

Growth and Characterizations of Two-Dimensional Metal-Organic Frameworks

by

Dong-Gwang Ha

Submitted to the Department of Materials Science and Engineering

in partial fulfillment of the requirements for the degree of

Doctor of Philosophy in Materials Science and Engineering at the

MASSACHUSETTS INSTITUTE OF TECHNOLOGY

June 2019

©Massachusetts Institute of Technology 2019. All rights reserved

Signature redacted

Signature of Author.....

Department of Materials Science and Engineering

May 01, 2019

Signature redacted

Certified by

Marc A. Baldo

Professor of Electrical Engineering and Computer Science

Thesis Supervisor

Signature redacted

Certified by

Harry Tuller

Professor of Materials Science and Engineering

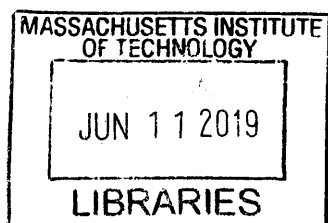
Thesis Reader

Signature redacted

Accepted by

Donald R. Sadoway

Chair, Department Committee on Graduate Studies



ARCHIVES

Growth and Characterization of Two-Dimensional Metal-Organic Frameworks

by

Dong-Gwang Ha

Submitted to the Department of Materials Science and Engineering

On May, 1st, 2019, in partial fulfillment of the requirements for the

Degree of Doctor of Philosophy in Materials Science and Engineering

Abstract

Metal-Organic Frameworks (MOFs) are a class of porous materials with a crystalline structure that can be designed based on extremely tunable building blocks of organic molecules and metal ions. They are typically insulators but making them π -conjugated with two-dimensional structure results in high electrical conductivity. This makes the two-dimensional π -conjugated MOFs (2D π MOFs) good candidates for applications that need porous conductors such as supercapacitors and batteries. More importantly, tunability of the crystal structure enables us to explore exotic physical properties, including topological protection. This great potential has inspired the synthesis of various 2D π MOFs, but their crystal growth remains challenging, preventing the characterization of intrinsic electrical properties.

In this thesis, I will explain the growth mechanisms of 2D π MOFs and the limitations of conventional growth methods. Based on the analysis, I developed a novel growth method that generates single-crystal plates of a 2D π MOF, $\text{Ni}_3(\text{HHTP})_2$ (HHTP= 2,3,6,7,10,11-hexahydroxytriphenylene), over 10 μm in lateral dimension, two orders of magnitude larger than previous reports. The growth mechanism of the new method is also studied by varying multiple growth parameters.

The properties of the single crystals are characterized by various spectroscopic techniques. Among assorted characteristics, the electrical properties are explored closely. The large single-crystal plates enable us to study in-plane properties of a 2D π MOF for the first time. The in-plane conductivity of $\text{Ni}_3(\text{HHTP})_2$ is up to 2 S/cm, two orders of magnitude higher than pressed pellet, and shows a clear temperature dependence. Hall measurements reveal that the origin of the high conductivity is a high charge carrier density rather than high charge carrier mobility. We anticipate our demonstration will facilitate the discovery of fundamental properties of various 2D π MOFs and further our realization of their potential as electronic materials.

Thesis Supervisor: Marc A Baldo

Title: Professor of Electrical Engineering and Computer Science

Acknowledgements

The work presented in this thesis would not be possible without many people who guided and worked with me. First, I would like to express my deepest appreciation to my advisor, professor Marc Baldo. I was so fortunate to be part of his group and enjoyed the research culture he created in the lab. He introduced an exciting research topic, and supported the risky path I chose. Until I passed my first huddle, I failed continuously over a year. If it was not him, I am sure that this work would not have been successful.

I would like to extend my thanks to my thesis committee members, professor Harry Tuller and professor Ju Li. I could build the foundation of this work from the thesis area exam and meetings. Their critical comments and knowledge are invaluable.

This work requires interdisciplinary collaborative efforts, and I have been lucky to have a dream team for my PhD journey. I am thankful to professor Mircea Dinca. His expertise on the chemistry of MOFs and knowledge accumulated in his lab was absolutely necessary for this work. I must thank professor Jing Kong. She was always available for discussion, and gave me ingenious suggestions on 2D materials growth. Also, I would like to thank professor Philip Kim for valuable discussion and providing me with insights on transport properties and opportunities to work in his lab.

I must thank all SEE group members. Special thanks to Brian who taught me about 2D materials and transferred valuable know-how. Tony and Markus trained me on many instruments and also worked together on OLEDs projects. Saima helped me fabricating many MOF devices, and Joe was always there for discussion. Without Jan, we could not discover our new findings on the OLED degradation. Cathy always supported administrative work promptly and kindly. Many discussions including topics outside research with the group members inspired and energized me. Thank you all.

I would like to thank collaborators from other groups. Lei answered me promptly and clearly whenever I threw him questions on MOFs. Discussion with Bobby was always constructive and inspired me to think about the growth more. I would also like to thank Lilia for helping and teaching me characterizing the MOF. Yimo's expertise on TEM and her enthusiastic attitude resulted in high-quality images. Mehdi and I worked together on electrical characterizations of

the MOF. The measurement data is outcome of many late nights and weekends. Tamar, Hyobin and Frank gave me fruitful discussions and helped. Thank you all.

I should acknowledge the Kwangjeong educational foundation for financial support. They supported me for five years of PhD as well as 3 years of undergraduate studies.

Lastly, but the most importantly, I would like to thank my family, especially my wife Ivy. Her love has invigorated my life throughout my PhD. As a mother of two sons, her devotion to our family enable me to pursue my passion. My family made my PhD period delightful and they are my strong motivation to work hard in life. I hope I can payback more than what I have received as we continue our journey.

Contents

1. Introduction and background.....	20
1.1. Metal-Organic Frameworks	20
1.1.1. Why MOFs are important?	20
1.1.2. Applications of MOFs	23
1.2. Two-dimensional π -conjugated Metal-Organic Frameworks	24
1.2.1. Conductive nature of 2D π MOFs	25
1.2.2. Reported 2D π MOFs	27
1.2.3. Exotic properties of 2D π MOFs	31
1.2.4. Potential applications of 2D π MOFs	33
2. Growth of 2D πMOFs.....	35
2.1. Why is 2D π MOF growth challenging?	36
2.2. Reported growth methods and problems.....	38
2.2.1. Single-phase solution growth	38
2.2.2. Liquid/liquid interfacial growth.....	40
2.2.3. Liquid/gas interface	41
2.2.4. Coevaporation.....	41
2.2.5. Summary of the limitations	42
2.3. Solid-liquid growth	42
2.4. Growth mechanism	46
2.4.1. Reaction time and growth.....	46
2.4.2. Proposed growth mechanism	50
2.5. Growth of other 2D π MOFs	53
2.6. Growth parameters	54

2.6.1. HHTP related parameters	55
2.6.2. Ni(OAc) ₂ related parameters	56
2.6.3. Amount of water between the substrates	57
2.7. Vacuum process	58
2.7.1. Vacuum reaction.....	58
2.7.2. Chemical Vapor Deposition	60
3. Characterization of the crystals.....	63
3.1. Powder synthesis	63
3.2. TEM	64
3.3. EDX.....	66
3.4. UV-Vis-IR spectrum	68
4. Device fabrication with Ni₃(HHTP)₂ single crystal.....	71
4.1. E-beam lithography process	71
4.2. Stencil-mask process	74
4.3. Crystal transfer process	76
5. Electrical properties of the Ni₃(HHTP)₂ single crystal.....	78
5.1. Expected properties of Ni ₃ (HHTP) ₂	78
5.2. Electrical conductivity.....	81
5.2.1. Measurement of highly resistive materials.....	81
5.2.2. Fabrication methods and conductivities	82
5.2.3. Anisotropic nature	83
5.2.4. Temperature dependence	84
5.3. Hall measurement.....	86
5.3.1. Challenges in Hall measurement	86

5.3.2. Carrier density and mobility of $\text{Ni}_3(\text{HHTP})_2$	87
5.4. Comparison with other materials	89
6. Conclusion and outlook	92
7. Special chapter	95
7.1. Link between hopping models and percolation scaling laws	96
7.2. Degradation of phosphorescent dyes	103
7.2.1. Degradation model	104
7.2.2. Photodegradation measurement.....	110
7.2.3. Dominance of exciton lifetime in stability	114
7.2.4. Experimental methods	119
List of publications	122
Bibliography	123

List of Tables

Table 1-1 Reported 2D π MOFs conductivity and sample conditions. For the chemical structure, please refer to Figure 1-3. ^a The naming of the MOFs can be confusing as there are different ways to name due to the large unit cell. Please refer to both Figure 1-3 and references for the correct chemical structure. ^b The grain size is subjectively judged by SEM or TEM images from the references, thus it is accurate only within an order of magnitude. ^c This is the only reported single-crystal conductivity of 2D π MOFs.	29
Table 1-2 Exotic properties of synthesized 2D π MOFs by theoretical calculation. Note that the properties are based on a monolayer of the MOFs.	32
Table 2-1 Summary of the growth methods and their strong and weak points.	42
Table 7-1 The three classes of degradation mechanisms that generate degraded molecules within an OLED and their defect generation rate as a function of triplet exciton-generation rate (G) and triplet exciton lifetime (τ). The dependence of the OLED lifetime to 90% of initial luminance (LT90) on the triplet exciton lifetime is significant because exciton lifetime not only contributes to the triplet exciton density, but also influences quenching losses at defect sites.....	104
Table 7-2 Triplet exciton generation rate dependence of the photodegradation of Ir(ppy) ₃ :CBP. On the left, we summarize varying CBP spacer thickness for 10% Ir(ppy) ₃ :CBP films. The structure employed is Ag(20 nm)/CBP(1, 5, 10, 20, 45 nm)/10% Ir(ppy) ₃ :CBP(10 nm)/CBP(10 nm). On the right, we summarize, the concentration dependence in the absence of a silver film. The structure is CBP (10 nm)/ 10% Ir(ppy) ₃ :CBP(10 nm)/ CBP (10 nm). As is the case for 10% doped Ir(dmp) ₃ :mCBP, samples that include a silver layer exhibit pump power laws with exponents of approximately 1.5, consistent with the presence of triplet-charge interactions. In the absence of the silver film, the power law slopes are around 1, indicates unimolecular degradation. Note that the slope becomes nearly 2 for neat Ir(ppy) ₃ , due to the strong triplet-triplet annihilation.....	118

List of Figures

Figure 1-1 Example structures of MOFs. (a) MOF-5. Benzodicarboxylic acid (organic ligand) is linked with Zn_4O nodes and it forms a simple cubic structure. (b) $Ni_3(HHTP)_2$ (also called Ni-CAT-1) is a two-dimensional MOF. Hexahydroxytriphenylenes are connected with nickel ions to form a 2D hexagonal structure..... 22

Figure 1-2 Schematic illustration of the energy levels of conventional MOFs vs 2D π MOFs. (a) Conventional MOFs. When an organic ligand and a metal ion meet, each energy level is slightly shifted or some new levels can be created from the interaction. However, the levels remain discrete as electrons are localized. Also, the localization means charge carriers need to hop from site to site which greatly reduces charge transport. (b) 2D π MOFs. The delocalization of electrons results in the formation of bands. This can lead to small or zero band gap. Also, the delocalization promotes carrier transport. The high carrier density and high mobility makes them conductive..... 26

Figure 1-3 Chemical structures and names of two archetypical types of 2D π MOFs. For the metal elements, I include them only if the conductivity is reported. Other metal elements can be adopted as long as square-planar coordination bonding is used. Iron, for example, forms octahedral coordination bonding so it requires two additional molecules which bond to the top and bottom of the layer. In that case, monolayers would be not one-atomic-layer thick anymore. (a) Triphenylene-based 2D π MOFs (b) Benzene-based 2D π MOFs 30

Figure 1-4 2D hexagonal and Kagome structures and their band diagrams. (a) 2D hexagonal lattice (b) Kagome lattice (c) Hexagonal-Kagome lattice. (d) Band structure of 2D hexagonal lattice. It exhibits Dirac bands which give massless behavior of the electrons near Dirac point (e) Band structure of a Kagome lattice. It has Dirac bands and an additional flat band. (f) Band structure of a Hexagonal-Kagome lattice. It is combination of (d) and (e). The figure is from J.-L. Lu et al, Chin. Phys. Lett. 34, 057302 (2017). Many 2D π MOFs have the hexagonal-Kagome structure, so there are two Dirac cones and one flat band according to simple tight-binding model..... 32

Figure 2-1 Redox states of deprotonated HHTP. For the MOF reaction, it needs to be half-oxidized which is the structure at the bottom left 37

Figure 2-2 Growth of single-crystal plates of $\text{Ni}_3(\text{HHTP})_2$. (a) Chemical structure of $\text{Ni}_3(\text{HHTP})_2$. (b) Schematic illustration of the growth method. The HHTP film is grown by vacuum thermal evaporation, and nickel acetate is drop-cast on a separate substrate. The two substrates are pressed together with a teflon-coated magnet, and placed in water. After, the vial is kept in a 95°C oven for a designated time to grow the 2D π MOF. A high nucleation density boosts crystal formation, and the tight reaction space promotes larger crystal growth. Also, the high reaction temperature gives rise to high crystallinity. In addition, the horizontal alignment of HHTP increases the 2D growth rate. Typically, I use a HHTP film thickness of 40nm and reaction time of 12 hours to grow single-crystal microplates. Under these conditions, the biggest crystal obtained from an independent run is at least 5 micrometers in diagonal on the 2D plane. 43

Figure 2-3 SEM and Optical microscope images of $\text{Ni}_3(\text{HHTP})_2$. (a) SEM image of the growth result. Sharp edges and corners of hexagons suggest high crystallinity of the crystals. (b,c) optical microscope images of a single-crystal plate on a Si/SiO₂ (285 nm) substrate..... 44

Figure 2-4 Growth results from different growth times. (a) half hour, (b) 1 hour, (c) 3 hours, (d) 12 hours of the reaction. Note that (a) and (b) are SEM images and (c) and (d) are optical microscope images. Also the scale bars are different for the images. 46

Figure 2-5 Higher magnification SEM image of a crystal after half hour reaction. Multiple spiral growth is happening on the surface of the crystal..... 47

Figure 2-6 Growth with the addition of 5mg of Na(OAc) to water. It makes the pH of the water around 8.5. The reaction time is 3 hours, but the crystals have sharp edges due to the increased reaction rate. (a) optical microscope image (b) AFM image (c) cross-section profile of the AFM image..... 48

Figure 2-7 AFM images and cross-sectional profiles of crystals after 12 hours of reaction. The surface is much smoother than shorter reaction-time samples. 49

Figure 2-8 Schematic illustration of the proposed growth mechanism. Initially organic ligands remain as an aligned solid film. The dissolved nickel ions meet the ligands and form the coordination bonding. At the same time some molecules or HHTP-Ni complexes can be dissolved into the water. As more ligands are connected it starts to form a crystalline facet. At this stage, there are still abundant HHTP or HHTP-Ni complexes around the crystals if the initial HHTP thickness is more than 30 nm. As the reaction continues, the crystals grow through the supply of HHTP and nickel, or by merging with other crystals. High temperature fixes defects and increases the crystallinity with longer reaction time..... 50

Figure 2-9 Variable angle spectroscopic ellipsometry data of evaporated HHTP film on silicon. (a) Complex refractive indexes of ordinary and extraordinary direction. (b) Fitting result of Psi and Delta for variable angles. The measurement was done by J. A. Woollam M-2000 and WVASE32 instruments. Both gave identical results. The sample was prepared by evaporation of 30nm HHTP on a bare silicon substrate with a native oxide. The measurement angle was 45° to 70° with 5 degree steps. The analysis started using the Cauchy model in the transparent region. Then it was slowly expanded to the whole region by the anisotropic B-spline model satisfying Kramers-Krönig consistency. 51

Figure 2-10 Growth with drop-cast HHTP instead of evaporated HHTP film. There was no single crystal plate found on the substrate. The crystals are small and polycrystalline. For the HHTP drop-casting, 10 µl of 1.7 mM methanol solution is drop-cast two times on a substrate. The HHTP amount is identical to that of 40nm film. 53

Figure 2-11 SEM image of $\text{Co}_3(\text{HHTP})_2$ and elemental distribution of cobalt, carbon and oxygen. Note that the background oxygen signal originates from the SiO_2 substrate. 54

Figure 2-12 Effect of HHTP patterning. Schematic illustration of unpatterned (a) and patterned (b) HHTP films. The line pattern is 0.1-inch-wide with 0.2-inch period. Optical microscope (c) and AFM (d) images of the growth result with patterned HHTP. Generally symmetric hexagonal crystals are obtained, but asymmetric hexagons are also observed. These might be grown from the edges of the line pattern. 56

Figure 2-13 Crystals grown by reaction under vacuum. Hexagonal plates are yellow circled. The small bright dots are copper which are reduced from Cu(OAc)₂ probably due to the oxidation of HHTP. 59

Figure 2-14 Schematic illustration of the CVD setup. HHTP is spuncoat on a silicon substrate and placed in the center of the furnace tube within an additional small tube. The additional small tube increases the concentration of Cu(OAc)₂ around the HHTP substrate. Cu(OAc)₂ is placed near the end of a single-zone furnace so that the two materials evaporate at the same time. Argon was used as carrier gas and a dry pump was used to remove air. 60

Figure 2-15 A flake grown with the CVD method and its electrical conductivity. (a) SEM image. (b) AFM image. The surface of the flake is as smooth as the silicon substrate. (c) optical microscope image after device fabrication. (d) current-voltage characteristics. Unfortunately, many contacts were open and this characteristic is two-probe data. It deviates a little bit from Ohmic behavior, which indicates a bad contact. The conductivity is estimated to be 1×10^{-2} S/cm which is similar to reported values. 62

Figure 3-1 PXRD of powder of Ni₃(HHTP)₂. The strong peak at $2\theta=4.555$ degree corresponds to a lattice parameter of 22.4 Å. 63

Figure 3-2 Low magnification (52,000 X) TEM image of the crystal. Due to the large unit cell of the MOF, the lattice is visible at this low magnification. It has a uniform hexagonal structure, and the low-bottom corner is the corner of the hexagonal single crystal. Inset: Fourier transform image. It confirms the hexagonal structure with a lattice spacing of $a=b=2.1$ nm which matches well with the PXRD data. 64

Figure 3-3 The high magnification TEM image. The bright circles are the pores of Ni₃(HHTP)₂. The lattice matches well with the crystal structure of Ni₃(HHTP)₂. It was measured with Tecnai F20 at an acceleration voltage of 120 kV. Estimated electron-beam dose was 10^5 electrons/Å². 65

Figure 3-4 SEM image of crystals (left) and elemental distribution of nickel, carbon, oxygen and silicon measured by EDS. 66

Figure 3-5 EDX phase mapping image and the corresponding energy dispersive spectrum. The crystal (blue phase) has clear carbon and nickel peaks whereas the background (red phase) has only silicon and oxygen peaks. 67

Figure 3-6 IR spectrum of HHTP single crystal (blue) and powder (red). The finger print region (Wavenumber below 1500 cm^{-1}) matches well with the powder IR. This is an additional proof that the single crystal is $\text{Ni}_3(\text{HHTP})_2$ 68

Figure 3-7 Band gap determination of $\text{Ni}_3(\text{HHTP})_2$ powder (a) IR and UV-vis-NIR spectrum of $\text{Ni}_3(\text{HHTP})_2$ powder by diffusive reflectance measurement (black and red) and transmission measurement (blue). (b) Tauc plot with an indirect band assumption. The band gap is determined from extrapolation of the linear band edge and it is 0.18 eV,..... 70

Figure 4-1 Device fabrication with e-beam lithography. The baking step, electron beam exposure, and metal evaporation process can potentially damage the crystals. Also residual PMMA can lead to a bad contact which is detrimental to the Hall measurement. 72

Figure 4-2 An example image of single crystal fracture after device fabrication with the electron-beam lithography technique. 74

Figure 4-3 (a) Schematic illustration of device fabrication with the stencil-mask process (b) Optical microscope image of a device fabricated with the stencil mask process 75

Figure 4-4 Bottom contact device fabricated with crystal transfer to a pre-patterned substrate. . 77

Figure 5-1 DFT-calculated band structure of monolayer $\text{Ni}_3(\text{HHTP})_2$. It is expected to be metallic in monolayer form. The Dirac point is located about 0.3 eV above the Fermi level. This calculation is done by Wenbin Li from Ju Li group at MIT. 78

Figure 5-2 DFT calculated band structure of bulk $\text{Ni}_3(\text{HHTP})_2$ with an assumption of AA stacking. Note that the x-axis is not proportional to the amplitude of the k vector. Γ to A distance is much larger than others. This calculation is done by Jian Zhou from Ju Li group at MIT. 80

Figure 5-3 Electrical conductivities as a function of the various crystal size and the three fabrication methods. Note that the electrical conductivity increases by one order of magnitude under vacuum. All the devices fabricated with the stencil mask technique were measured under vacuum and others are measured in ambient environment. 82

Figure 5-4 Temperature dependence of conductivity for the single crystal and pressed pellet sample. The single crystal shows clean mono-exponential dependence with an activation energy of 0.1 eV..... 85

Figure 5-5 current-voltage curves from 300K to 100K. All of them show Ohmic behavior. 86

Figure 5-6 Hall measurement at room temperature. The Hall coefficient was $-0.46 \pm 0.14 \text{ cm}^3/\text{C}$. If the crystal is an extrinsic semiconductor or electron mobility is much higher than hole mobility, the carrier density is estimated as $1.4 \times 10^{19} \text{ cm}^{-3}$ and the electron mobility is $0.16 \text{ cm}^2/\text{V}\cdot\text{sec}$ 88

Figure 5-7 Mobility-carrier density-conductivity mapping of various materials. The color indicates the electrical conductivity in log scale. The dotted diagonal lines represent the order of magnitude of the conductivity. 91

Figure 7-1 Schematic illustration of charge transport in mixtures of small molecules: (a) transport below percolation threshold (b) above percolation threshold. Charge moves along the conductive molecules. At high concentration of the molecules, a percolation path is formed and carriers transport with hopping transport. 97

Figure 7-2 (a) Structure of the hole only devices. TAPC has high LUMO level which prevent injection of electrons. (b) Molecular structures of TCTA and BmPyPb. (c) Energy level configuration of the devices. The deep HOMO level of BmPyPb hinder the hole transport. (d) Current density- voltage characteristics of the hole only devices with different mixing ratio. Inset: Relative current density of the devices. It is normalized by the 100% TCTA hole-only device. 98

Figure 7-3 (a) Relative current density as a function of TCTA mixing ratio. Fitting of the percolation scaling law, red line, gives the (x_0, t) of (0.18, 1.6). (b) Relative current density as a function of the hopping distance. Fitting with the MA hopping model gives α of 2.4 Å..... 99

Figure 7-4 (a) Numerical calculation of the SMAPE, which is defined in Eq. (7.5), for the x_0 of 0.18. The dashed black line represents Eq. (7.4). It is well contained within the lowest error region. (b) Extracted minimum SMAPE for $1 < t < 2.5$ from (a) (black square), and the SMAPE along the Eq. (4) in (a) (red circle). (c) The minimum SMAPE for different x_0 values in the range of $1 < t < 2.5$ 100

Figure 7-5 The chemical structures and energy levels of (a) blue, and (b) green emission layer. The HOMO levels were measured by ultraviolet photoemission spectroscopy for Ir(ppy)₃, CBP, Ir(dmp)₃, and mCBP^{134,140}. The LUMO levels of Ir(ppy)₃ and CBP were determined by inverse photoemission spectroscopy¹⁴⁰. The LUMO levels of Ir(dmp)₃ and mCBP were determined from the optical gaps¹³⁴ and assuming identical exciton binding energies in Ir(ppy)₃ and CBP, respectively. The sample structure for the blue system (c) is Ag(34 nm)/mCBP(10, 20, 45, 150 nm)/Emission layer(10 nm)/mCBP(10 nm) and the green system (d) is Ag(20 nm)/CBP(0, 5, 10, 20, 45, 100 nm)/Emission layer(10 nm)/CBP(10 nm)..... 110

Figure 7-6 Transient photoluminescence of (a) 10% Ir(dmp)₃:mCBP and (b) neat Ir(ppy)₃, as a function of varying spacer thickness d. As expected, reducing the distance between the emission layer and the Ag corresponds to increasingly fast exciton decay due to strong coupling to the non-radiative surface plasmonic modes in Ag. The photodegradation curves for the (c) blue and (d) green systems as a function of d. Samples with emission layers closer to Ag experience a stabilizing effect, i.e. slower photodegradation due to the shorter exciton lifetime. 112

Figure 7-7 Transfer matrix calculation for neat Ir(ppy)₃ samples for different spacer layer and experimental data measured by the integrating sphere. The absorption is corrected based on this calculation. 113

Figure 7-8 The stability in both green (neat Ir(ppy)₃) and blue (10% Ir(dmp)₃:mCBP) systems as a function of the generation rate of triplet excitons, G, and the triplet exciton lifetime, τ . As we predicted from the degradation model, the exciton lifetime has much stronger impact on the

degradation rather than exciton generation rate for both systems. The difference in slope between the green and blue system is due to the different degradation mechanism. The slope of the pump-power dependence indicates that neat Ir(ppy)₃ degrades from triplet-triplet annihilation and the doped Ir(dmp)₃ degrades from triplet-charge annihilation. Note that the degradation mechanism changes from triplet-charge annihilation to unimolecular process when d is 150nm. Values for LT90 are extracted from the data presented in Figure 7-6 and plotted on a normalized logarithmic scale against (top) triplet exciton generation rate (G) and (bottom) triplet exciton lifetime (τ)..... 115

Figure 7-9 Exciton lifetime dependence of 10% Ir(ppy)₃:CBP degradation. The slope is 2.4 which indicates the triplet-charge degradation based on our degradation model. LT90s for emission layers very close to Ag are reduced compared to the trend at larger distances from Ag. 116

Figure 7-10 Photocurrent of a 10% Ir(ppy)₃:CBP photovoltaic device. The device structure is ITO(100nm)/10% Ir(ppy)₃:CBP (60nm)/Al (80nm), and it is exposed to a λ=365 nm LED with 5.6 W/cm². The open circuit voltage is 9.3 mV and the short circuit current density is..... 117

1. Introduction and background

1.1. Metal-Organic Frameworks

1.1.1. Why MOFs are important?

Metal-Organic Frameworks (MOFs) ¹⁻³ are a class of porous materials with a crystalline structure that can be designed with tunable building blocks of organic molecules and metal ions as shown in Figure 1-1. MOFs have three major advantages. First, the crystalline structure can be designed. Generally, if you need a material with a specific crystal structure, you need to find a material that has the structure. With MOFs, however, you can design the crystal structure as chemists design a molecule. Materials properties and crystal structure are closely related. This design capability alone gives strong tunability. Some properties such as topologically nontrivial properties have a very demanding crystalline structure, so only limited numbers of materials are known. MOFs enable us to design a new material to obtain a desired crystal structure rather than trying iterative material synthesis. MOFs are ideal material systems to optimize a structure and property relation.

Second, the building blocks are extremely tunable. One of the building blocks is an organic molecule. The number of stable organic molecules is expected to be on the order of 10^{180} when the molecular weight is restricted to below 1000 g/mol and elements are limited to carbon, nitrogen, oxygen, phosphorous, sulfur and halogens ⁴. This near infinite number of building blocks enables to fine-tune the properties of MOFs. Moreover, another building block is a metal ion or cluster. Therefore, nearly every element on the periodic table can be utilized for the design of MOFs.

Third, MOFs are nano-porous. The crystal structure itself includes pores, so MOFs have the highest surface area per weight ⁵. This is a distinct feature of MOFs compared to other

materials, and it makes MOFs ideal candidates for many applications such as gas storage, gas separation, catalysis, sensors, electrodes for batteries or supercapacitors, etc. Also, guest molecules can be adsorbed into the pores and bring other properties to the MOFs as well.

The above three advantages combine to yield vast freedom in material design. In the following chapters, I will describe how these are utilized for different applications.

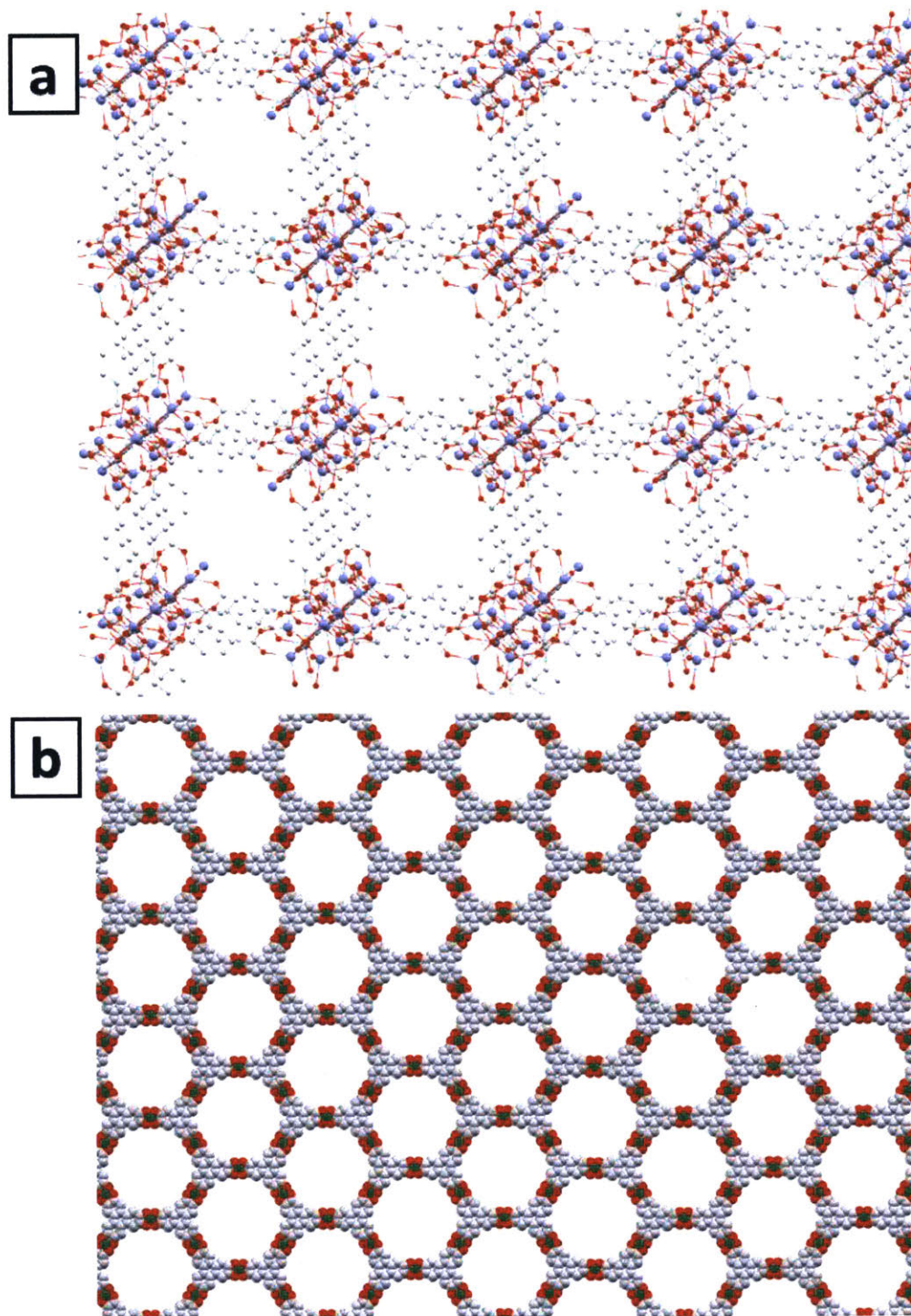


Figure 1-1 Example structures of MOFs. (a) MOF-5. Benzodicarboxylic acid (organic ligand) is linked with Zn_4O nodes and it forms a simple cubic structure. (b) $Ni_3(HHTP)_2$ (also called Ni-CAT-1) is a two-dimensional MOF. Hexahydroxytriphenylenes are connected with nickel ions to form a 2D hexagonal structure.

1.1.2. Applications of MOFs

In this chapter, I will briefly explain the current and potential applications of MOFs. The focus is to explain why MOFs are adequate for those applications rather than a detail review of the fields.

Gas storage

Hydrogen and methane are clean energy sources for applications including automobiles. For the success of the clean vehicles, we must have safe and dense storage of the gases. MOFs have the outstanding surface area which maximizes the density of the stored gas. Also, their tunability can optimize desirable adsorption properties such as adsorption enthalpy and its temperature dependence ⁶. By filling the conventional gas cylinders with MOFs, more gas can be stored at lower pressure ⁷.

Hazardous gas storage can be improved by using MOFs as well. MOFs decrease the cylinder pressure while maintaining the same amount of gas which results in safe handling of the gas cylinder. It reduces the risk of gas leakage or dangerous accident related to high pressure of the tank. MOF-based hazardous-gas cylinders have been successfully commercialized for semiconductor fabrication processes ⁸. The purity of the released gas is the most important factor for this application, and the success of MOFs proves that some MOF candidates can be stable for a long time (>10 years) and chemically inert. Other porous materials such as zeolites were not qualified for the application due to deficiencies concerning the gas purity.

Gas separation

One of the most important environmental issues is carbon dioxide emission. To solve the problem, it is important to capture it selectively from gas mixtures. The large surface area of MOFs increases the separation capacity, and the chemical tunability can optimize adsorption and

selectivity of the gas⁹. Furthermore, designing the crystal structure can generate steric hindrance for specific molecules which can improve the selectivity¹⁰.

Another important gas separation application is getting clean water from the air. MOFs can selectively adsorb water vapor in the air. The chemical tunability can optimize adsorption characteristics, and it was recently demonstrated that a MOF can harvest water from desert air just with solar power¹¹. The gas separation with MOFs are not limited to CO₂ or H₂O. Hazardous gas separation or many other separations are also an active area of research¹².

Catalysis

MOFs are also ideal candidates for catalysis applications. First, accessibility to metal sites is excellent. Due to the inherently large surface area, a small amount of metal can accelerate a large number of chemical reactions. On the contrary, conventional expensive noble metals such as platinum only utilize the surface of the catalyst for reactions; any bulk material is wasted. Second, the control of micro- and mesoscopic pores can introduce size selectivity¹³. Lastly, chemical tunability can fine-tune reactions.

1.2. Two-dimensional π -conjugated Metal-Organic Frameworks

MOFs are typically insulators due to the use of non-conjugated building blocks. Recently, however, conductive MOFs have been synthesized, opening up new applications of MOFs¹⁴. There are several ways to make MOFs conductive¹⁵. Among these, two-dimensional π -conjugated MOFs (2D π MOFs) have shown the highest conductivity¹⁵. In this chapter, I will give background information on 2D π MOFs.

1.2.1. Conductive nature of 2D π MOFs

2D π MOFs are formed when fully π -conjugated and flat small molecules are linked with metal ions that can form square-planar type coordination bonding as shown in Figure 1-1(b). Consequently, electrons are delocalized in the layers with the π -conjugation which results in the formation of bands. Therefore 2D π MOFs can have narrow or zero band gap which makes them semiconductors or metals as shown in Figure 1-2. In contrast, conventional MOFs do not exhibit delocalization, and the energy levels of the MOFs are determined by the energy levels of building blocks. Also, the localized electrons cannot move freely. These make conventional MOFs insulating.

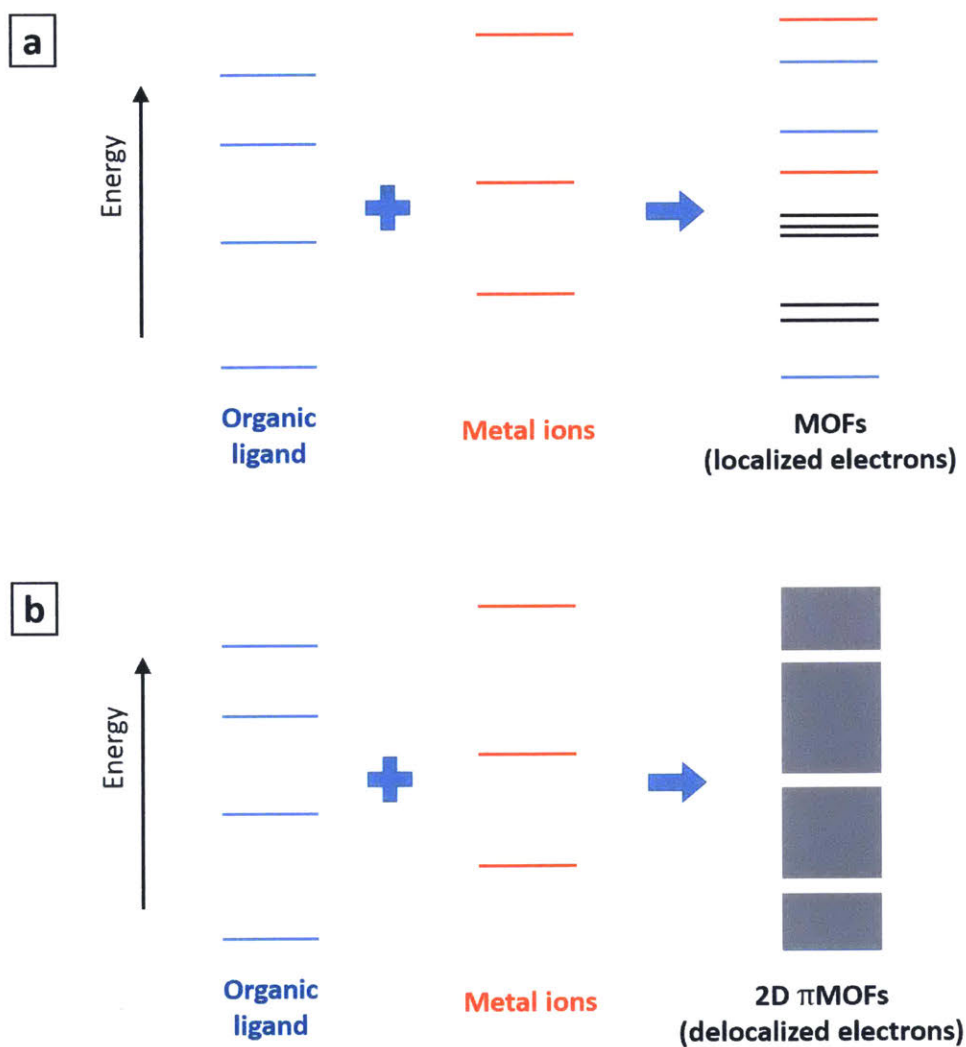


Figure 1-2 Schematic illustration of the energy levels of conventional MOFs vs 2D π MOFs. (a) Conventional MOFs. When an organic ligand and a metal ion meet, each energy level is slightly shifted or some new levels can be created from the interaction. However, the levels remain discrete as electrons are localized. Also, the localization means charge carriers need to hop from site to site which greatly reduces charge transport. (b) 2D π MOFs. The delocalization of electrons results in the formation of bands. This can lead to small or zero band gap. Also, the delocalization promotes carrier transport. The high carrier density and high mobility makes them conductive.

1.2.2. Reported 2D π MOFs

Since the first report of electrical conductivity of 2D π MOFs in 2012¹⁶, many 2D π MOFs have been synthesized to increase the conductivity. The reported electrical conductivities are summarized in Table 1-1.

Great care needs to be taken to interpret the conductivity value because it is measured in polycrystalline film or pressed pellets except for the first report. But the only single crystal conductivity is measured along the out-of-plane direction which is irrelevant to the 2D properties. Even though the 2D π MOFs have 2D structure, the conductivity along the 2D plane has never been measured due to the morphology of the samples. Also, the 2D domain size is typically much smaller than 1 micrometer as shown in the table. They can include small crystals with several tens of nanometers size. Considering the large unit cell of the MOFs, the crystal size can be below 10 times the lattice parameter. For example, the triphenylene-based MOFs have unit cell parameter of ~ 2 nm. A crystal size smaller than 20nm means unit cell repeats less than 10 times, disrupting delocalization and leading to quantum confinement as in a quantum dot. The growth of large single crystal and characterization along the 2D plane is necessary to understand the intrinsic properties of 2D π MOFs.

The electrical conductivity is greatly affected by sample quality and morphology as shown in Table 1-1. For example, the electrical conductivity of $\text{Cu}_3(\text{HHTP})_2$ varies by three orders of magnitude. The spread is even bigger for $\text{Co}_3(\text{HTTP})_2$ and $\text{Ni}_3(\text{HITP})_2$. Previous reports confirmed the identity of the samples by powder x-ray diffraction so the variation in conductivity is not due to differing chemical composition. Instead, the purity and morphology of the samples greatly affect the conductivity. Note that generally higher reaction temperature leads to higher conductivity. Higher temperature gives higher crystallinity because the coordination

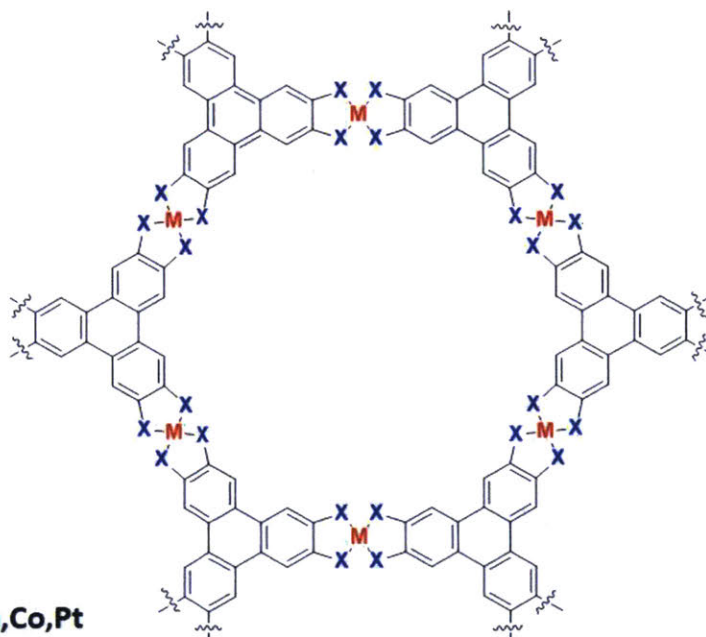
bonding is more reversible, allowing the material to more closely approach its most stable equilibrium structure. This indicates that crystallinity is important to achieve high conductivity.

Regardless of the non-ideal sample morphology, the electrical conductivity values vary by 12 orders of magnitude which shows the tunability of MOFs. Some of them are claimed to be metallic based on spectroscopic data and DFT calculations. CuBHT showed superconductivity at 0.25K. Note that it is arguable whether CuBHT can be considered as a MOF or not because it is not porous. According to IUPAC definition ³, a MOF needs to be porous. If not, it is a coordination polymer. Among the MOFs, Ni₃(HITP)₂ and Ni₃(BHT)₂ are considered as the most conductive MOFs. In many cases, 2D π MOFs are based on triphenylene or benzene. The chemical structures and naming of the 2D π MOFs are shown in Figure 1-3.

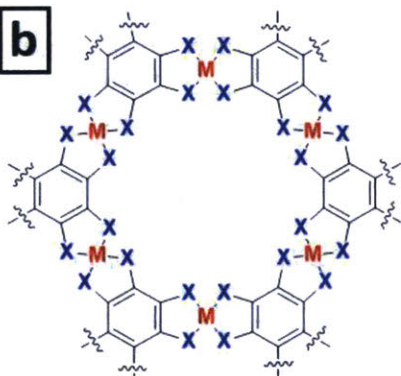
2D- π MOF Name ^a	Electrical conductivity (S/cm)	Sample Type	Growth Medium, Temperature (°C)	2D Grain Size (nm)	Note	Ref.
Cu ₃ (HHTP) ₂	0.2	Single crystal ^c , 4 probe	Solution, 85	200	Measured along c-axis direction.	16
Cu ₃ (HHTP) ₂	7.6×10 ⁻³	Pressed pellet, 4 probe	Solution, 80	140	.	17
Cu ₃ (HHTP) ₂	2×10 ⁻²	Film, 2 probe	layer-by-layer RT	50 ^b	.	18
Cu ₃ (HHTP) ₂	1×10 ⁻⁴	Film, 2 probe	Interfacial (liquid/gas) RT	<200	.	19
Ni ₃ (HHTP) ₂	1×10 ⁻²	Pressed pellet, 4 probe	Solution, 80	72	.	17
Cu ₃ (HTTP) ₂	2.4×10 ⁻⁸	Pressed pellet, 4 probe	Solution, 65	200 ^b	.	20
Ni ₃ (HTTP) ₂	3.6×10 ⁻⁴	Pressed pellet, 4 probe	Solution, 65	<100 ^b		
Co ₃ (HTTP) ₂	3.4×10 ⁻⁹	Pressed pellet, 4 probe	Solution, 65	<100 ^b		
Co ₃ (HTTP) ₂	1.3×10 ⁻³	Pressed pellet, 4 probe	Interfacial (liquid/liquid), RT	.	Claimed the MOF is metallic	21
Pt ₃ (HTTP) ₂	3×10 ⁻⁴	Pressed pellet, 2 probe	Solution, 90	.	Broad PXRD peaks indicates limited crystallinity	22

$\text{Fe}_3(\text{HTTP})_2(\text{NH}_4)_3$	3.4×10^{-2}	Film, 4 probe	Interfacial (liquid/liquid), RT	$<30^b$	Very high Hall mobility of 220 cm^2/Vs . Carrier density is reported.	23
$\text{Ni}_3(\text{HITP})_2$	40	Film, 4 probe	Solution, 65	$<50^b$.	24
$\text{Ni}_3(\text{HITP})_2$	0.23	Film, 4 probe	Interfacial (liquid/air), 60	$<50^b$	Conductivity for 7 nm film is $8.5 \times 10^{-3} \text{ S/cm}$	25
$\text{Cu}_3(\text{HITP})_2$	0.2	Pressed pellet, 2 probe	Solution, 23	.	.	26
$\text{Ni}_3(\text{BHT})_2$	0.15	Pressed pellet, 2 probe	Interfacial (liquid/liquid), RT	.	.	27
$\text{Ni}_3(\text{BHT})_2$	160	Film, 4 probe	Interfacial (liquid/liquid), RT	.	.	28
$\text{Ni}_3(\text{HIB})_2$	8	Pressed pellet, 4 probe	Solution, 65	$<50^b$	Claimed the MOF is metallic	29
$\text{Cu}_3(\text{HIB})_2$	13	Pressed pellet, 4 probe	Solution, 65	$<100^b$	Claimed the MOF is metallic	
$\text{Ni}_3(\text{HIB})_2$	0.7	Pressed pellet, 4 probe	Solution, RT	<50		30
$\text{Cu}_3(\text{HIB})_2$	0.11	Pressed pellet, 4 probe	Solution, RT	<50		
$\text{Cu}_3(\text{HHB})_2$	7.3×10^{-8}	Pressed pellet, 4 probe	Solution, RT	$<100^b$		31
CuBHT	1580	Film, 4 probe	Interfacial (liquid/liquid), RT	16	Not porous.	32
CuBHT	2500	Film, 4 probe	Interfacial (liquid/liquid), 45	$>100^b$	Not porous. Superconducting at 0.25K	33
$\text{Pd}_3(\text{BHT})_2$	2.8×10^{-2}	Film, 4 probe	Interfacial (liquid/liquid)	.	.	34
NiPc-MOF	0.2	Pressed pellet, 4 probe	Solution, 160	$<100^b$	Square lattice	35

Table 1-1 Reported 2D π MOFs conductivity and sample conditions. For the chemical structure, please refer to Figure 1-3. ^aThe naming of the MOFs can be confusing as there are different ways to name due to the large unit cell. Please refer to both Figure 1-3 and references for the correct chemical structure. ^bThe grain size is subjectively judged by SEM or TEM images from the references, thus it is accurate only within an order of magnitude. ^cThis is the only reported single-crystal conductivity of 2D π MOFs.

a

	MOF name		Another name
X=O	M₂(HHTP)₃	HHTP=HexaHydroxyTriPhenylene	M-CAT
X=S	M₂(HHTTP)₃	HHTTP=HexaThioTriPhenylene	M₂(THT)₃
X=NH	M₂(HITP)₃	HITP=HexalminoTriPhenylene	

b

	MOF name		
X=O	M₂(HHB)₃	HHB=HexaHydroxyBenzene	
X=S	M₂(BHT)₃	BHT=BenzeneHexol	
X=NH	M₂(HIB)₃	HIB=HexalminoBenzene	

Figure 1-3 Chemical structures and names of two archetypical types of 2D π MOFs. For the metal elements, I include them only if the conductivity is reported. Other metal elements can be adopted as long as square-planar coordination bonding is used. Iron, for example, forms octahedral coordination bonding so it requires two additional molecules which bond to the top and bottom of the layer. In that case, monolayers would be not one-atomic-layer thick anymore. (a) Triphenylene-based 2D π MOFs (b) Benzene-based 2D π MOFs

1.2.3. Exotic properties of 2D π MOFs

Although the growth of 2D π MOFs is challenging, computational studies of monolayers of 2D π MOFs have predicted various exotic properties. Among these numerous studies, I will only highlight the calculated properties of MOFs that have been synthesized, as many of the calculated 2D π MOFs have unrealistic chemical structures. Table 1-2 summarizes the exotic properties. All the exotic MOFs have a hexagonal-Kagome lattice. As shown in Figure 1-4³⁶, a simple tight-binding calculation of hexagonal-Kagome lattice gives two Dirac cones and one flat band. The band structure can lead to topologically nontrivial properties if time-reversal symmetry is broken and at the same time spin-orbit coupling opens the gap. The time reversal symmetry can be broken with a magnetic field. If the material itself is ferromagnetic, the exotic properties do not require an external magnetic field. This is the case for $\text{Ni}_3(\text{HITP})_2$, $\text{Cu}_3(\text{HHB})_2$ and $\text{Ni}_3(\text{BHT})_2$. For $\text{Cu}_3(\text{HHTP})_2$ and $\text{Cu}_3(\text{HIB})_2$, a Dirac cone can be spin-polarized by the magnetic field. They are expected to be ferromagnetic at a low temperature so that electric current in a given direction is polarized with a single spin, a phenomenon known as half-metallicity. Another exotic property is superconductivity. CuBHT is expected to be a Bardeen–Cooper–Schrieffer type superconductor with a critical temperature of 1.6K for the bulk form. This is also experimentally demonstrated with a polycrystalline film which showed the critical temperature of 0.25K (see Table 1-1).

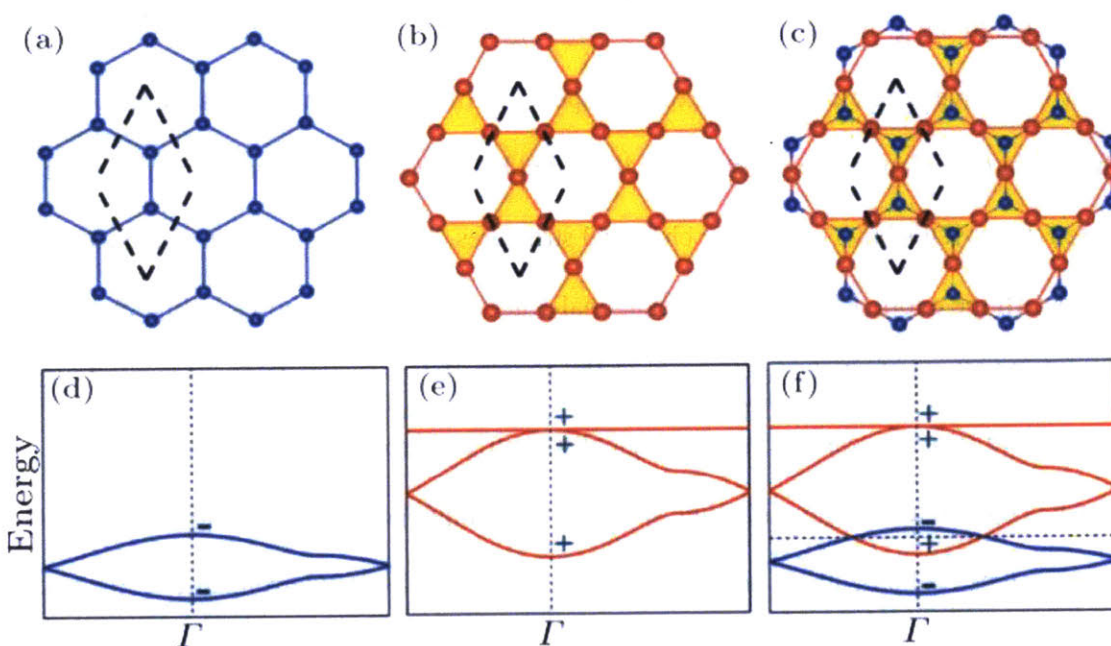


Figure 1-4 2D hexagonal and Kagome structures and their band diagrams. (a) 2D hexagonal lattice (b) Kagome lattice (c) Hexagonal-Kagome lattice. (d) Band structure of 2D hexagonal lattice. It exhibits Dirac bands which give massless behavior of the electrons near Dirac point (e) Band structure of a Kagome lattice. It has Dirac bands and an additional flat band. (f) Band structure of a Hexagonal-Kagome lattice. It is combination of (d) and (e). The figure is from J.-L. Lu et al, *Chin. Phys. Lett.* 34, 057302 (2017). Many 2D π MOFs have the hexagonal-Kagome structure, so there are two Dirac cones and one flat band according to simple tight-binding model.

2D- π MOF Name ^a	Exotic properties	Ref.
$\text{Cu}_3(\text{HHTP})_2$	Half-metal: The Kagome lattice gives Dirac-cone band structure and Fermi level is located in only one Dirac cone. The cone is spin-polarized due to the ferromagnetism.	37
$\text{Cu}_3(\text{HHB})_2$	Chern insulator. It will show quantum anomalous Hall effect	
$\text{Ni}_3(\text{HITP})_2$	Topological insulator. Requires electron doping which can be achieved by gating. The Fermi level needs to move up by 0.5 eV	38
$\text{Ni}_3(\text{BHT})_2$	Topological insulator	39
$\text{Cu}_3(\text{HIB})_2$	Half-metal	40
CuBHT	Superconductivity	41

Table 1-2 Exotic properties of synthesized 2D π MOFs by theoretical calculation. Note that the properties are based on a monolayer of the MOFs.

1.2.4. Potential applications of 2D π MOFs

A porous conductor is useful for many applications. First, MOFs are ideal candidates for electrodes of supercapacitors. The most important figures of merit for a supercapacitor are surface area and conductivity. $\text{Ni}_3(\text{HHTP})_2$, $\text{Cu}_3(\text{HIB})_2$ and $\text{Ni}_3(\text{HIB})_2$ have been tested as electrodes in supercapacitors, and they outperform a current electrode, activated carbon^{30,42}. Electrodes for battery applications are also relevant. The redox chemistry of the metal sites of MOFs can be used for cathode materials⁴³. However, the limited number of metal sites per weight restrict the specific capacity. 2D π MOFs as an anode materials have not been demonstrated yet, but they have potential to beat graphite if lithium atoms can be stored in the pores as well as intercalated between the layers.

Also, 2D π MOFs are ideal for sensor applications. Many reports show that the electrical conductivity is environmentally sensitive^{15,17,18,26,44–48}. The porous structure can maximize the sensitivity and filter larger molecules. The chemical tunability can optimize selectivity for a specific sensing application. Calculations show that the adsorption can slightly modify energy bands which could modulate carrier density. Experimental demonstrations of carrier density or mobility changes upon the adsorption are required to understand and boost the sensor performance.

Semiconducting 2D π MOFs can be used as the basis of a field-effect transistor (FET). $\text{Ni}_3(\text{HITP})_2$ based transistors show a charge carrier mobility of $48.6 \text{ cm}^2/\text{Vs}$, a threshold voltage of 1.1 V, and an on/off ratio of 2000⁴⁹. Since the FET measurement can overestimates the mobility, additional verification is required to confirm the value⁵⁰. The narrow bandgap of this MOF leads to the low on/off ratio, but the mobility is comparable to poly-crystalline silicon.

Considering the small grain size (<100 nm), improvement in growth could advance the FET characteristics. Potentially FET devices can be combined with sensor applications to maximize the sensing performance. For example, different gases change the Fermi level in a 2D π MOF, and we could sense multiple species by tuning the Fermi level by gate voltage.

Ferromagnetic 2D π MOFs can be useful as it is a porous magnet. Although experimentally demonstrated ferromagnetic 2D π MOFs have a low Curie temperature of 20 K⁵¹, theoretical calculations show great promise^{52,53}. They can be used as a magnetic sensor, for magnetic separation, and as low-density magnets. Also, the ferromagnetism can break time-reversal symmetry. In combination with other characteristics, this can lead to exotic properties such as the anomalous quantum Hall effect.

Last, 2D π MOFs have an atomically flat structure and are compatible with conventional 2D materials. If synthesized with a particular crystalline structure, the 2D π MOFs can be transferred to the surface of a 2D material, imprinting the periodicity of the MOF and tuning the properties of the 2D material. The extremely tunable nature of 2D π MOFs will enrich the platform of 2D materials. So far no experimental work has been demonstrated related to this topic. Large single crystal growth is absolutely necessary to achieve this, and monolayer growth is also crucial for further improvement.

2. Growth of 2D π MOFs

Growth of single crystal growth is the key element to unlock the great potential of 2D π MOFs. As briefly discussed in chapter 1.2.2, all the reported electrical properties are characterized from pressed pellets^{17,20–22,26,27,29–31,35}, aggregated thin film^{18,19,23–25,28,32–34} or single crystal along out-of-plane direction¹⁶. Therefore, the intrinsic electrical properties within the 2D plane of 2D π MOFs have never been explored.

To understand the fundamental properties of 2D π MOFs, single crystal studies must be carried out. The electrical properties are expected to be anisotropic due to their two-dimensional structure. Especially, 2D-plane properties are of great interest due to their π -conjugated nature. As discussed in chapter 1, all the expected interesting properties are 2D-plane properties. The out-of-plane properties are less interesting because the 2D layers are weakly bonded by van der Waals forces. Polycrystalline samples will have a mixture of in-plane and out-of-plane transport. They also possess grain boundaries which distort their electrical properties. Moreover, the polycrystalline samples are purified by washing with solvents which cannot remove all impurities and residual side products. Grain boundaries in particular can accommodate residual side products and impurities. They can also hold electrical dopants which makes accurate control of doping challenging. A single crystal is free from these additional sources of impurities. Lastly, the 2D domain size of the polycrystalline samples is typically smaller than 100 nm, and they can include small crystals with several tens of nanometers size. Domain sizes can be below 10 times the lattice parameter due to the large unit cell of MOFs. Like quantum dots, those small crystals will have different properties compared to large crystals.

To grow high-quality single crystals, we need to understand the growth of 2D π MOFs comprehensively. In this chapter, I will analyze the challenges in 2D π MOFs growth and

describe conventional growth methods. Based on the problem definition, I will introduce my growth method which solves the issues and generate single crystal plates of 2D π MOFs. The growth mechanism and important growth parameters will be explained. Additionally, vacuum process growth will be discussed.

2.1. Why is 2D π MOF growth challenging?

There are many ways to grow materials, and arguably the most popular methods utilize supersaturation as a driving force for the growth. The phase diagram gives us information on the stable phase at equilibrium for a given temperature and pressure. If we start from a liquid or vapor phase and bring the temperature down to make the solid phase as the equilibrium phase, the supersaturation drives the nucleation and growth. Classical nucleation and growth theories are based on this type of growth⁵⁴. They are well understood and high-quality crystals with large size can be obtained with various methods including the famous Czochralski process⁵⁵. Unfortunately, this is not applicable to the growth of 2D π MOFs. MOFs normally decompose before they melt and limited numbers of MOFs can exist as liquid phase⁵⁶.

What is the driving force for the 2D π MOFs growth? It is a chemical reaction. The exothermic reaction of organic ligands and metal ions makes the combination more stable. This is a more complicated kinetic process because there is a high activation energy, unlike supersaturation. Moreover, the overall reaction may depend on multiple intermediate reactions⁵⁷. Indeed, reported 2D π MOFs require initial oxidation of the organic ligands with subsequent deprotonation and bonding to metal ions. Furthermore, the organic ligands usually have multiple redox states. To form a MOF, they need to be in a specific redox state. For HHTP based MOFs, HHTP should be half oxidized which is one of the seven possible redox states shown in Figure 2-1. Therefore, for successful growth the challenge is to realize precise control over the oxidation

states of the organic ligands and also overcome the activation energy. To illustrate the complexity consider an increase in the reaction temperature, it can promote the reaction kinetics, but it also affects the oxidation states of the organic ligands.

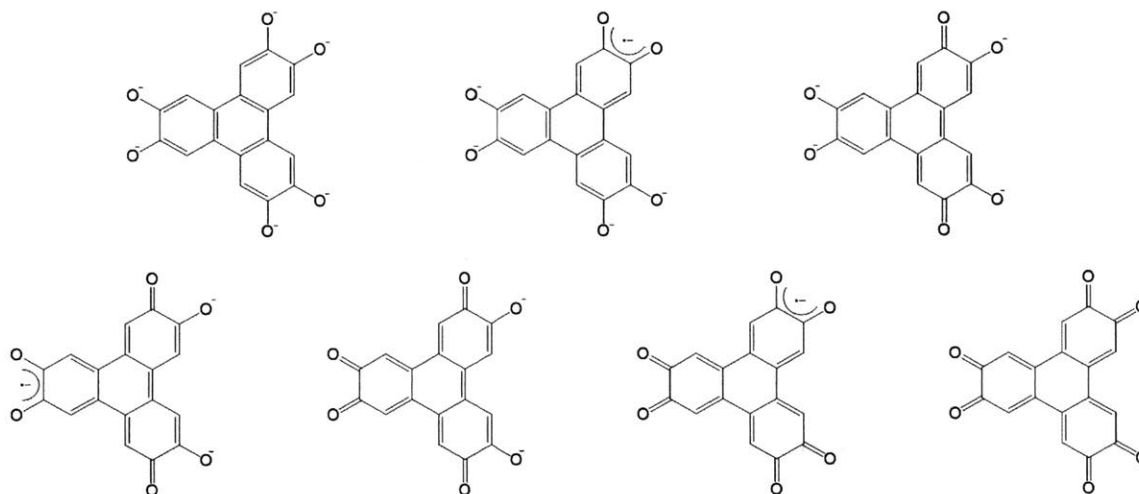


Figure 2-1 Redox states of deprotonated HHTP. For the MOF reaction, it needs to be half-oxidized which is the structure at the bottom left

Another major difficulty originates with the constituent organic molecules. Typically, crystal nuclei are very unstable at the initial stage of growth due to their high surface to volume ratio⁵⁴. The surfaces are unstable because surface atoms have dangling bonds (*i.e.* unsatisfied valence). These unstable nuclei help the growth because they grow quickly to minimize the surface to volume ratio. However, if the building block is a molecule, the situation is different. The molecules do not have dangling bonds and the surface is not as unstable. These stable nuclei especially retard in-plane growth.

The stable nuclei cause another issue. If they have dangling bonds, they will bond to remove the dangling bonds which leads to growth along 2D plane. The stacking does not help to

reduce the dangling bonds. For 2D π MOFs, however, they tend to stack faster than to form a chemical bonding in a 2D plane. This results in the needle shape of crystals and the cross section of the needle is the 2D plane^{16,17,24,29}. If we are interested in the 2D-plane properties, we need to grow plate-shape rather than the needle shape.

The challenges can be summarized as below

- High activation energy is required for a chemical reaction which results in a slow reaction.
- Demanding chemical reaction requirement. The oxidation state of the ligand is especially important.
- Stable crystal nuclei slow down the reaction.
- The stable nuclei stack in the out-of-plane direction which results in an undesired needle morphology.

2.2. Reported growth methods and problems

In this section, I will explain the major growth methods that have been applied to 2D π MOFs. The growth mechanisms of the methods are analyzed and I will explain why these methods have achieved limited success based on the challenges described in the previous section.

2.2.1. Single-phase solution growth

This is the simplest and the most popular way to grow 3D MOFs⁵⁸. The reaction proceeds when metal salts and organic ligands are dissolved together in a solvent. In many cases, the reaction is carried out at high temperature but it can be done at room temperature depending on the constituent chemical reactions as shown in Table 1-1. If the reaction temperature exceeds

the boiling point of the solution at atmospheric pressure it may be performed in an autoclave at higher pressure, in which case the growth method is called solvothermal (or hydrothermal if solvent is water).

Unlike 3D MOFs, 2D π MOFs have strong anisotropy in growth rates along the in-plane and out-of-plane crystalline axes. 2D plane growth involves chemical reactions and out-of-plane growth is based on stacking between the layers with van der Waals forces. If a monolayer of 2D π MOFs can be stabilized in a solvent, stacking would not be an issue. Evans *et al* found cosolvent that stabilize colloidal suspension of 2D COFs (Covalent-Organic Frameworks), and they could grow micro-size single-crystal plates⁵⁹. But 2D π MOFs typically forgo solvation in favor of stacking in aggregates. Consequently, the stacking rate is fast and it competes with the 2D growth rate. Ideally, we want to have much faster chemical reaction rate than the stacking rate to grow plate-shape crystals so that we can explore and take advantage of the 2D properties of the materials. Unfortunately, it is challenging to slow down the stacking rate and resulting morphology of the crystal is a needle shape. Note that the cross-section of the needle is the 2D plane which means the stacking rate is much faster than the chemical reaction rate.

Another issue with this method is a small 2D crystal size. For the small nuclei to grow, reactants need to be continuously supplied to the nuclei. However, the continuous supply of reactants is challenging because the nuclei are precipitated and deposited at the bottom or floated on top of the solvent. Due to the continuous precipitation, the small crystals are deposited with others and have limited exposure to reactants. Also, the reaction volume is too large and reactants are uniformly dispersed in the solvent. Consequently, the reactants bump into each other before they find the nuclei, and they form other nuclei. Because of the large reaction volume and coexistence of both reactants in the same solution, it will continuously generate

small nuclei rather than growing them bigger. In addition, the slow growth rate of the 2D π MOFs for the reasons explained in section 2.1 makes the crystals even smaller.

Although they are small and tends to have a needle shape, the crystallinity of the crystals is good as it can be performed at a high temperature. Insufficient supply of energy to the system often leads to limited crystallinity^{58,60}. The high temperature increases the reaction rate as reactants can easily overcome the activation energy. Also, it increases reaction rate for reverse reaction rates. Consequently, the reaction can be reversible, if the activation energy is much higher than enthalpy of the reaction. This will help to fix defects and drive to high-quality crystals. The high temperature, however, could reduce the Gibbs free energy of the reaction because forming a MOF is not favored in terms of entropy. Also, it might affect the oxidation status of ligands as well. As the temperature is crucial parameter, the best advantage of this growth method is the access to wide range of temperature.

2.2.2. Liquid/liquid interfacial growth

Liquid/liquid interfacial growth uses two solutions which are insoluble in one another. One solution contains metal salts and the other contains organic molecules. Placing the two solutions in a container forms a liquid/liquid interface. The chemical reaction happens only at the interface so the reaction volume is much smaller than the previous method. The small reaction volume increases nucleation density. The higher nucleation density could lead to growth of nuclei by coarsening⁵⁴.

The reactions, however, are proceeded at room temperature^{21,23,27,28,32,34}, or a low temperature³³. As temperature is the key growth parameter as explained in the previous section, the insufficient supply of energy offset the advantages of interfacial growth. It is not clear why

the low reaction temperatures are used, but it might be due to the evaporation of solvents or reduced miscibility.

Despite the problems, liquid-liquid interfacial growth gives a smooth film with the thickness of the film controllable by adjusting the reaction time. As shown in Table 1-1, many groups have used this method to grow films prior to electrical characterization of their properties.

2.2.3. Liquid/gas interface

In this method, only a small amount of organic ligand is dispersed on the surface of the metal ion solution. The film density can be further improved by the Langmuir–Blodgett (LB) method. This method is ideal to grow a large area thin film. However, the temperature should be kept low to prevent evaporation of the solvent. This leads to low crystallinity. One study reported a large standing film of the $\text{Ni}_2(\text{HHTP})$, but atomic defect level was 35%⁶¹. Another report¹⁹ measured the electrical conductivity of $\text{Cu}_2(\text{HHTP})_3$ grown by LB method and it is 2 orders of magnitude lower than other reports which use a different growth method as shown in Table 1-1. This suggests a poor quality film. Nevertheless, if we can increase the growth temperature, this approach can potentially give large single-crystal monolayers of 2D π MOFs.

2.2.4. Coevaporation

This method is performed by thermal coevaporation of organic molecules and metal under high vacuum. It is cleaner and easy to grow monolayer. So far, reported works have a small grain size of the MOFs (<50 nm)^{62,63}, and research has been focused on characterizations with scanning tunneling microscopes. One of the major obstacles might be to fulfill the reaction condition. It is hard to selectively oxidize the ligand under vacuum. Further study is required to solve this problem and obtain large monolayers of MOFs.

2.2.5. Summary of the limitations

Table 2-1 summarize the advantages and disadvantages of the reported growth methods. The single-phase solution growth needs to increase the nucleation density or find a stabilization solvent to achieve large plate shape crystals. The interfacial growth methods need to improve the crystalline quality. For the vacuum process, construction of the proper chemical reaction environment is the key to improve the quality of the crystals.

Reaction environment	Good	Good	Good	Challenging
Crystallinity (High Temperature)	Good	Not Good	Bad	Good
Nucleation density	Low	High	High	.
$\frac{2D \text{ growth rate}}{\text{Stacking rate}}$ (Ratio)	Slow	Slow	Fast	Fast
Typical growth outcome	Small Needle shape crystals	Small grain film	Small grain thin film	Small grain monolayer

Table 2-1 Summary of the growth methods and their strong and weak points.

2.3. Solid-liquid growth

To grow large single-crystal plates, I started from single-phase solution growth. The key is to increase the nucleation density and 2D growth rate and slow down the stacking rate. First, an organic ligand, 2,3,6,7,10,11-hexahydroxytriphenylene (HHTP), is vacuum thermal evaporated onto a substrate and nickel acetate is drop-casted on another substrate. Then, the two substrates are pressed together so that the two reactants are facing each other. Teflon-coated

magnets are used to press them with pressure of 50 kPa at room temperature, and they are placed in water and heated to 95 °C. A schematic illustration of the process is shown in Figure 2-2 (b). This results in large single crystal plates as shown in Figure 2-3. Typical growth conditions are 40nm of HHTP, drop-casted film of nickel acetate from 20 μl of 10 mM methanol solution, and 12 hours of reaction time. With these conditions, micrometer-scale single-crystal plates are grown with high reproducibility. The growth condition occasionally gives large (over 10 μm) crystals, and the probability of getting large crystals increases by starting with a thicker HHTP film. The diagonal of the crystals was 10 to 100 times larger than their thickness. The thickness can be varied by the amount of the reactants and reaction times.

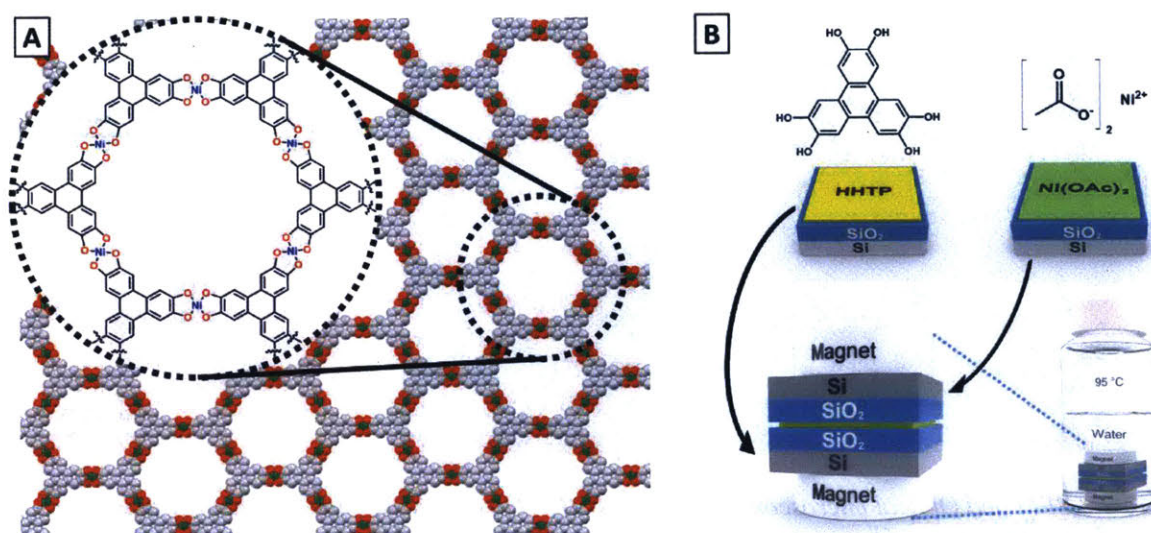


Figure 2-2 Growth of single-crystal plates of $Ni_3(HHTP)_2$. (a) Chemical structure of $Ni_3(HHTP)_2$. (b) Schematic illustration of the growth method. The HHTP film is grown by vacuum thermal evaporation, and nickel acetate is drop-cast on a separate substrate. The two substrates are pressed together with a teflon-coated magnet, and placed in water. After, the vial is kept in a 95 °C oven for a designated time to grow the 2D π MOF. A high nucleation density boosts crystal formation, and the tight reaction space promotes larger crystal growth. Also, the high reaction temperature gives rise to high crystallinity. In addition, the horizontal alignment of HHTP increases the 2D growth rate. Typically, I use a HHTP film thickness of 40nm and reaction time of 12 hours to grow single-crystal microplates. Under these conditions, the biggest crystal obtained from an independent run is at least 5 micrometers in diagonal on the 2D plane.

The growth method is designed to fulfill the following conditions. First, the growth temperature is high to ensure high crystallinity. Second, we reduce the reaction volume small by limiting the growth space between the two substrates. The low water solubility of HHTP ensures that the nucleation takes place at the HHTP film. This generates a high nucleation density which leads to the growth of nucleates. Also, the narrow reaction space may slow down the stacking of the nuclei. Lastly, HHTP is horizontally aligned in the film to increase the 2D plane reaction rate. For these reasons, the beautiful single crystal plates are generated.

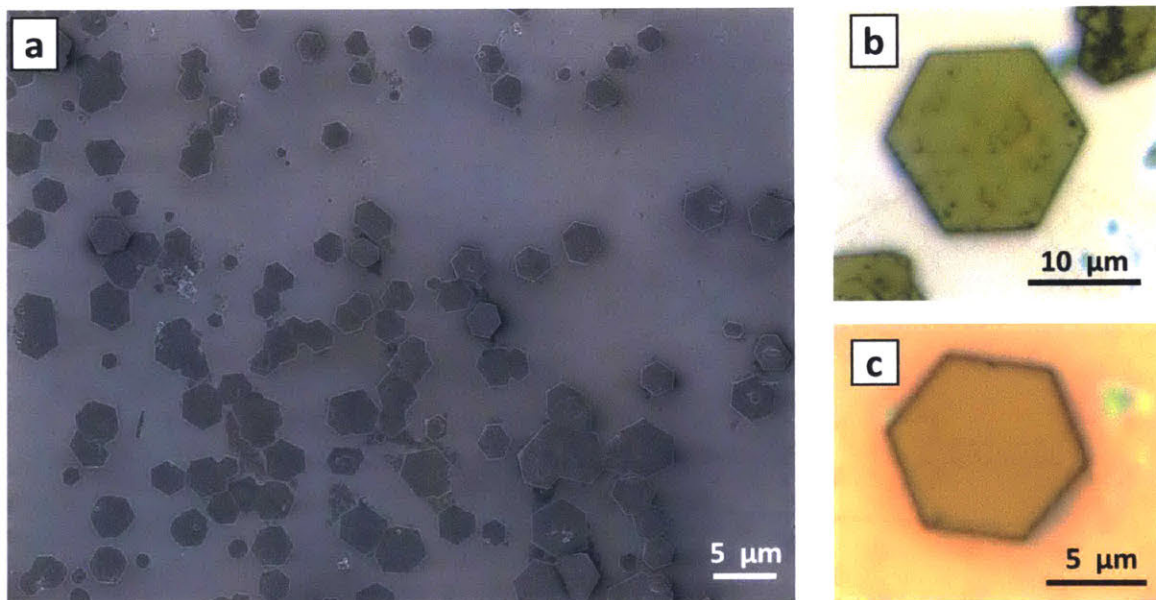


Figure 2-3 SEM and Optical microscope images of $\text{Ni}_3(\text{HHTP})_2$. (a) SEM image of the growth result. Sharp edges and corners of hexagons suggest high crystallinity of the crystals. (b,c) optical microscope images of a single-crystal plate on a Si/SiO_2 (285 nm) substrate.

The detailed growth procedures are as follows. The silicon substrates are cleaned with sonication of acetone and isopropyl alcohol (IPA) following with boiling in IPA. The substrates are loaded in a vacuum thermal evaporator and HHTP is evaporated below 3×10^{-6} Torr. The evaporation rate is between 0.3 \AA/s and 1.5 \AA/s . The growth is insensitive to the evaporation rate.

10mg of nickel acetate ($\text{Ni}(\text{OAc})_2$) is dissolved in 4ml of methanol and 10 μl of the solution is drop-casted onto the substrates two times. Once the drop-casted film is dried, the HHTP substrate and $\text{Ni}(\text{OAc})_2$ substrates are pressed together with Teflon coated magnets and placed in a 20ml vial which contains 4 to 10 ml of water. The vial is placed in a 95 °C oven for 12 hours to grow the crystals. After the growth, the vial is cooled down to room temperature naturally and the substrates are rinsed with water and dimethylformamide (DMF). HHTP (95%), Nickel acetate (99.999%), Teflon coated magnets (TEF-D0050) and Si/SiO₂ (285nm) substrates are purchased from TCI America, Alfa Aesar, SuperMagnetMan, and Nova electronic materials respectively.

2.4. Growth mechanism

2.4.1. Reaction time and growth

To check how the crystals grow, I varied the reaction time and characterized the growth outcomes as shown in Figure 2-4. After only 30 minutes of growth, a few micrometer size plates are already formed. Note that the surroundings of the crystals have similar height. This indicates that HHTP film was not fully dissolved to water or reacted with nickel ion. Most plates are sitting on the substrates but some of them are standing. This might be related to the alignment of HHTP which will be discussed in the following section. HHTP film is primarily horizontally

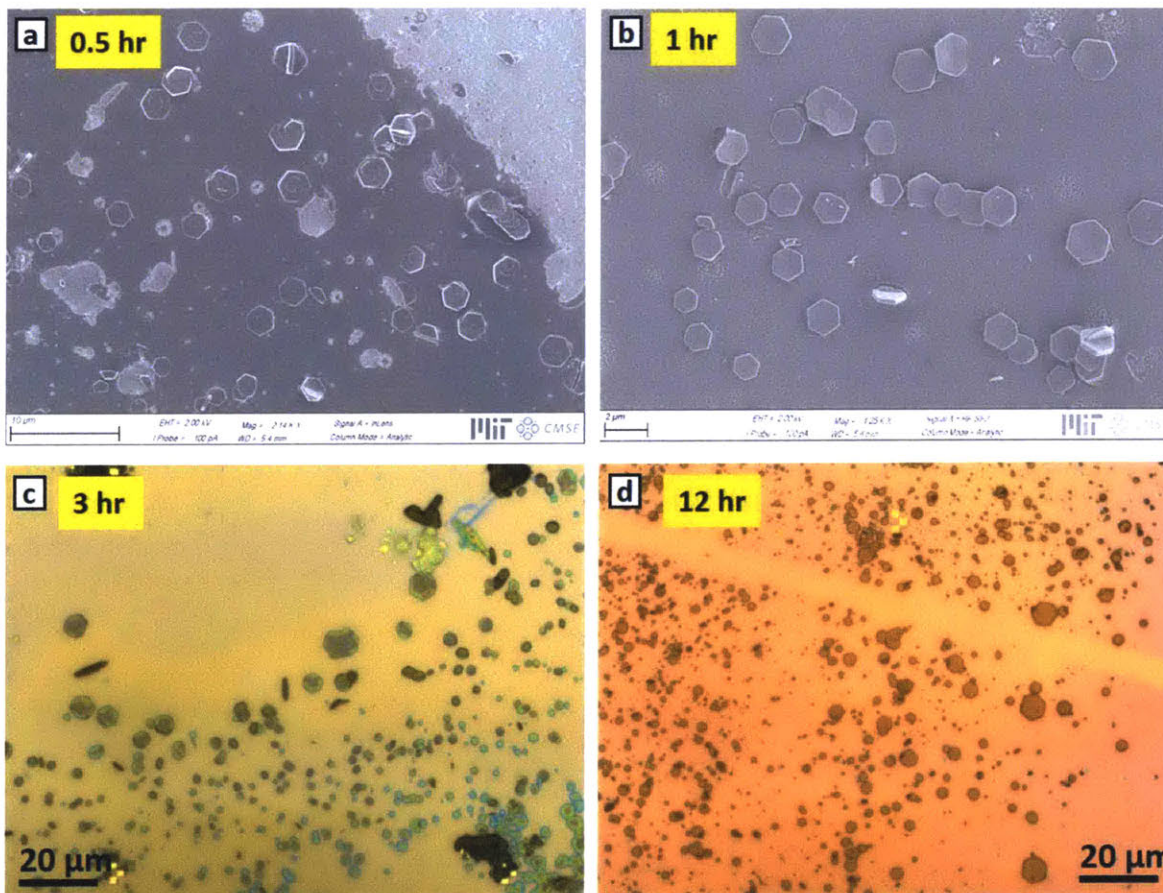


Figure 2-4 Growth results from different growth times. (a) half hour, (b) 1 hour, (c) 3 hours, (d) 12 hours of the reaction. Note that (a) and (b) are SEM images and (c) and (d) are optical microscope images. Also the scale bars are different for the images.

aligned but it is not a crystalline film. some crystals might detach and then reattach in a different orientation. After 1 hour of reaction, the crystal plates continuously grow or start to merge as you can see in Figure 2-4 (b). The crystals are thicker than surroundings which means more HHTP molecules are consumed by dissolution to water or reactions with nickel ions. After 3 hours of reaction, the crystals grow bigger from reactions or merging between crystals. The edges and corners of the crystal are still ill-defined. Also, the color of the crystal is not uniform which indicates the irregular thickness of the plates. Dissolved small nuclei are stable because of the lack of dangling bonds, so they stack on each other to minimize the surface energy rather than undergoing a chemical reaction. After 12 hours of reaction, the quality of the crystal is

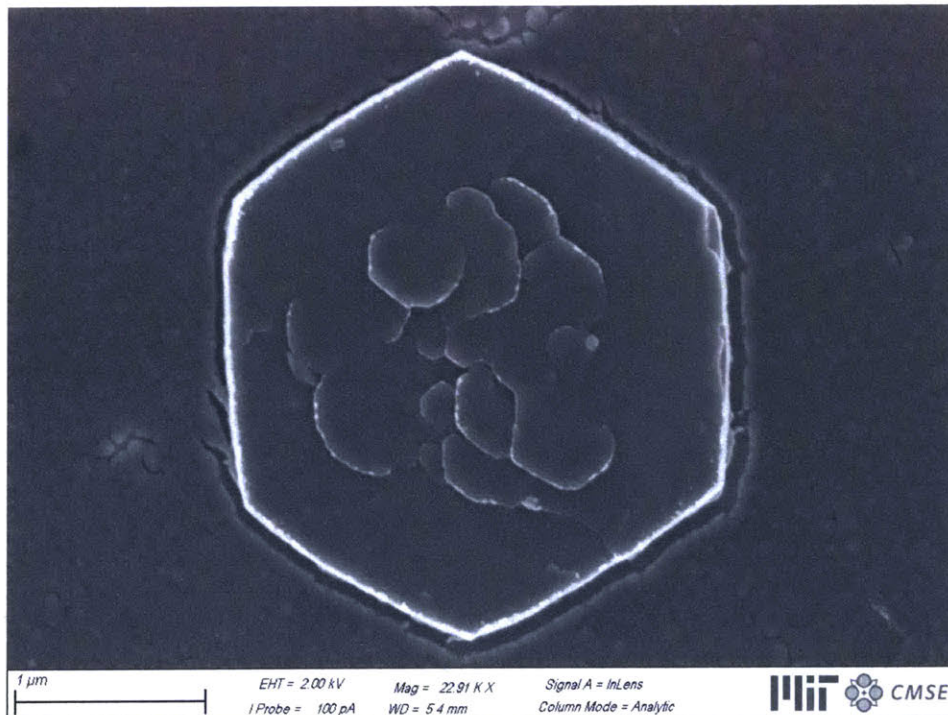


Figure 2-5 Higher magnification SEM image of a crystal after half hour reaction. Multiple spiral growth is happening on the surface of the crystal.

significantly improved. This proves that the coordination bonding is reversible with a given thermal energy and that crystals can fix defects to minimize their energy.

It is interesting to note multiple examples of spiral growth on the crystals in the early stage of the growth. This can be seen in Figure 2-4 (a) or more clearly in Figure 2-5. Typically, spiral growth is initiated by dislocations along c-axis⁵⁴. In this case, however, the growth step is beyond a monolayer in thickness which means that the spiral growth is started by the rough surface rather than a dislocation. The interpretation is aligned with the multiple examples of spiral growth site on a crystal. The rough surface might be originated from roughening phenomena at elevated temperature⁵⁴ or stacking of small nuclei on the surface. The spiral growth is difficult to observe at longer reaction time. It is probably because more nuclei sit on the surface, becoming indistinguishable and roughening the surface.

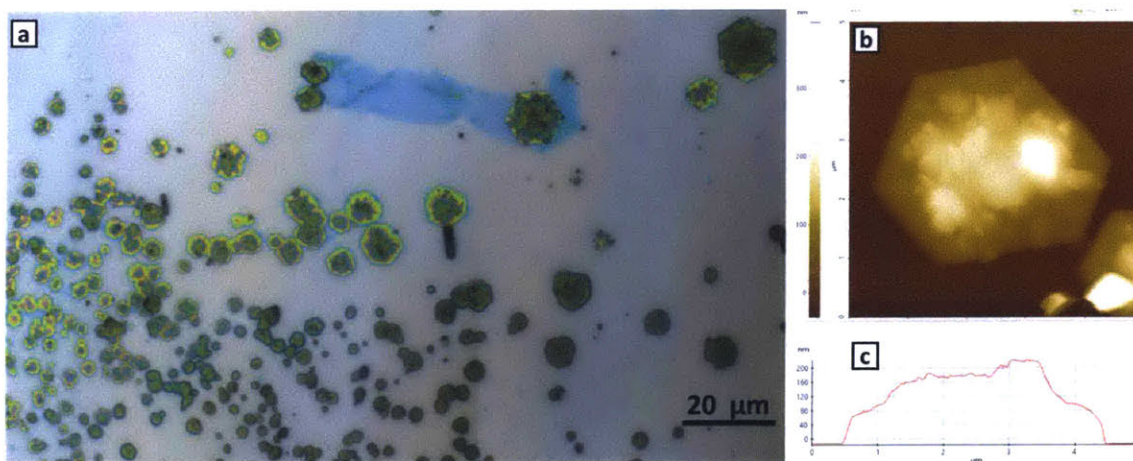


Figure 2-6 Growth with the addition of 5mg of Na(OAc) to water. It makes the pH of the water around 8.5. The reaction time is 3 hours, but the crystals have sharp edges due to the increased reaction rate. (a) optical microscope image (b) AFM image (c) cross-section profile of the AFM image

A mild basic environment tends to help the formation of the coordination bonding.

Therefore, the addition of sodium acetate (Na(OAc)) could increase the growth rate and

crystallinity. 5mg of Na(OAc) was added to the 5ml of water which makes pH of 8.5. To check the effect, I grew the MOFs for 3 hours. As expected, the crystals have sharp edge and corners even with 3 hours of reaction as shown in Figure 2-6. Still, the stacking of small nuclei is problematic as is evident from the irregular color of the crystals and the atomic force microscope (AFM) image. The downside of using Na(OAc) is that it could be trapped in the MOF crystals and increase the elemental impurity level.

Although the surface is not uniform at the early stage, it becomes more uniform with longer reaction time. Example AFM images of 12 hours reaction crystals are shown in Figure 2-7.

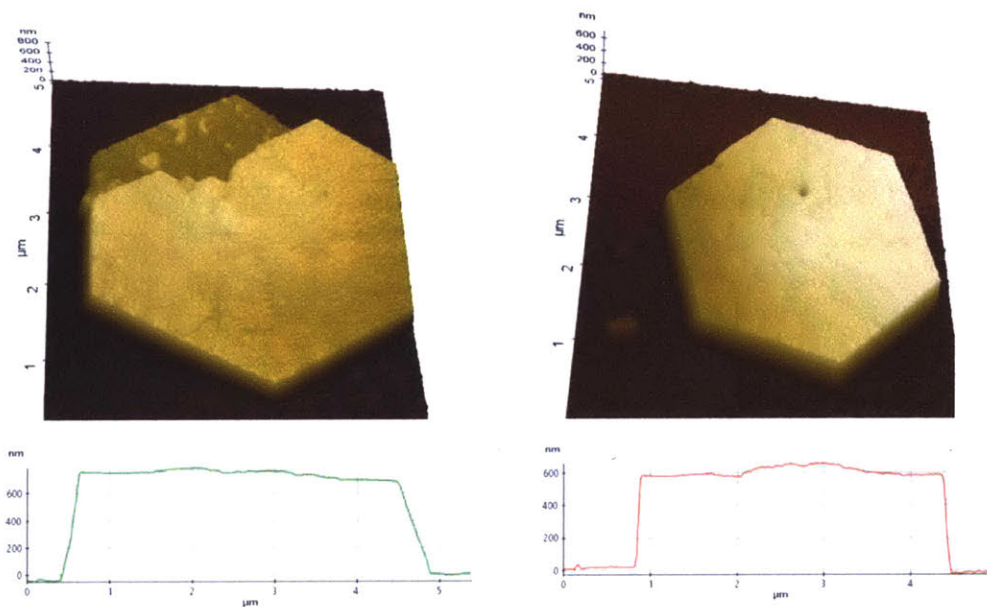


Figure 2-7 AFM images and cross-sectional profiles of crystals after 12 hours of reaction. The surface is much smoother than shorter reaction-time samples.

2.4.2. Proposed growth mechanism

Based on the above observation, we propose growth mechanism as shown in Figure 2-8. key points of the growth method are, solid phase of HHTP, alignment of HHTP, small reaction volume, and high reaction temperature which addresses the growth problems listed in the previous chapter.

The growth method starts with a horizontally aligned film of the organic ligands. Small molecules can be aligned by vacuum thermal evaporation if they have a planar shape and strong

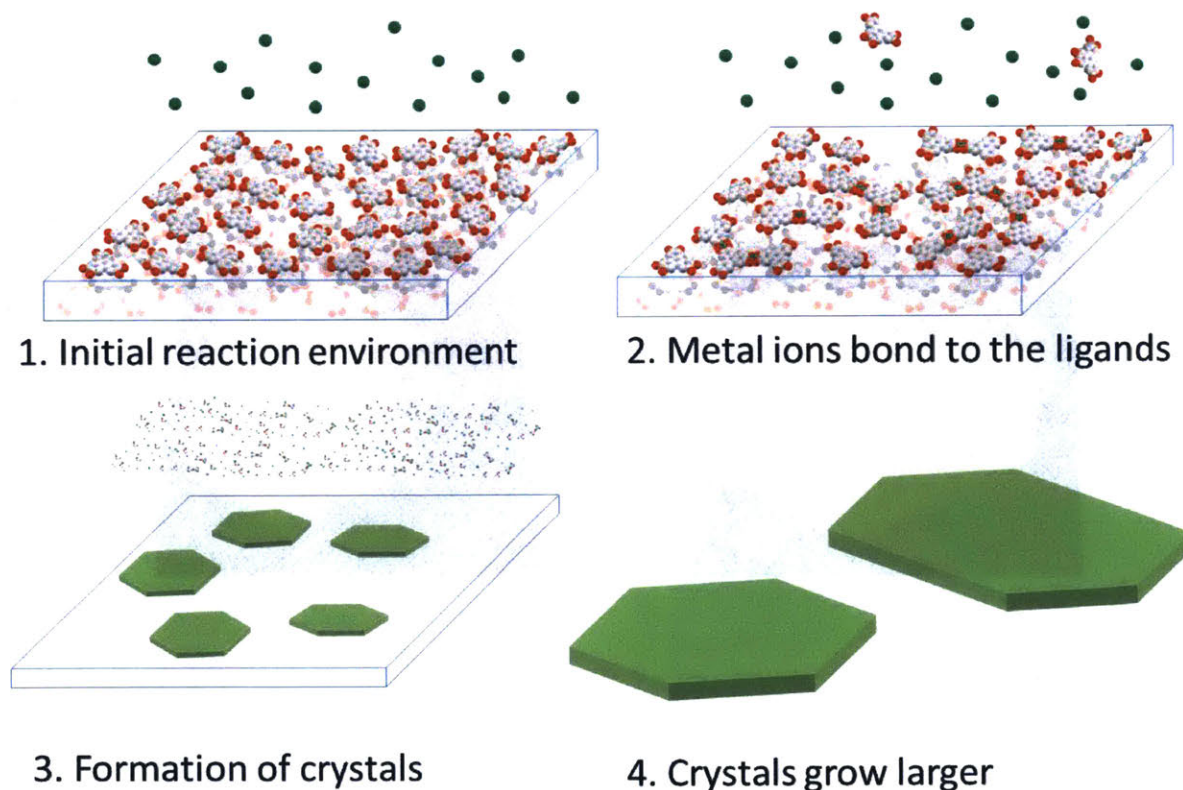


Figure 2-8 Schematic illustration of the proposed growth mechanism. Initially organic ligands remain as an aligned solid film. The dissolved nickel ions meet the ligands and form the coordination bonding. At the same time some molecules or HHTP-Ni complexes can be dissolved into the water. As more ligands are connected it starts to form a crystalline facet. At this stage, there are still abundant HHTP or HHTP-Ni complexes around the crystals if the initial HHTP thickness is more than 30 nm. As the reaction continues, the crystals grow through the supply of HHTP and nickel, or by merging with other crystals. High temperature fixes defects and increases the crystallinity with longer reaction time.

intermolecular bonding such as hydrogen bonding⁶⁴. HHTP is planar and has strong hydrogen bonding. A molecule with a similar structure, HATCN (1,4,5,8,9,11-Hexaazatriphenylene-hexacarbonitrile), also exhibits horizontal alignment⁶⁵. Indeed, an ellipsometric measurement of the film gives higher ordinary refractive index than extraordinary index (Figure 2-9). HHTP is a

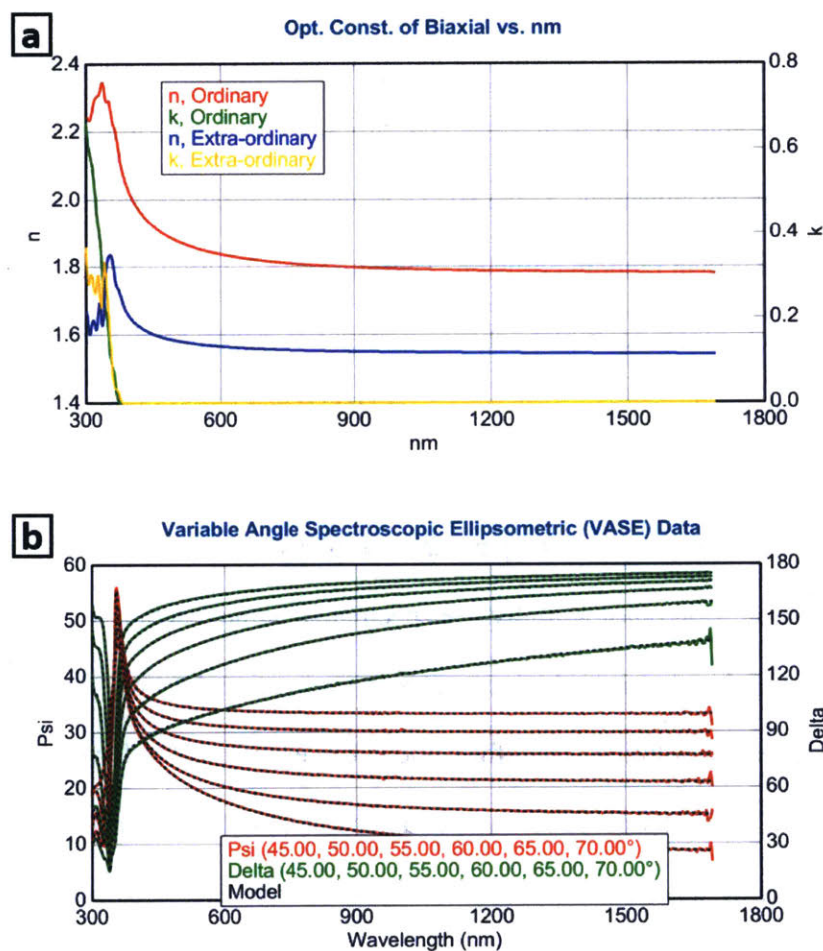


Figure 2-9 Variable angle spectroscopic ellipsometry data of evaporated HHTP film on silicon. (a) Complex refractive indexes of ordinary and extraordinary direction. (b) Fitting result of Psi and Delta for variable angles. The measurement was done by J. A. Woollam M-2000 and WVASE32 instruments. Both gave identical results. The sample was prepared by evaporation of 30nm HHTP on a bare silicon substrate with a native oxide. The measurement angle was 45° to 70° with 5 degree steps. The analysis started using the Cauchy model in the transparent region. Then it was slowly expanded to the whole region by the anisotropic B-spline model satisfying Kramers-Krönig consistency.

planar molecule so it is more polarizable within the molecular plane. Therefore, the higher ordinary refractive index indicates preferentially horizontal alignment of the molecule. If the alignment is completely random the ordinary and extraordinary refractive index should be identical. The order parameter of the film is -0.22. It is -0.5 if the molecules have perfect horizontal alignment, and it is 0 if they are randomly oriented⁶⁴.

When the two substrates are submerged in water, the HHTP film remains in solid phase because HHTP has poor solubility in water and only small amounts of water can wet inside the tight space between the substrates. Since HHTP molecules are in the same orientation, the reaction rate is faster than random collision. Therefore, the 2D growth rate can be faster than the vertical stacking rate resulting in plate-shape crystals rather than needle shape. As a control experiment, we repeat the process with drop-cast HHTP that has random orientation, and it did not generate single-crystal plates (Figure 2-10).

The nucleation density and temperature also plays a crucial role in growth. As the HHTP molecules remain in solid phase initially, we speculate that the reaction occurs at the surface of the film. The nucleation density is high compare to conventional growth methods where organic molecules are spread in solution. Therefore, nuclei can easily meet to form crystals. Even after the HHTP molecules are dissolved to water and become mobile, the reaction volume is small because of the narrow space between the two substrates. This increases the collisions between reactants and crystals which grows the crystals. Unlike the conventional interfacial growth, we could set a high growth temperature because the substrates are submerged in water. The high crystallinity indicates that the reaction temperature is high enough to have reversible reactions. The longer reaction time yields bigger and better-quality crystals.

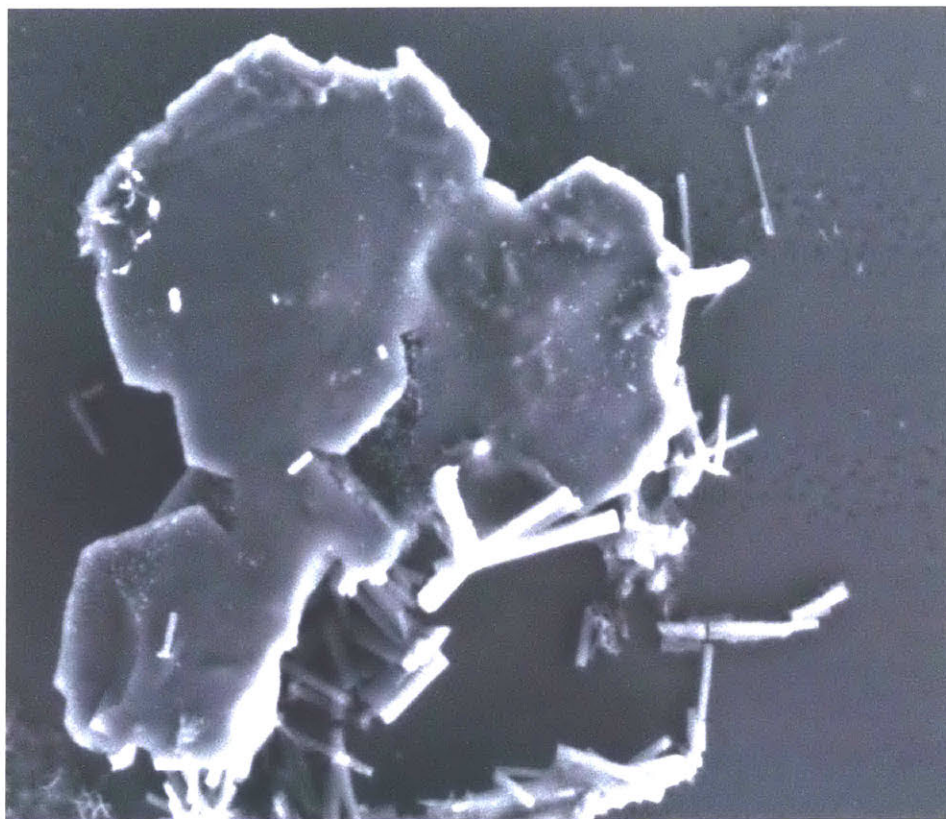


Figure 2-10 Growth with drop-cast HHTP instead of evaporated HHTP film. There was no single crystal plate found on the substrate. The crystals are small and polycrystalline. For the HHTP drop-casting, 10 μ l of 1.7 mM methanol solution is drop-cast two times on a substrate. The HHTP amount is identical to that of 40nm film.

2.5. Growth of other 2D π MOFs

I chose $\text{Ni}_3(\text{HHTP})_2$ to test the growth method. There are several reasons. HHTP is a good organic building block as it is vacuum-evaporable and a good candidate for horizontal alignment. Also, HHTP is commercially available which means it is stable and has less uncertainty on the material quality. Nickel is chosen because its square-planar geometry is stable and its redox state is cleaner. For example, copper can be Cu(I) or Cu(II) but Ni(I) is unstable so the chemistry of the system is cleaner. However, this does not necessarily restrict the technique

to $\text{Ni}_3(\text{HHTP})_2$. Rather, it is important to show the grow method is universally applicable to many 2D π MOFs. Although I have not tried different organic ligands but I did try to change the metal ions. I kept all the conditions but changed the metal ion to cobalt and copper. The cobalt gives beautiful hexagonal crystals as shown in Figure 2-11 whereas the growth with copper was not successful, at least without additional optimization.

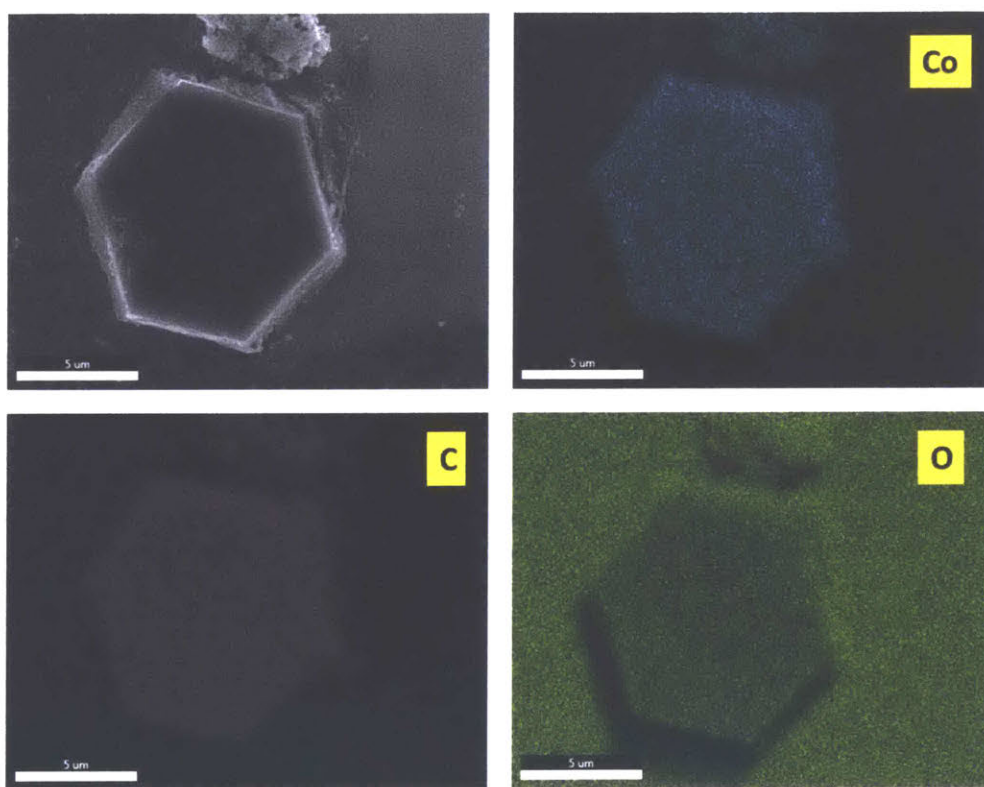


Figure 2-11 SEM image of $\text{Co}_3(\text{HHTP})_2$ and elemental distribution of cobalt, carbon and oxygen. Note that the background oxygen signal originates from the SiO_2 substrate.

2.6. Growth parameters

In this section, I will briefly discuss the effect of many growth parameters besides the reaction time. Due to the number of parameters, I could not test all combinations of the

conditions. Also, there might be a crucial hidden parameter that I did not consider. Therefore, there is considerable uncertainty in the following control experiments.

2.6.1. HHTP related parameters

The thickness of the HHTP layer directly affects the crystal size. Generally, the thicker HHTP leads to thick and large crystals. Typically, 40 nm of HHTP is used for the growth and it generates micrometer scale crystals with high reproducibility. These starting conditions yield at least one single-crystal plate with 2D diagonal of over 5 μm on a substrate. However, the number of the large crystals are greatly varied. With the 40 nm of HHTP, the biggest crystal I grew is 25 μm . As I increase the HHTP thickness, probability of getting larger crystals increased. In other words, thinner HHTP gave smaller MOF crystals. If HHTP thickness is too thin (below 10nm), it was difficult to find crystals with optical microscope. Over 20 μm crystals can be obtained with reasonable yield when the initial HHTP thickness of 100nm is used.

I do not find a correlation between HHTP evaporation conditions and crystal growth. The evaporation rate is in the range of 0.3 A/s \sim 1.5 A/s. The vacuum level is ranged from 3×10^{-7} torr to 3×10^{-6} Torr. The evacuation overnight before the evaporation also does not affect the growth. The alignment of molecules is insensitive to those parameters⁶⁴. However, if we increase the substrate temperature above the glass-transition temperature of HHTP during the evaporation, HHTP is likely to have random orientation⁶⁴. In that case, the growth of plate-shape crystal can be challenging.

Patterning the HHTP film tends to help growth. The possible reasons for the improvement are, (1) The patterning gives more room for the MOF to expand horizontally. (2) Water can wet inside better as the SiO_2 substrate is hydrophilic and the empty space generated by the linear pattern can function as ditch. The effect of the water amount will be discussed in the

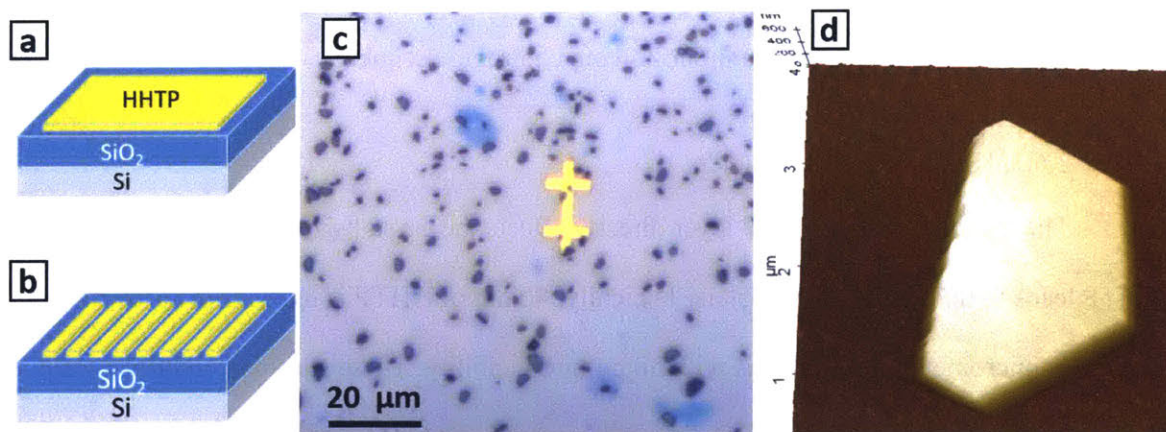


Figure 2-12 Effect of HHTP patterning. Schematic illustration of unpatterned (a) and patterned (b) HHTP films. The line pattern is 0.1-inch-wide with 0.2-inch period. Optical microscope (c) and AFM (d) images of the growth result with patterned HHTP. Generally symmetric hexagonal crystals are obtained, but asymmetric hexagons are also observed. These might be grown from the edges of the line pattern.

following section. Another interesting outcome of the patterned HHTP is the shape of the MOF crystals. Generally, symmetric hexagons are obtained from the growth, but highly asymmetric hexagons are also obtained as shown in Figure 2-12. These crystals might be grown from the edges of the line pattern.

2.6.2. Ni(OAc)₂ related parameters

One of the major uncertainties of the growth method is the drop-cast Ni(OAc)₂ film. 10 mg of Ni(OAc)₂ is dissolved in 4ml of methanol, and typically 10 μL of the solution is drop-cast on a Si/SiO₂ substrate two to four times. Since it is drop-cast, the morphology and uniformity of the film are not controllable. Although Ni(OAc)₂ has a high solubility in water (182 g/L at room temperature), the drop-cast film might not dissolve quickly if the amount of water inside the space between the two substrates is limited. This is speculated to be the major reason of the inhomogeneous distribution of the MOF crystals on a substrate.

The amount of $\text{Ni}(\text{OAc})_2$ is also a crucial factor. Small amount leads to small crystals with good crystallinity, and large amount leads to big crystals with poor crystallinity or polycrystalline film. The ideal amount of $\text{Ni}(\text{OAc})_2$ is about 5 to 20 times of HHTP.

2.6.3. Amount of water between the substrates

This is also one of the most crucial factors. The amount of water affects the chemical environment, especially the oxidation of HHTP, so it affects the 2D growth rate. If dissolved oxygen is the source of the oxidation, a large amount of water can increase the reaction rate. Also, the water amount controls the dissolution rate of $\text{Ni}(\text{OAc})_2$ and the HHTP film. A large amount of water can dissolve them quickly which makes the synthesis similar to conventional single-phase solution growth.

The water amount can be controlled by the distance between the two substrates or hydrophilicity of the substrates. To check the effect, I increased the distance by dispersing $4\ \mu\text{m}$ silica microspheres, defining the minimum distance between the substrates. Interestingly, this does not affect the growth dramatically, and the growth outcome is similar. For 30nm of HHTP on a half-inch substrate, the amount of HHTP per water amount is 1.3 g/L. This exceeds the solubility of HHTP in water. Therefore, the HHTP film remains on the substrate as aligned solid phase and it results in micrometer-scale single crystal plates.

Alternatively, we also tested placing the HHTP substrates in a nickel acetate solution to do the reaction. In this case, HHTP dissolves in water quickly so the MOF crystal cannot be found on the substrate after the reaction. The hydrophilicity of the substrate affects the capillary action of the water. When a bare silicon substrate is used, the number of grown crystals are greatly reduced.

2.7. Vacuum process

A vacuum process has a great advantage over the solution process, because it is cleaner and offers good control over the nucleation. However, the major challenge is to make a chemical environment to do the complicated reaction. In this section, I will describe the vacuum processes I tried and discuss the limitations.

2.7.1. Vacuum reaction

For the vacuum process, I change the material system to copper acetate ($\text{Cu}(\text{OAc})_2$) from $\text{Ni}(\text{OAc})_2$. The reason is that $\text{Ni}(\text{OAc})_2$ decompose before it evaporates whereas $\text{Cu}(\text{OAc})_2$ is evaporable. I started from the evaporation of 30nm HHTP film on a substrate and drop-casting of $\text{Cu}(\text{OAc})_2$ on another substrate. Then I placed the $\text{Cu}(\text{OAc})_2$ substrate on top of the HHTP substrate in a way that they were facing each other. Then they were placed in a vacuum furnace and evacuated for 30 minutes at 30 °C. The furnace was heated up to 250 °C for 20 minutes under vacuum (30 mTorr). It generated hexagonal plates as shown in Figure 2-13. The hexagons are suspected to be $\text{Cu}_3(\text{HHTP})_2$, but it has not yet been characterized due to its small size. Growth parameters need to be further optimized to grow larger crystals. One major issue with this process is the oxidation of the organic ligand. Since it is under vacuum, HHTP can be only oxidized by $\text{Cu}(\text{OAc})_2$. This results in reduced copper crystals which are the bright dots in Figure 2-13. It is confirmed by elemental mapping of the small crystals which tells us that the small crystals only contain copper. If external oxidants such as oxygen are introduced to oxidize

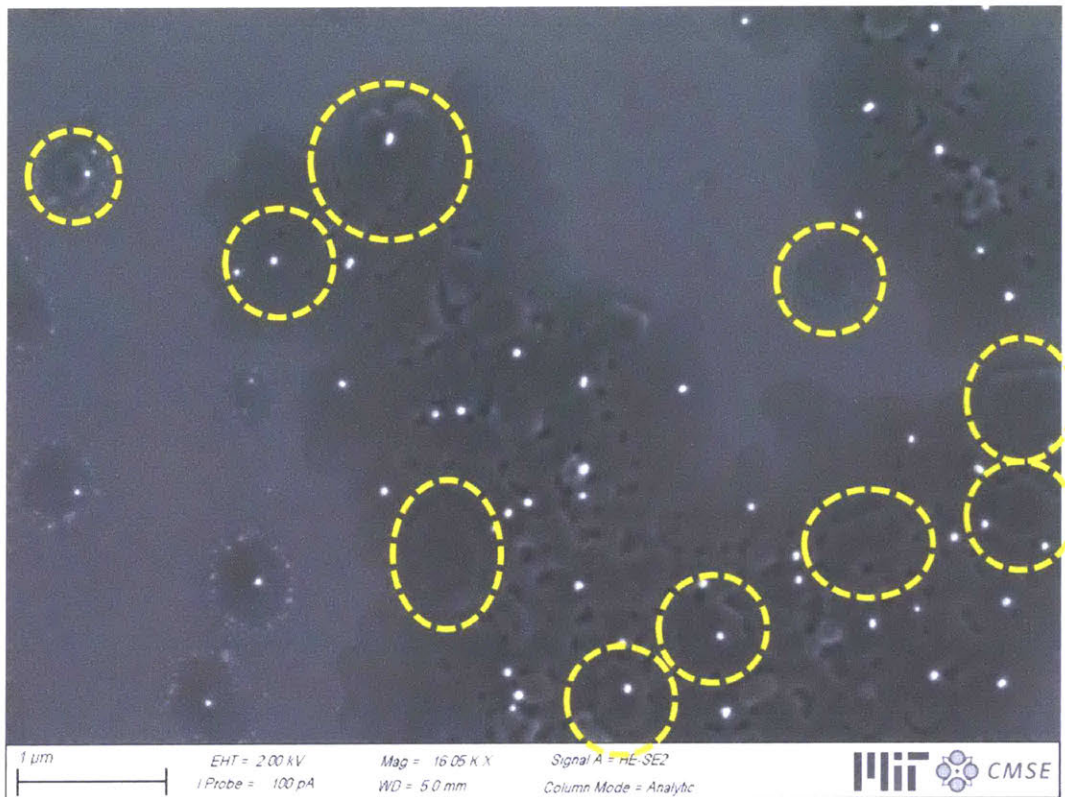


Figure 2-13 Crystals grown by reaction under vacuum. Hexagonal plates are yellow circled. The small bright dots are copper which are reduced from $\text{Cu}(\text{OAc})_2$ probably due to the oxidation of HHTP.

HHTP, it also oxidizes $\text{Cu}(\text{OAc})_2$. If the oxidation issue is not solved, it will always leave small copper crystals on top of the MOF crystals.

2.7.2. Chemical Vapor Deposition

In the previous method, it is difficult to control the flow of copper acetate as the HHTP substrate is covering the $\text{Cu}(\text{OAc})_2$ substrate. A Chemical Vapor deposition (CVD) method separates the two sources and makes them vapor phase for the reaction. Since HHTP has a higher boiling point, the HHTP substrate is placed in the center of the furnace, and $\text{Cu}(\text{OAc})_2$ is placed near the end of the furnace so that two materials boil at the same time as shown in Figure 2-14.

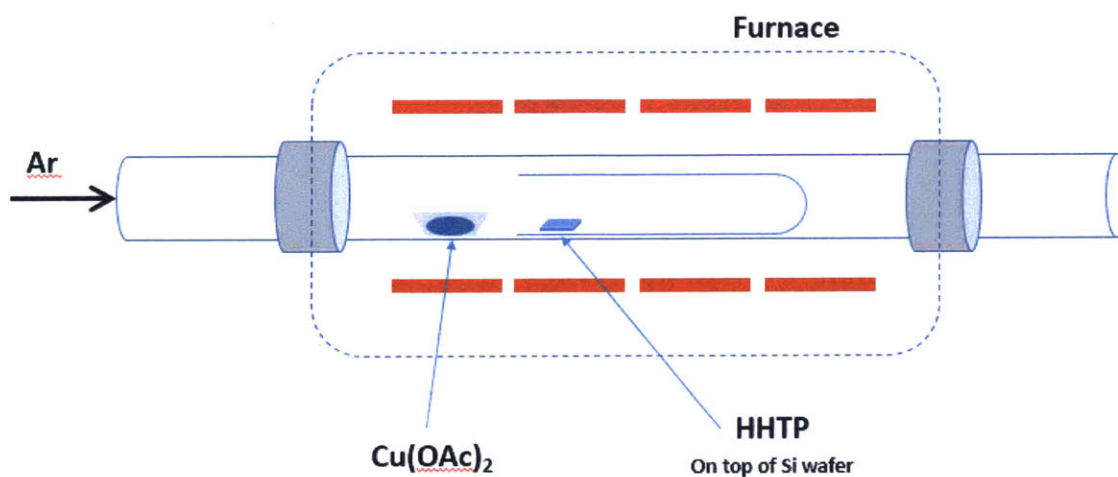


Figure 2-14 Schematic illustration of the CVD setup. HHTP is spuncoat on a silicon substrate and placed in the center of the furnace tube within an additional small tube. The additional small tube increases the concentration of $\text{Cu}(\text{OAc})_2$ around the HHTP substrate. $\text{Cu}(\text{OAc})_2$ is placed near the end of a single-zone furnace so that the two materials evaporate at the same time. Argon was used as carrier gas and a dry pump was used to remove air.

A HHTP film is made by spincoating on a Si/SiO_2 (285nm) substrate. 3 mM solution made with DMF is drop-cast and spun at 7000 rpm for a minute. Then, the HHTP substrate and $\text{Cu}(\text{OAc})_2$ crucible is placed in the tube and evacuated for 30 minutes at 30 °C followed by heating to 300 °C for 20 minutes with an additional 20 minute soak time. Note that an additional tube is introduced to increase the concentration of $\text{Cu}(\text{OAc})_2$ around the HHTP substrate. After

the reaction is finished, it is cooled down to room temperature naturally. Argon flow is maintained at 5 sccm and the pressure is 140 mTorr.

Under these conditions, I was able to get 4nm-thick flakes as shown in Figure 2-15. The surface of the flake is very smooth, comparable to the substrate roughness. Unfortunately, we still have small copper or copper oxide crystals on top of the flake. Probably copper ions are reduced by HHTP and formed the small particles. The identity of the crystals is confirmed by elemental mapping that they are copper or copper oxide crystals. Another unwanted feature is folding or wrinkles of the flake, possibly exacerbated by the high temperature.

We have not directly identified the flake, but it is expected to be $\text{Cu}_3(\text{HHTP})_2$. The flakes do not dissolve in water or ethyl acetate which can easily dissolve HHTP and copper acetate. Also, elemental mapping of highly wrinkled and folded flakes reports the presence of both carbon and copper. A device is fabricated to check its electrical conductivity. Unfortunately, many contacts are open from handling the device so two probe conductivity is measured at ambient environment. The conductivity is 0.01 S/cm which is similar to previous reports (See Table 1-1). Considering the contact resistance and the fact that the conductivity increases by one order of magnitude under vacuum, the actual conductivity of the flake can be much higher than 0.01 S/cm.

Still, the major challenge in this process is to prohibit the production of copper crystals. It is promising that we can grow smooth flake with CVD, but applications will be limited without solving the HHTP-oxidation related issue.

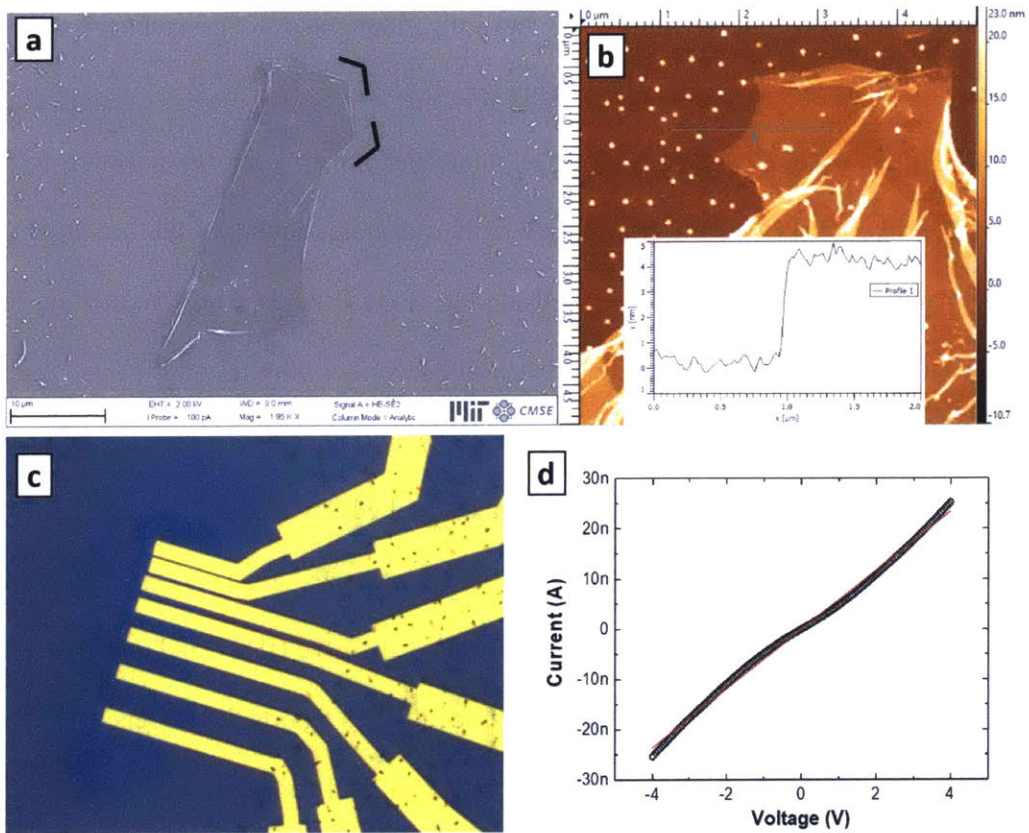


Figure 2-15 A flake grown with the CVD method and its electrical conductivity. (a) SEM image. (b) AFM image. The surface of the flake is as smooth as the silicon substrate. (c) optical microscope image after device fabrication. (d) current-voltage characteristics. Unfortunately, many contacts were open and this characteristic is two-probe data. It deviates a little bit from Ohmic behavior, which indicates a bad contact. The conductivity is estimated to be 1×10^{-2} S/cm which is similar to reported values.

3. Characterization of the crystals

In the previous chapter, I presented optical microscope and SEM images of the single crystal plates. Here, I will show TEM, EDS, UV-Vis-NIR and IR spectrum and discuss the properties of $\text{Ni}_3(\text{HHTP})_2$.

3.1. Powder synthesis

Before I discuss the properties of the single crystals, it is good to compare with powder samples prepared with the typical single-phase solution growth method. The powder was synthesized as follow. 7 mg of HHTP was added to 4ml of water in a 20-ml glass vial. To dissolve HHTP, 0.2 ml of DMF was added. Note that HHTP was not completed dissolved. Then 10 mg of $\text{Ni}(\text{OAc})_2 \cdot 4\text{H}_2\text{O}$ was added and the vial was gentled shaken. The vial was placed in a 85 °C oven for 12 hours. Then it was cooled to room temperature naturally. The crystals were washed with water and acetone 3 times each. At each washing process, it was centrifuged at 3000 rpm for 5 minutes. The powder was confirmed by powder x-ray diffraction (PXRD). The peak locations match well with a previous report¹⁶ and this confirms the synthesized powder

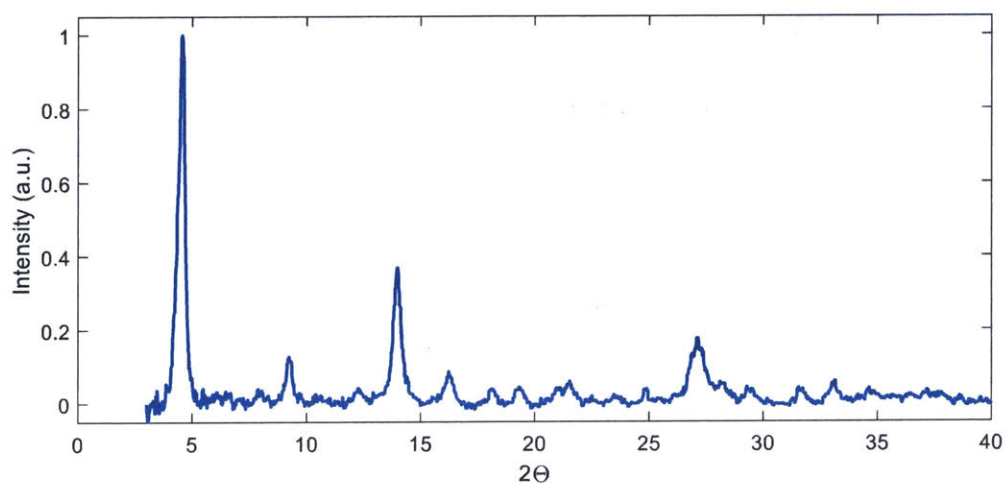


Figure 3-1 PXRD of powder of $\text{Ni}_3(\text{HHTP})_2$. The strong peak at $2\theta=4.555$ degree corresponds to a lattice parameter of 22.4 Å.

was $\text{Ni}_3(\text{HHTP})_2$. The strong peak at $2\theta=4.55$ degree corresponds to lattice parameter of $a=b=2.24$ nm.

3.2. TEM

To check the crystal structure of the single crystal, transmission electron microscope (TEM) is used. Figure 3-2 shows a low magnification image of the crystal. The image was collected with FEI Tecnai G2 Spirit TWIN with the beam acceleration voltage of 120 kV. Due to the large lattice parameter of the MOF, we can see the lattice at the low magnification (52,000 X). Unlike TEM images reported previously, the crystal size is large. The right-bottom corner of

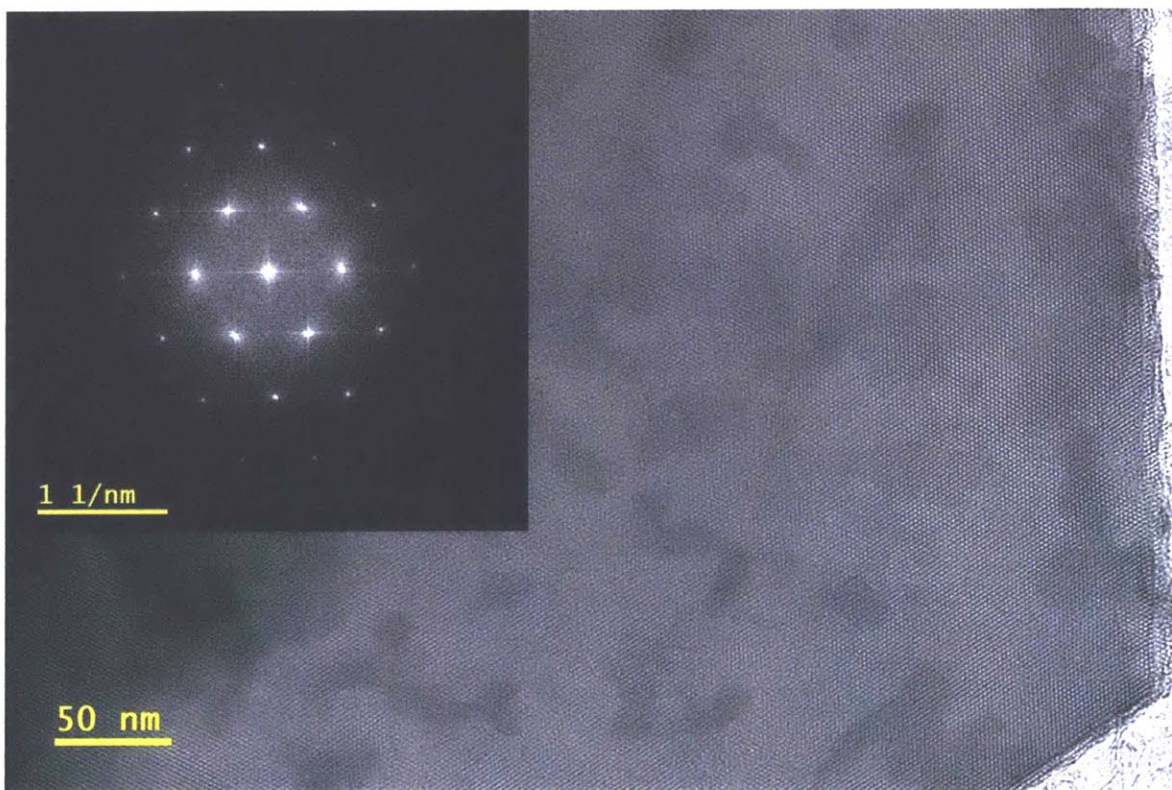


Figure 3-2 Low magnification (52,000 X) TEM image of the crystal. Due to the large unit cell of the MOF, the lattice is visible at this low magnification. It has a uniform hexagonal structure, and the low-bottom corner is the corner of the hexagonal single crystal. Inset: Fourier transform image. It confirms the hexagonal structure with a lattice spacing of $a=b=2.1$ nm which matches well with the PXRD data.

the image is the corner of the hexagonal single crystal. It has uniform hexagonal lattice which proves it is single-crystalline. Also, no dislocations are observed in the imaged area indicating high crystalline quality. The lattice parameter is determined by Fast Fourier Transform (FFT) of the TEM image. The reciprocal vector is 0.55 nm^{-1} which corresponds to the lattice spacing of $a=b= 2.1 \text{ nm}$. This is in good agreement with the PXRD data. The high magnification image is shown in Figure 3-3. In this image the pores of the MOFs are visible and it matches well with the crystal structure.

For successful imaging, the most important thing is sample preparation. Charging of the crystals damages the sample so I use a graphene TEM grid (from Ted Pella inc) to effectively remove the charges from the crystals. The crystals are transferred to the TEM grid as follow.

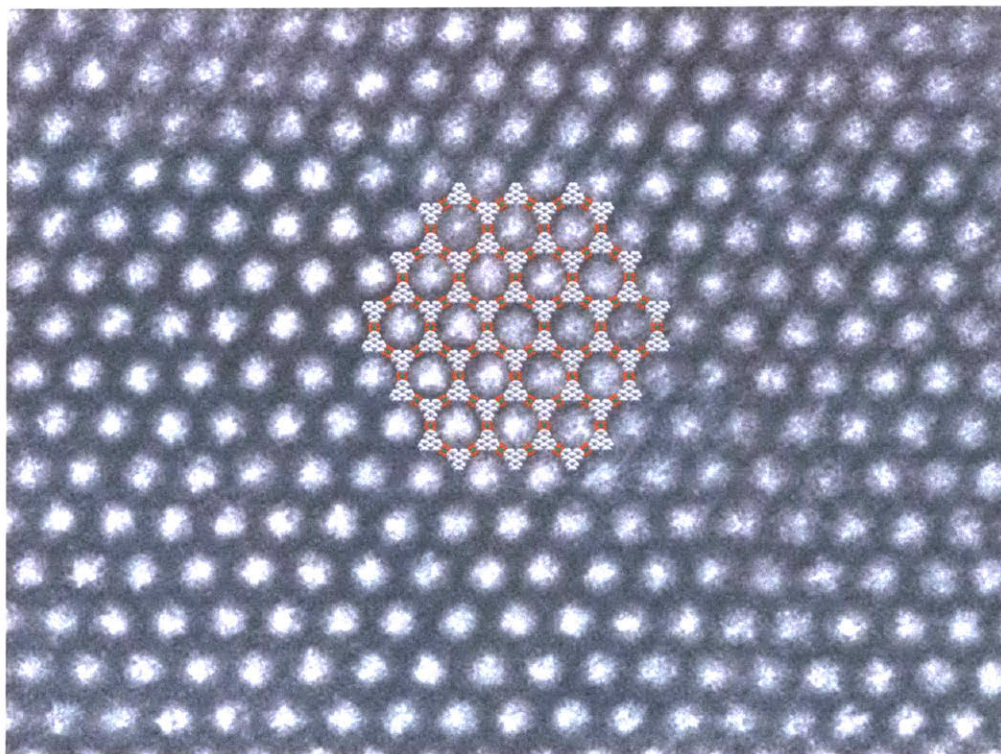


Figure 3-3 The high magnification TEM image. The bright circles are the pores of $\text{Ni}_3(\text{HHTP})_2$. The lattice matches well with the crystal structure of $\text{Ni}_3(\text{HHTP})_2$. It was measured with Tecnai F20 at an acceleration voltage of 120 kV. Estimated electron-beam dose was $10^5 \text{ electrons}/\text{\AA}^2$.

After the reaction is finished, I add 5ml of DMF to the vial. Then I detach the magnets and separate the two substrates. The surface of the substrates is still wet with solution. The solution is transferred to the TEM grid and dried. Only crystals have good contact with the graphene are stable under the electron beam radiation. If the contact is bad, crystals are easily damaged even at liquid-nitrogen temperature (77K), but the stable crystals are good to image at room temperature even with the dose of 10^5 electrons/ \AA^2 .

3.3. EDX

Energy dispersive X-ray spectroscopy (EDX) measures X-ray emission when a sample is exposed to an electron beam. Since the emission is dependent on the atomic energy level, we can check the elemental distribution of a sample. SEM and EDX elemental mapping images are shown in Figure 3-4. The crystal has a uniform distribution of nickel and carbon. Since a

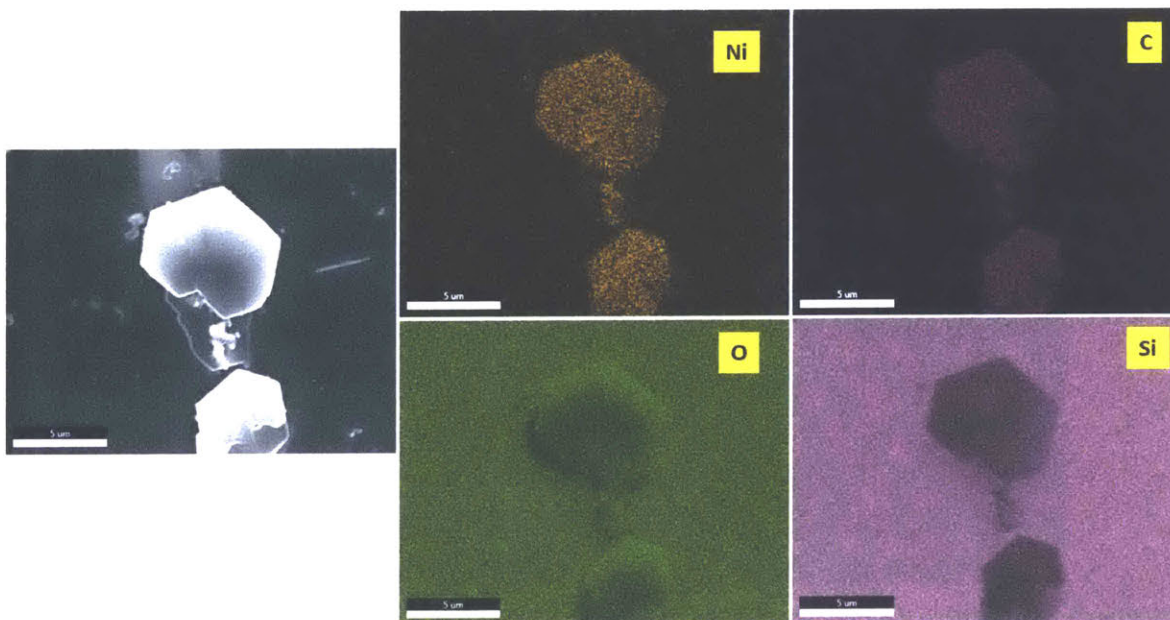


Figure 3-4 SEM image of crystals (left) and elemental distribution of nickel, carbon, oxygen and silicon measured by EDS.

silicon/silicon dioxide substrate is used, there is a strong background signal of oxygen and silicon. Given the contrast in the oxygen and silicon channels between the background and the crystals, the crystal is also likely to have oxygen as well.

From comparing the X-ray radiation intensity, we can quantify the elemental ratio. The EDX spectrum is shown in Figure 3-5. The crystal has both nickel and carbon peaks which cannot be found in the background. The elemental ratio of nickel to carbon is 1:12 which matches to $\text{Ni}_3(\text{HHTP})_2$. Along with an accurate lattice structure and spacing from TEM image, we confirm that the crystals are $\text{Ni}_3(\text{HHTP})_2$.

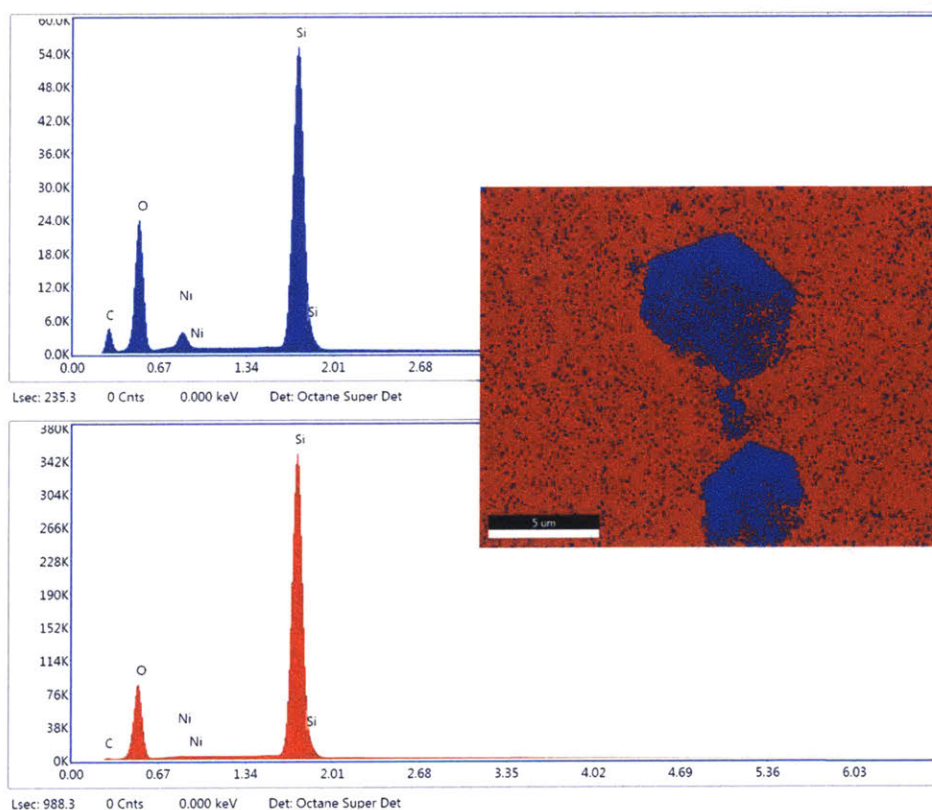


Figure 3-5 EDX phase mapping image and the corresponding energy dispersive spectrum. The crystal (blue phase) has clear carbon and nickel peaks whereas the background (red phase) has only silicon and oxygen peaks.

3.4. UV-Vis-IR spectrum

Infrared spectroscopy (IR) measures the vibronic nature of materials, which provide a fingerprint for materials. I checked the IR of single crystals by using a Bruker LUMOS model which combines IR and microscope. Therefore, I could check the IR of micrometer scale single crystals. The result is shown in Figure 3-6. The location of the vibronic peaks matches well with IR of powder samples. This confirms again that the single crystals are $\text{Ni}_3(\text{HHTP})_2$.

2D π MOFs are expected to have a narrow or zero gap due to their π -conjugated nature. Therefore, Ultraviolet-Visible-Near IR spectroscopy (UV-Vis-NIR) and IR can give information of the band gap. Unfortunately, it is hard to measure those with the micrometer-scale single

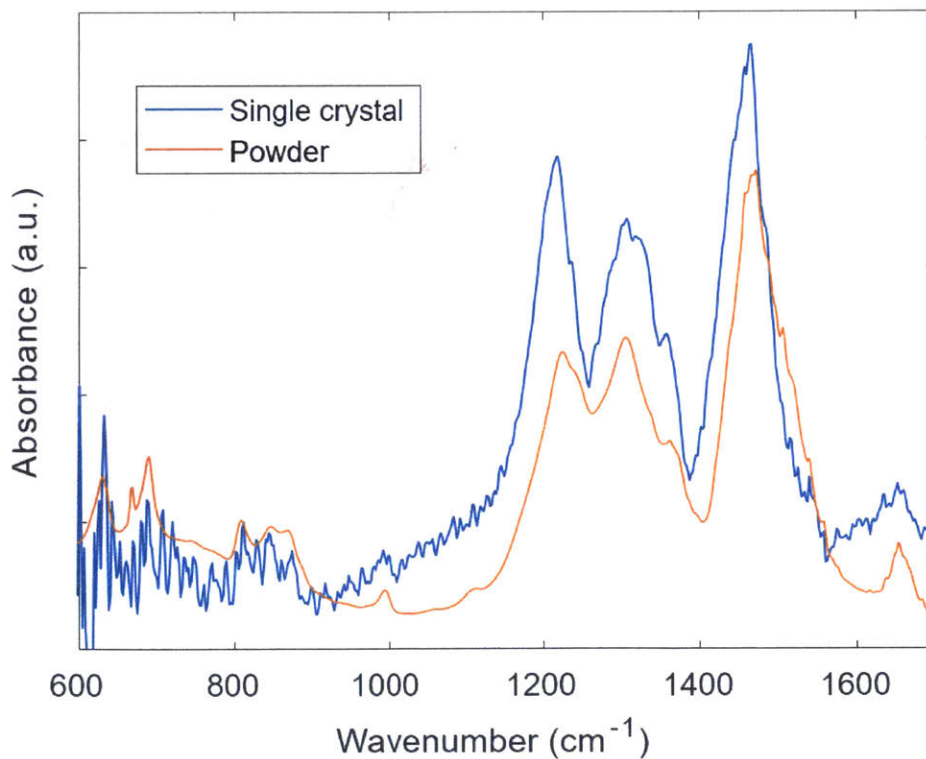


Figure 3-6 IR spectrum of HHTP single crystal (blue) and powder (red). The finger print region (Wavenumber below 1500 cm^{-1}) matches well with the powder IR. This is an additional proof that the single crystal is $\text{Ni}_3(\text{HHTP})_2$.

crystals. Instead, I determine the band gap based on the powder samples. I dilute the MOF powder into KBr by 1% and measure the diffuse reflectance for both IR and UV-vis-NIR. Then the reflectance is converted to Kubelka-Munk parameter which is proportional to the absorption coefficient over scattering coefficient⁶⁶. The result is shown in Figure 3-7 (a). To confirm the UV-vis-NIR, I also measure the transmission spectrum of the MOF. The transmission sample is prepared by dropcasting a MOF dispersed solution on a quartz substrate. To make the solution, I add methanol to the MOF powder and sonicate for one minute. The result is shown in the blue line of Figure 3-7 (a). The trend matches well to the drift reflectance measurement which validates the measurement.

To estimate the band-gap I used Tauc plot which is shown in Figure 3-7 (b)⁶⁷. I assume indirect band because the Tauc plot is linear for the indirect case whereas the plot is bendy for the direct band case. If the simple parabolic band assumption is applicable to this material, the Tauc plot indicates that it has indirect bands. Also, amorphous materials are often fitted with indirect band assumption even though their crystalline structure has a direct band gap⁶⁸⁻⁷⁰. Considering the small 2D domain size (<100nm) of Ni₃(HHTP)₂, it can be considered as amorphous phase, so it is reasonable to fit with an indirect band gap assumption. The optical band gap is determined as 0.18 eV. It is interesting to note that the band gap is much smaller than HOMO-LUMO gap of HHTP. It is measured to be 3.4 eV based on UV-Vis spectrum of evaporated HHTP film. Ni₃(HHTP)₂ has continuous absorption from 0.18 eV to 3.1 eV. This suggests the extension of π -conjugation in the MOF.

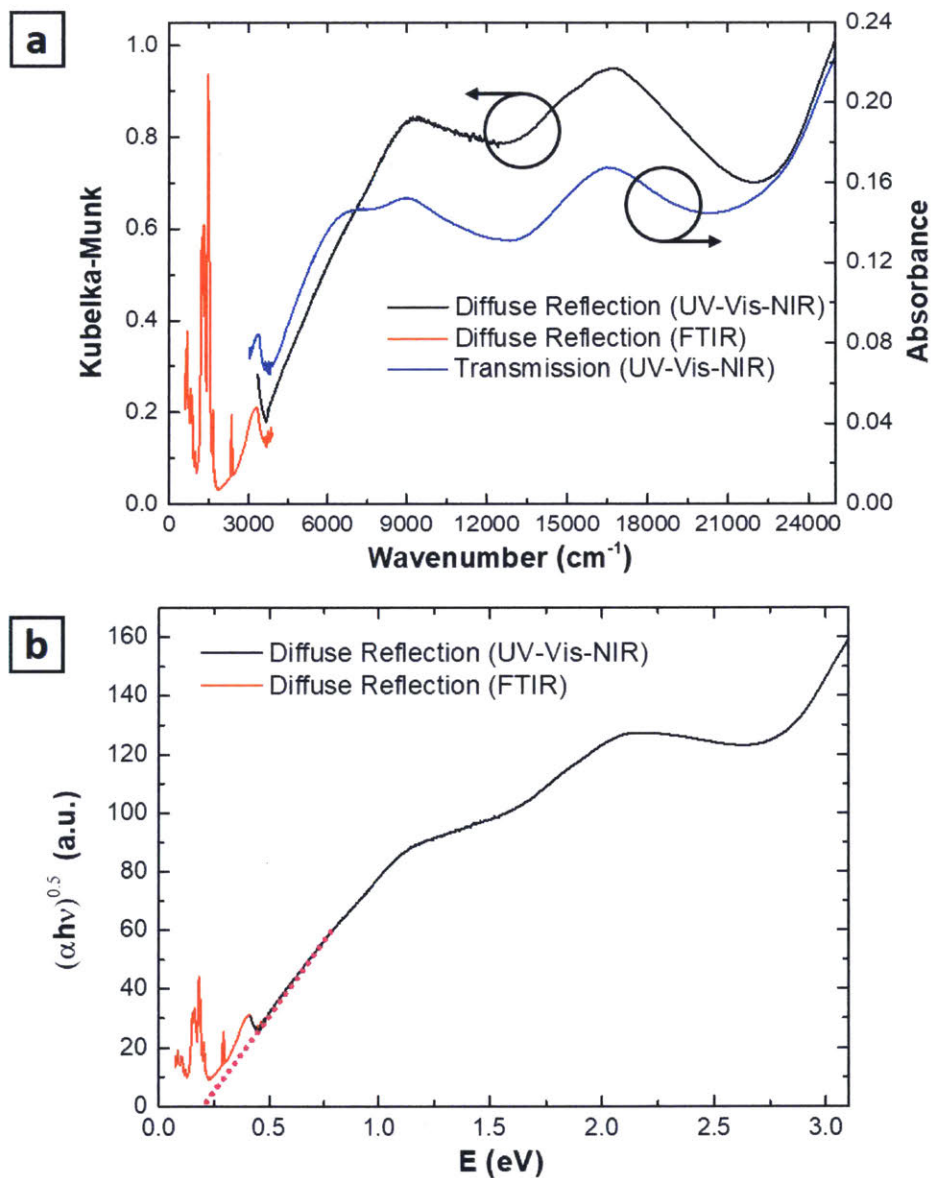


Figure 3-7 Band gap determination of $\text{Ni}_3(\text{HHTP})_2$ powder (a) IR and UV-vis-NIR spectrum of $\text{Ni}_3(\text{HHTP})_2$ powder by diffusive reflectance measurement (black and red) and transmission measurement (blue). (b) Tauc plot with an indirect band assumption. The band gap is determined from extrapolation of the linear band edge and it is 0.18 eV,

4. Device fabrication with $\text{Ni}_3(\text{HHTP})_2$ single crystal

To explore the electrical properties of the 2D π MOFs single crystals, the device fabrication is a crucial step as they are sensitive to the fabrication environment. MOFs generally have low hardness than inorganic materials⁶⁷. Therefore, they can experience plastic deformation or fracture at low stress. If they have defects in their crystals, it can be even easier to break them. In this chapter, I will describe three different fabrication methods, and potential damages from the fabrication technique.

4.1. E-beam lithography process

Electron beam (e-beam) lithography is a widely used technique to make nano-scale patterning. The device fabrication procedure is shown in Figure 4-1. It starts with spincoating of e-beam resist. PMMA (Poly methyl methacrylate) is the most common resist, and the manufacturer recommendation is to bake it at 180 °C for 60~ 90 seconds. This process can easily crack the crystals. The sample is heated up to 180 °C quickly which generates thermal stress. Also, if the thermal expansion coefficient of the MOF is different from that of PMMA, it will generate additional shear stress. In this case, bigger crystals will have stronger stress. Also, being at 180 °C itself can degrade the sample. The high temperature might cause a chemical reaction to deform the MOF.

Although some crystals survived the recommended baking condition, I could increase fabrication yield by modifying the baking step. First, I used a PMMA solution with chlorobenzene. Chlorobenzene has a lower boiling point of 132 °C than anisole (154 °C), so I could use lower annealing temperature. Also, annealing under vacuum helped to remove the solvent more efficiently. Thus I could lower the annealing temperature. In addition, the

degradation from the air, especially oxygen, can be alleviated. To reduce the thermal stress further, I changed the temperature slowly. The optimized baking condition was annealing at 100 °C for 10mins and rise time of 10 mins. Then it cooled down naturally. The vacuum level was 37 mTorr.

Electron beam exposure can also damage the sample. Using a thinner PMMA reduces the required e-beam dosage, but the problem cannot be fully solved without changing the whole fabrication process. Also, too small e-beam dosage can leave residual PMMA, so the metal contact can be bad. The bad contact forbids a transport measurement, so electron beam exposure needs to be well optimized to avoid the problems.

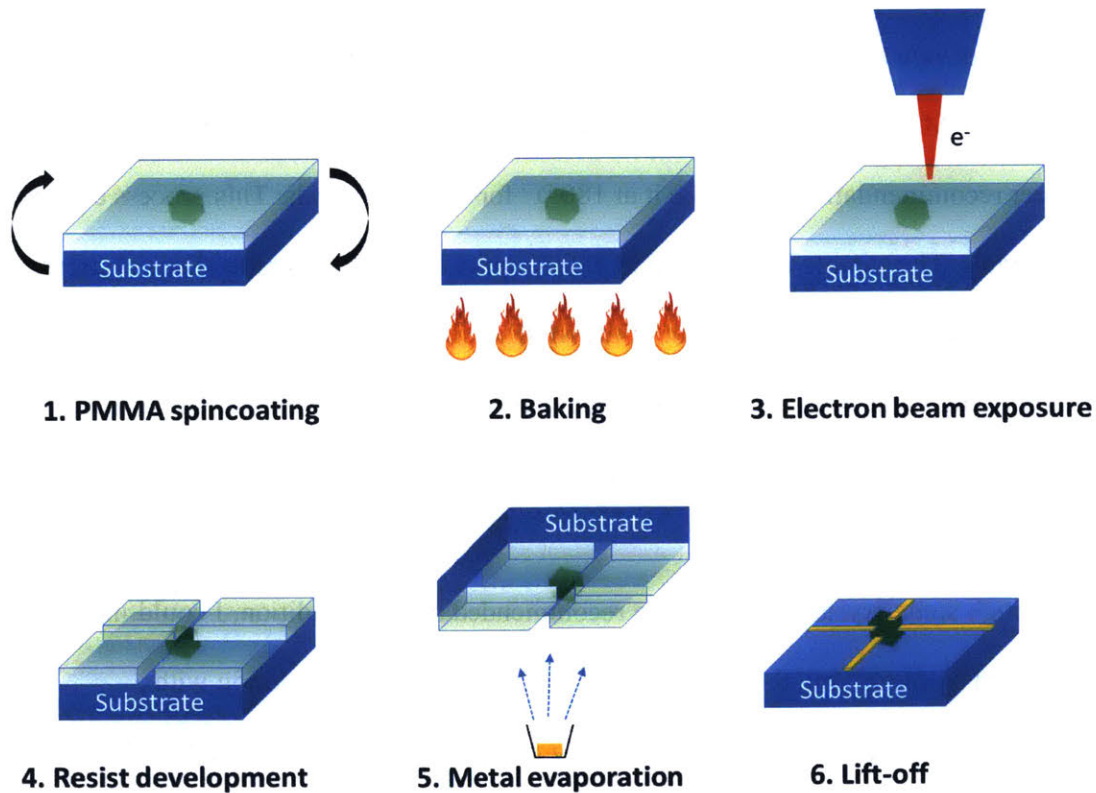


Figure 4-1 Device fabrication with e-beam lithography. The baking step, electron beam exposure, and metal evaporation process can potentially damage the crystals. Also residual PMMA can lead to a bad contact which is detrimental to the Hall measurement.

Metal evaporation can damage the crystal as well. If the distance from the metal source to crystal is too close, the crystal will heat up which cause thermal stress. If e-beam evaporator is used, it can also have e-beam damage as well. Therefore, it is good to use a metal evaporator with a large source to substrate distance and substrate cooling feature. Lastly, lift-off with warm solution should be avoided. I have not directly observed damage from the lift-off, but it is definitely safer to reduce the risk of crystal degradation.

The detail fabrication method is as follow. PMMA 950k C7 (from microchem) is spincoated at 4000 rpm resulting $\sim 1 \mu\text{m}$ thick film. The substrate is baked at $180 \text{ }^\circ\text{C}$ for 1 minute. An Elionix ELS-F125 is used for e-beam lithography. The acceleration voltage, current, and dose are 125 kV, 1 nA, and 2000 C/cm^2 respectively. When I use the mild baking condition, electron beam dose is optimized before the sample exposure. It typically has a higher dose. After the exposure, it is developed in MIBK:IPA=1:3 solvent for 60 seconds and washed in IPA for 30 seconds. Ti/Au or Cr/Au electrodes are deposited by vacuum thermal evaporation under $\sim 1 \times 10^{-6}$ torr. The substrate is water-cooled during the evaporation and the deposition thickness is 300 to 400 nm.

Figure 4-2 shows an example of crystal fracture after the e-beam lithography fabrication process. Generally, smaller crystals are more resilient to the fabrication process. They have fewer defects than bigger crystals and also the thermal stress caused by the different thermal expansion coefficient is smaller for the small crystals.

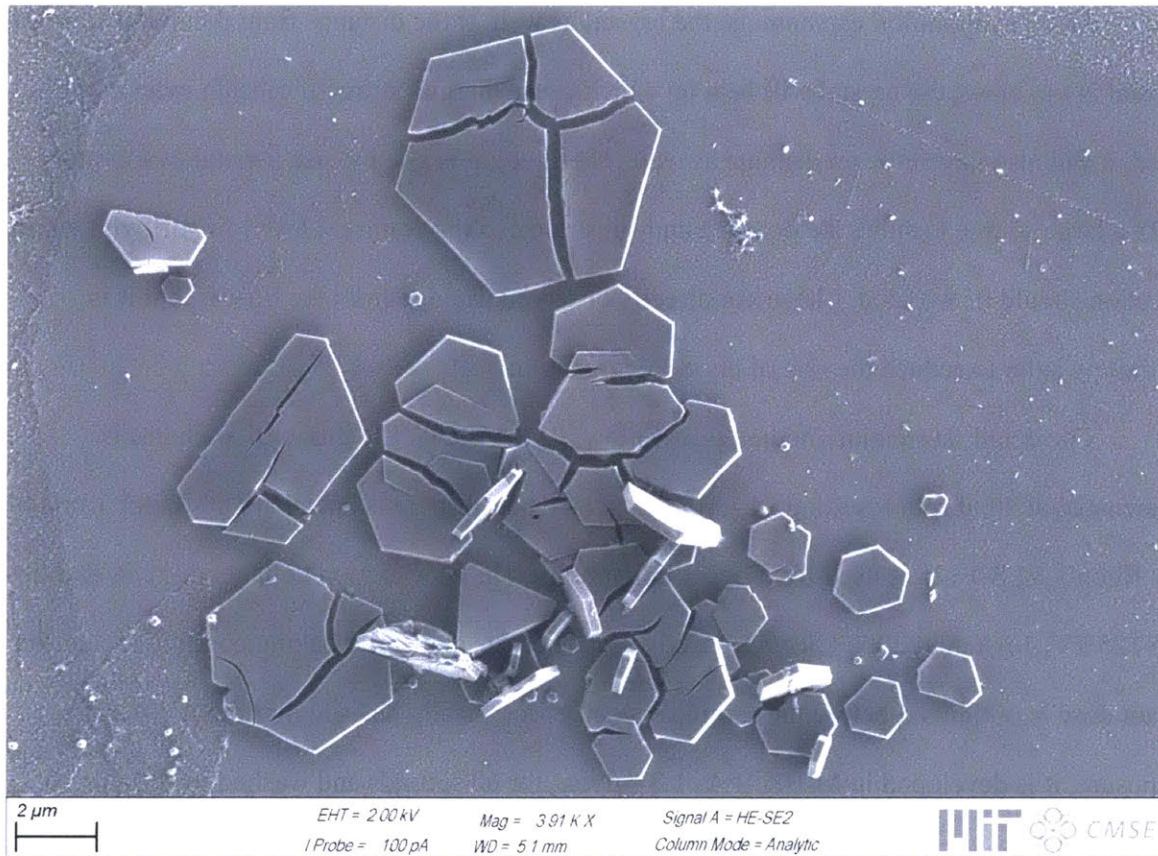


Figure 4-2 An example image of single crystal fracture after device fabrication with the electron-beam lithography technique.

4.2. Stencil-mask process

Stencil mask technique does not require PMMA spincoating, baking and e-beam exposure process. Therefore, the fabrication yield is much higher in terms of crystal fracture. However, placement of the mask with sub-micrometer accuracy is a challenging step which reduces the fabrication yield. Regardless of the difficulty in fabrication, this is the best technique to get a high-quality sample. The process is illustrated in Figure 4-3.

The process starts with the fabrication of the stencil masks. The mask is based on a Si/Si₃N₄ (200nm) substrate. Multiple windows of 850 μm × 850 μm are patterned with a photolithography technique. For big pattern, 1200 μm × 1200 μm are used. Then silicon is etched to make a silicon nitride window. On the window, we use photolithography or e-beam lithography to make the desired pattern of resist. Then, the silicon nitride is etched with reactive ion etcher. Once the mask is ready, a small amount of grease is applied near the edge of the mask. Then the mask is placed on a desired location by micropositioner. It is very important to press the mask well to minimize the gap between the mask and the crystal. If the gap is too large, it will generate shadow deposition around the pattern which can short the device. After the mask is well-positioned, the device fabrication is finished with metal evaporation. Due to the stability of the Si₃N₄ stencil mask, all patterns cannot be made in one mask. So two masks with fine and big pattern are used, and the above process is performed two times to make the devices.

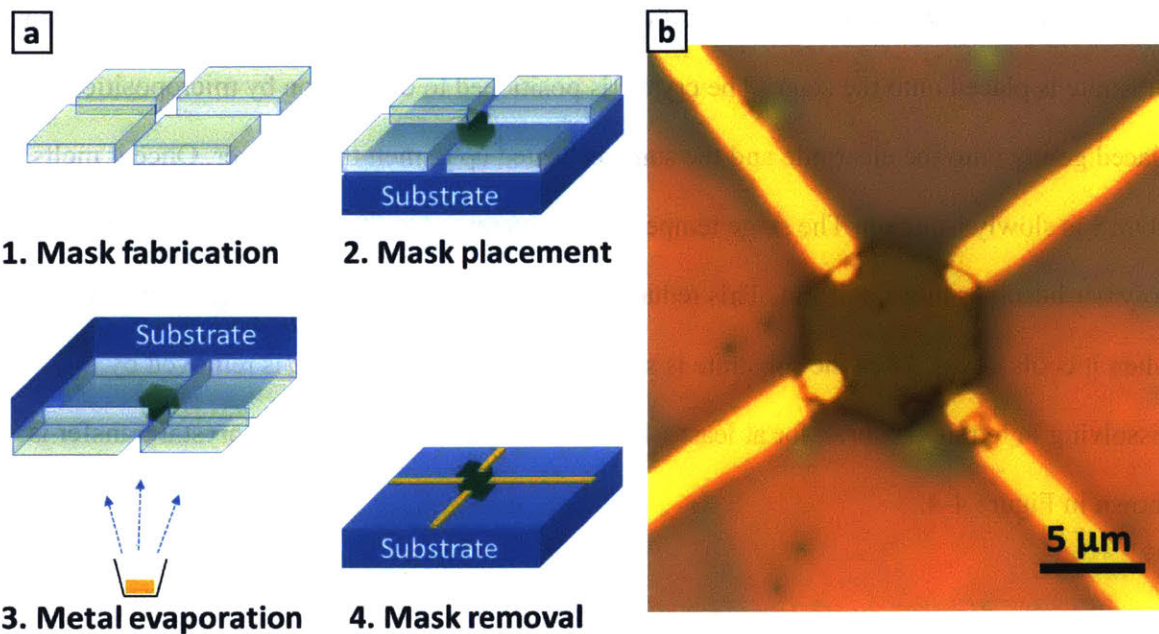


Figure 4-3 (a) Schematic illustration of device fabrication with the stencil-mask process (b) Optical microscope image of a device fabricated with the stencil mask process

4.3. Crystal transfer process

The previous methods generate top-contact samples. To make a bottom contact device with the MOF, transferring the crystal to a designated location is needed. We can successfully transfer the crystals with the following procedure.

A small piece (a few mm size) of PDMS (Polydimethylsiloxane) is placed on a microscope slide. PCL (Polycaprolactone; a melting point of 60 °C) is spincoated on top of PDMS at 2000rpm and baked at 70 °C for 15 minutes to make it smooth. A transfer stage is heated to 45 °C and a substrate contains the MOF crystals is placed on the stage. The microscope slide is loaded onto a micropositioner and approached to the crystals. When PCL is close to the substrate the temperature is slowly increased until it melts ($T_m \sim 60$ °C). As temperature increases, PCL contacts the crystals due to the thermal expansion. Once it has good contact, the heat is turned off and polymer is slowly cooled down. Then the polymer is lifted as it shrinks and the crystal is separated from the substrate and attached to the polymer. An electrode substrate is placed onto the stage. The crystal is positioned to destination by micropositioner. It is placed gently onto the electrode and the stage is heated up to melt the polymer. Once it melts, the PDMS is slowly lifted up. The stage temperature is increased to 70 °C so that the residual polymer becomes more uniform. This reduces the chance of irregular shrinkage of the polymer when it cools down. Then the substrate is slowly cooled down, and PCL is removed by dissolving in tetrahydrofuran for at least 1 hr. An example of the successful crystal transfer is shown in Figure 4-4.

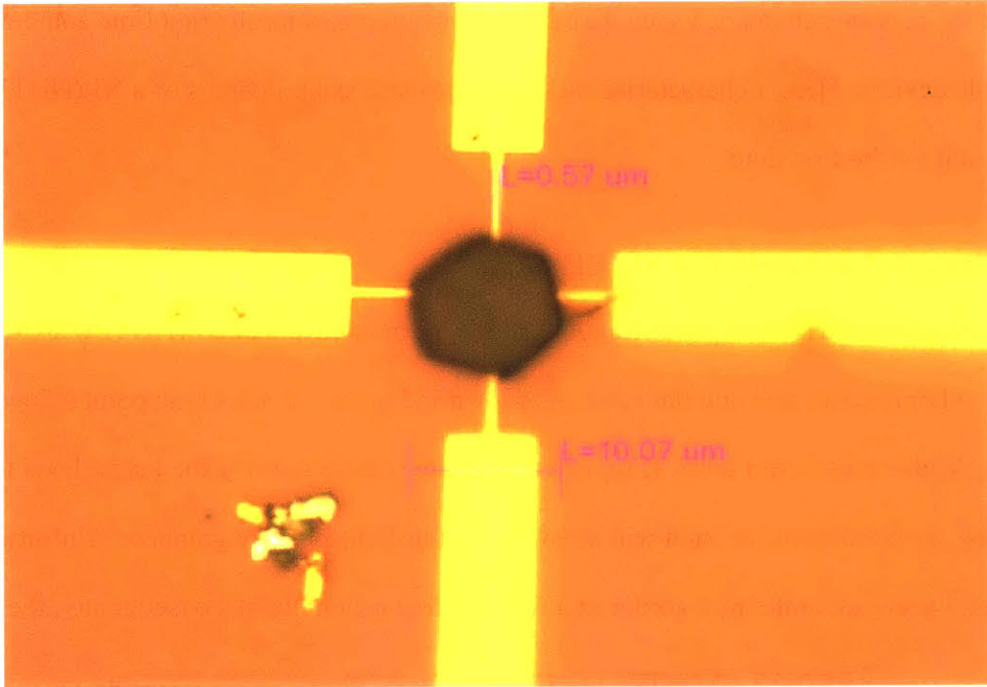


Figure 4-4 Bottom contact device fabricated with crystal transfer to a pre-patterned substrate.

5. Electrical properties of the $\text{Ni}_3(\text{HHTP})_2$ single crystal

In the previous chapters, I grew large single crystal plates for the first time and described how I made devices. Here, I characterize the 2D-plane electrical properties of a $\text{Ni}_3(\text{HHTP})_2$ single crystal for the first time.

5.1. Expected properties of $\text{Ni}_3(\text{HHTP})_2$

$\text{Ni}_3(\text{HHTP})_2$ has a hexagonal-Kagome lattice, so monolayers of $\text{Ni}_3(\text{HHTP})_2$ are expected to have two Dirac cones and one flat band. As shown in Figure 5-1, the Dirac point is located about 0.3 eV above its Fermi level. If we can apply gate voltage to bring the Fermi level to the Dirac point, the nondispersive band will show interesting behavior like graphene. Unfortunately, the crystals I grew are quite thick (order of a few hundred nanometers), consequently, the energy

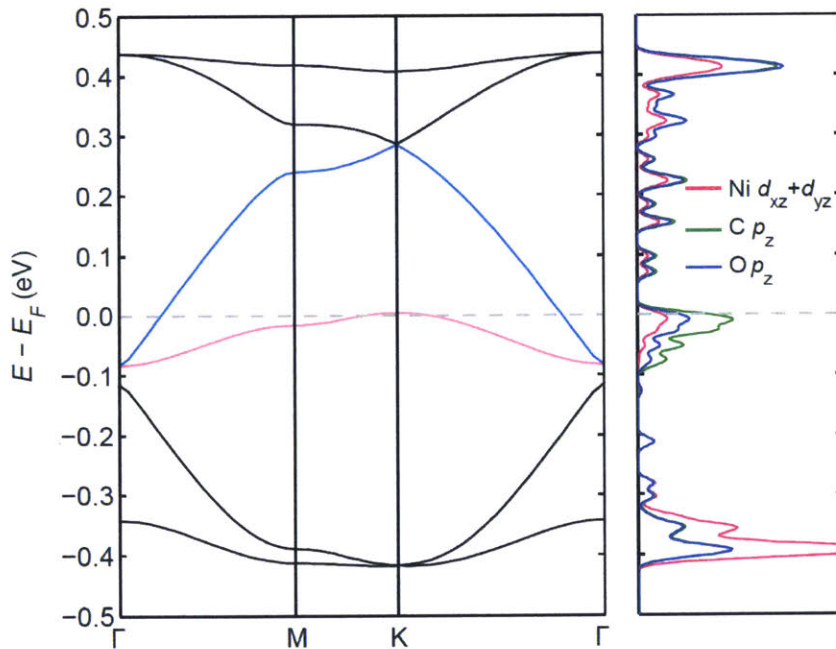


Figure 5-1 DFT-calculated band structure of monolayer $\text{Ni}_3(\text{HHTP})_2$. It is expected to be metallic in monolayer form. The Dirac point is located about 0.3 eV above the Fermi level. This calculation is done by Wenbin Li from Ju Li group at MIT.

band diagram is expected to deviate from the monolayer one. I do not have a single crystal XRD due to a small size of crystals, so the stacking order of $\text{Ni}_3(\text{HHTP})_2$ is unknown. If we assume AA stacking, the band structure is calculated as shown in Figure 5-2. It still shows the metallic behavior. Unlike the AA-stacking based calculation, the optical band gap of the crystals is

measured as 0.18 eV with UV-Vis-NIR and IR, so it is expected to show semiconducting behavior.

Since the Brillouin zone of the MOF is small (i.e. it has large unit cell), the interaction between the unit cell is weak which leads to small dispersion of band. The narrow bandwidth can lead to small curvature which means the large effective mass. Also, the density of states will be

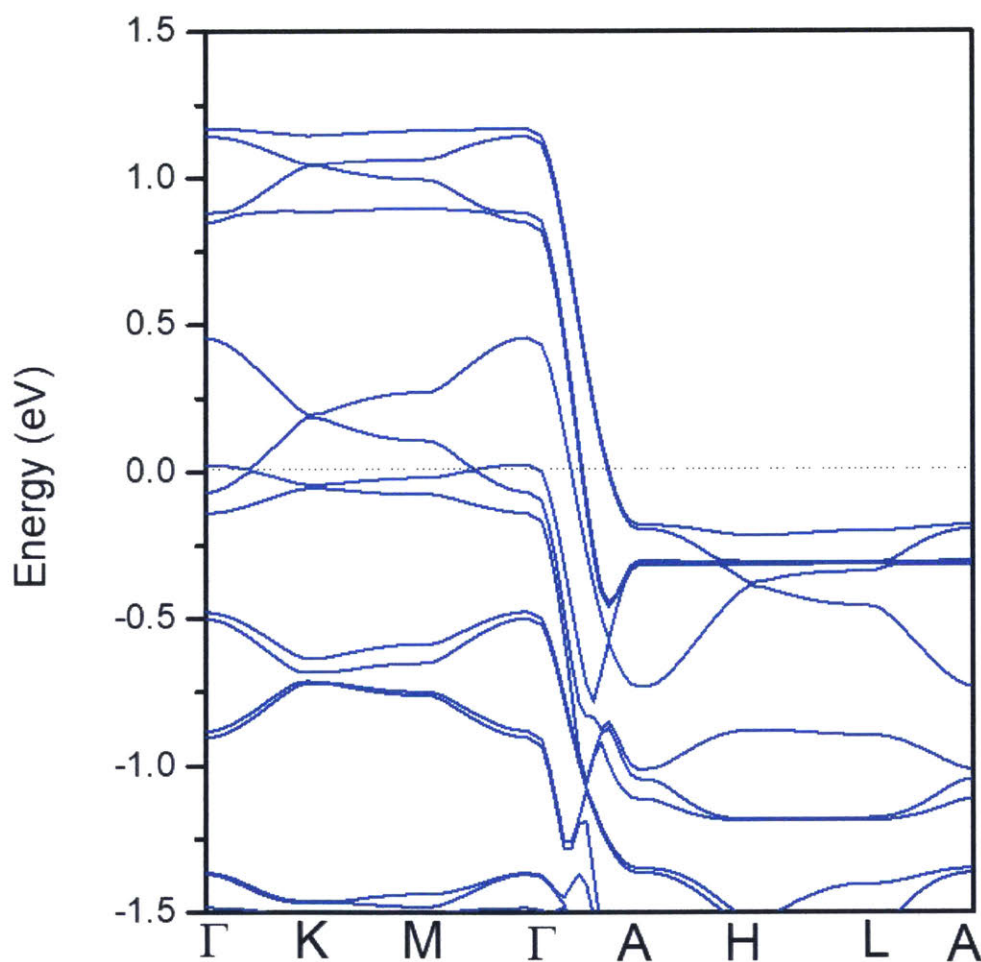


Figure 5-2 DFT calculated band structure of bulk $Ni_3(HHTP)_2$ with an assumption of AA stacking. Note that the x-axis is not proportional to the amplitude of the k vector. Γ to A distance is much larger than others. This calculation is done by Jian Zhou from Ju Li group at MIT.

high due to the narrow band. Therefore, the carrier mobility is expected to be small. If there is a Dirac point in a MOF and the Fermi level is located near the point, the band curvature can approach zero which can exhibit relativistic behavior like graphene⁷¹. In that case, the mobility might be high in spite of the narrow band.

5.2. Electrical conductivity

5.2.1. Measurement of highly resistive materials

Semiconductors have very low conductivity at low temperature if the sample is intrinsic. Transport measurements with highly resistive materials are prone to errors, so I want to quickly point out common mistakes.

If the resistance of a sample is over 1 G Ω , the triaxial cable must be used. The dielectric material within BNC cables has a resistance in the G Ω range. If a BNC cable is used for the measurement, the measured properties are the dielectric of the BNC cable, not the sample.

The impedance of the voltmeter is also important. If the voltmeter impedance is too low and comparable to the sample resistance, a significant amount of current will flow through the voltmeter, not through the sample. Therefore, it is important to check that the impedance of the voltmeter is sufficiently higher than sample resistance. The sample resistance includes the contact resistance, so it would be ideal if the impedance of the voltmeter is at least 100 times the sample and contact resistance.

In this work, I used an Agilent 4156c semiconductor parameter analyzer or combination of a Keithley 2400 sourcemeter and an Agilent 34401a multimeter with 10 G Ω input impedance. The temperature dependence was measured with a LN₂-cooled cryo-probe station (Janis) or liquid He dewar mount insert (Cryo industries of America).

5.2.2. Fabrication methods and conductivities

Figure 5-3 summarizes the electrical conductivity of the samples with different size and different fabrication methods. Before I explain the data, please note that all stencil mask samples are measured under vacuum whereas others are measured in ambient environment. The unique property of the MOF is its sensitive to pressure. Although the detailed mechanism is not yet

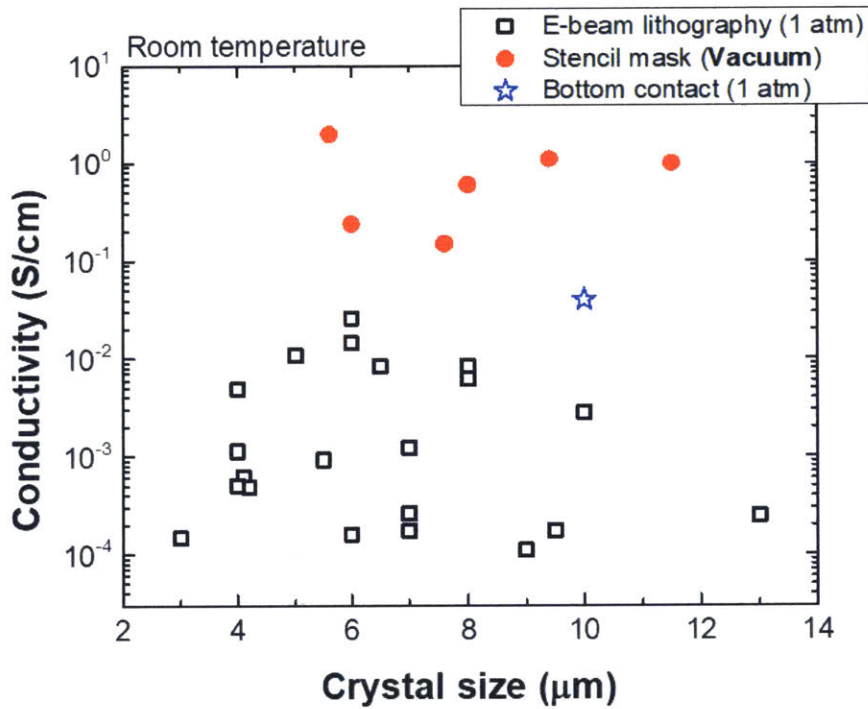


Figure 5-3 Electrical conductivities as a function of the various crystal size and the three fabrication methods. Note that the electrical conductivity increases by one order of magnitude under vacuum. All the devices fabricated with the stencil mask technique were measured under vacuum and others are measured in ambient environment.

known, it typically has almost one order of magnitude higher conductivity under vacuum.

Therefore, one must consider an additional order of magnitude increase to compare between stencil mask samples and others. Also, this is an additional evidence that the crystals are indeed MOFs.

The conductivity of 21 e-beam lithography devices spreads over more than two orders of magnitude. This is probably related to the crystal damage from the fabrication process. Also, smaller crystals tend to have better performance. This is because the smaller samples are more resilient from the damage for the reasons discussed in the previous chapter. Although many samples showed low conductivity, the best conductivity of the e-beam lithography samples is similar to the samples made with the stencil mask. If the e-beam lithography process is further optimized, it might be able to increase the fabrication yield of high-quality devices.

The bottom contact sample showed similar conductivity to the stencil mask samples. Compared to the stencil mask technique, bottom contacts have well-defined electrode patterns. So the accuracy of the measurement should be better than other technique. It is reassuring that the bottom contact devices have similar conductivity. Unfortunately, the contact became very unstable upon evacuation. Generally, organic materials do not form good contacts with bottom gold electrodes, graphene contact is desired to have better performance ⁷².

The conductivity of the stencil mask samples deviates over one order of magnitude and showed the best conductivity of 2 S/cm. As discussed in the previous chapter, this method minimizes the damage to crystals and results in high performance.

5.2.3. Anisotropic nature

The two-dimensional structure gives the anisotropic nature. The conductivity is also expected to be different as in-plane conduction is through the π conjugated bonds whereas the out-of-plane conduction is through the van der Waals bonding. Indeed, the out-of-plane conductivity of $\text{Ni}_3(\text{HHTP})_2$ is measured as 1×10^{-4} S/cm which is four orders of magnitude lower than the in-plane conductivity. Note that the c-direction conductivity is based on a two-probe

measurement due to the small size of a single crystal wire. Although the contact resistance is included in the conductivity, the four orders of magnitude difference show the anisotropic nature of $\text{Ni}_3(\text{HHTP})_2$.

5.2.4. Temperature dependence

A temperature dependence of the electrical conductivity is required to verify semiconducting behavior. As shown in Figure 5-4, the temperature dependence shows clean mono-exponential character and the activation energy is 0.09 eV. It is exactly half of the band gap. The carrier density is expected to have an activation energy of 0.09 eV if the crystal is an intrinsic semiconductor. If it is an extrinsic semiconductor, the mobility should be responsible for the conductivity change. We will discuss this further in the following section together with the Hall measurement.

The temperature dependence is measured by sweeping current-voltage (I-V) characteristics at each temperature. As shown in Figure 5-5, it shows ohmic behavior as I-V is linear for the plotted temperature region.

A pressed pellet device was fabricated from powder to provide comparison with the conventional method used to characterize electrical properties. The pellet was made by pressing the powder with 6.6 ton-force/cm². The conductivity was 3.6×10^{-3} S/cm at room temperature which is similar to previous reports^{47,73}. The low conductivity can be explained by grain boundaries. Also, the low out-of-plane conductivity might contribute to the low conductivity.

The pressed pellet has higher activation energy near room temperature. This also can be explained by the grain boundaries and out-of-plane conduction. Unlike the single-crystal, it does not have mono-exponential temperature dependence. There can be many possible explanations

for this behavior due to the complexity of the system so we do not know the exact mechanism without additional experiments.

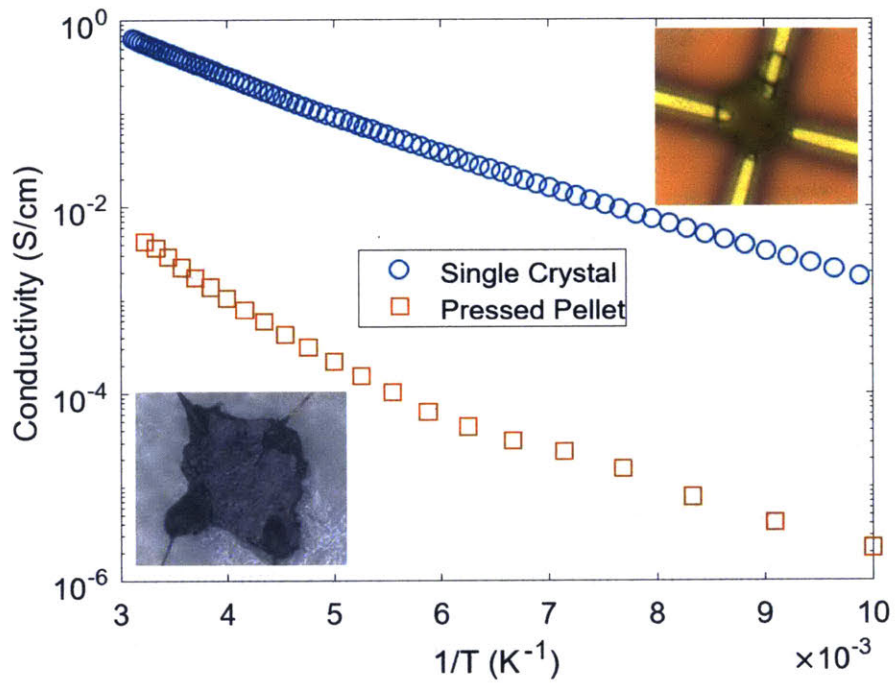


Figure 5-4 Temperature dependence of conductivity for the single crystal and pressed pellet sample. The single crystal shows clean mono-exponential dependence with an activation energy of 0.1 eV.

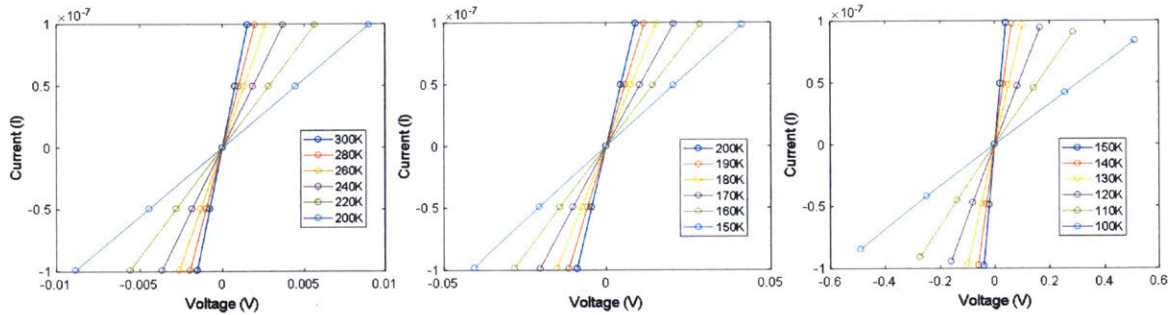


Figure 5-5 current-voltage curves from 300K to 100K. All of them show Ohmic behavior.

5.3. Hall measurement

5.3.1. Challenges in Hall measurement

A Hall measurement gives the carrier density of the system and type of major carrier. Together with the conductivity, we can estimate mobility which is crucial information to understand the transport properties of materials. The Hall measurement, however, is often challenging.

A material should have a low carrier density with high mobility to get a clear Hall signal. The Hall voltage is inversely proportional to the carrier density, so having low conductivity is helpful to increase the Hall signal. In reality, however, we always measure a resistive voltage drop together with Hall voltage as the Hall electrodes are not completely perpendicular to the current flow direction. The resistive voltage drop is large if a material has low conductivity. If the noise level of the resistive voltage drop is comparable to the Hall voltage, the Hall signal will be buried in the noise. Therefore, an ideal material for the Hall measurement has low carrier density with high mobility.

If a material does not have high mobility, it is important to minimize the noise level of the resistive voltage drop. For that, the electrode contact should be optimized. Unstable contacts generate a high noise level, so the Hall signal cannot be measured.

Also having a symmetric and small contact area is important. If the electrodes are symmetric, the resistive voltage drop can be minimized. Even if the electrodes are symmetric, large contact area could cause a problem. If the metal contact is not good, the effective contact position could be one corner of the electrodes. The large electrodes make the actual electrodes asymmetric and this leads to the high resistive voltage drop.

5.3.2. Carrier density and mobility of $\text{Ni}_3(\text{HHTP})_2$

A Hall measurement result is shown in Figure 5-6. The data is noisy because the contact was not good, and $\text{Ni}_3(\text{HHTP})_2$ has high carrier density with low mobility. The Hall resistance was measured from the slope of the I-V (Hall voltage) sweep. We swept the magnetic field back and forth 10 times from 1 to -1 T. Each data point in the graph was average of 10 sweep and the error bar represents the standard error about the mean.

The Hall coefficient was $-0.46 \pm 0.14 \text{ cm}^3/\text{C}$. If the crystal is an extrinsic semiconductor or the electron mobility is much higher than the hole mobility, the carrier density is estimated as $1.4 \times 10^{19} \text{ cm}^{-3}$ and the electron mobility is $0.16 \text{ cm}^2/\text{V}\cdot\text{sec}$. Thus, the origin of the high conductivity of $\text{Ni}_3(\text{HHTP})_2$ is its high carrier concentration rather than fast carrier transport. Due to the unstable contact and properties of the $\text{Ni}_3(\text{HHTP})_2$, a Hall measurement at a lower temperature failed.

Although the origin of the high carrier density is not identified, a simple parabolic band assumption suggests that the intrinsic carrier density is a similar order of magnitude to the

measured value. The electron carrier density of 3D non-degenerate semiconductors with the parabolic band assumption is ⁷⁴,

$$n = 2 \left(\frac{m^* k_B T}{2\pi \hbar^2} \right)^{3/2} e^{-(E_C - E_F)/k_B T}$$

Where m^* is effective mass, k_B is Boltzmann constant, T is temperature, \hbar is Planck constant, E_C is conduction band level, E_F is Fermi level. If a semiconductor is intrinsic, $E_C - E_F$ is half of the band gap. If we put an effective mass of $1 m_e$ (static electron mass) to $6 m_e$ the carrier density is ranging from 1×10^{18} to $1 \times 10^{19} \text{ cm}^{-3}$. Since triphenylene-based MOFs have large unitcells (lattice parameter of $\sim 2 \text{ nm}$), the Brillouin zone is small and it leads to narrow bands. The narrow bands have small curvature so have high effective mass. The in-plane effective mass

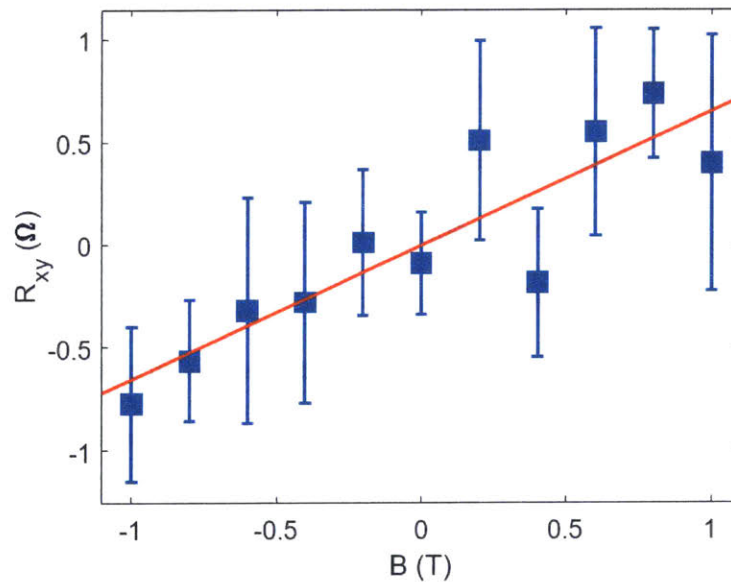


Figure 5-6 Hall measurement at room temperature. The Hall coefficient was $-0.46 \pm 0.14 \text{ cm}^3/\text{C}$. If the crystal is an extrinsic semiconductor or electron mobility is much higher than hole mobility, the carrier density is estimated as $1.4 \times 10^{19} \text{ cm}^{-3}$ and the electron mobility is $0.16 \text{ cm}^2/\text{V}\cdot\text{sec}$.

of $\text{Co}_3(\text{HHTP})_2$ was calculated to be 1.27 to $18.7 m_e$ ²¹. Therefore, the measured carrier density of $1 \times 10^{19} \text{ cm}^{-3}$ can be intrinsic carriers due to the small band gap of $\text{Ni}_3(\text{HHTP})_2$. Certainly, this does not rule out the chance of being extrinsic, and further experimental verification is required.

If the majority of carriers are intrinsic (i.e. thermally excited from the valence band), the estimated carrier density and the mobility is over- and underestimated, respectively because the electrons and holes cancel out the Hall signal. But materials like graphite has only a 10% difference between the mobility of electrons and holes⁷⁵ which can lead to 20 times underestimation. Also the big electrode size in comparison to the crystal size can lead to underestimation of the mobility. For the big electrodes, current can flow to Hall electrodes which reduces the Hall coefficient⁷⁶.

The reason for the low mobility might be the narrow bands of the MOF. As discussed in the previous section, MOFs have narrow bands because of the large unit cell. The narrow bands result in a high effective mass and high density of states. Therefore, the high mass and the fast scattering time lead to low mobility.

Even though the mobility was low, growth of single crystals enables the Hall measurement. Assuming the polycrystalline samples have the same carrier density, the mobility would be two orders of magnitude lower. Therefore, the Hall measurement is nearly impossible with the polycrystalline sample, so we cannot get the carrier density or mobility information from the sample.

5.4. Comparison with other materials

It is interesting to compare the MOF properties with other materials. In Figure 5-7, mobility-carrier density-electrical conductivity data of materials are shown. Metals have high carrier density limited by their atomic density⁶⁰. Silicon has very low ($\sim 10^{10} \text{ cm}^{-3}$) intrinsic carrier density, but it can be increased by more than 10 orders of magnitude. The mobility

decrease at high doping concentration (above 10^{17} cm^{-3})⁶². Polysilicon has about 2 orders of magnitude lower mobility due to the grain boundaries⁶³. The most conductive organic conductor, PEDOT:PSS generally has a conductivity of 100 S/cm, but increasing the crystallinity can lead to almost 10^4 S/cm ⁶⁴. The mobility is on the order of $10 \text{ cm}^2/\text{Vs}$. $\text{Ni}_3(\text{HHTP})_2$ data is marked as a yellow star in the figure. Due to the potential underestimation of mobility, it could move toward the bottom right. Compared to the atomic density of $\text{Ni}_3(\text{HHTP})_2$, the carrier density can be still increased by up to 1000 times more. In terms of mobility, it is pretty low compared to other materials. It would be interesting to check the mobility of a monolayer. If we can bring the Fermi level to the Dirac point, mobility can be increased dramatically.

Although the electrical properties are not amazing compared to other materials, this is the first measurement of in-plane single-crystal properties. There are other MOFs that are more conductive than $\text{Ni}_3(\text{HHTP})_2$. As we obtained much higher conductivity from the single crystal characterization, those highly conductive MOFs can show even better performance with single crystal devices. If we put more single crystal data points on the Figure 5-7, we can truly understand the structure –property relation of 2D π MOFs. Based on that understanding, we will be able to design and make better 2D π MOFs.

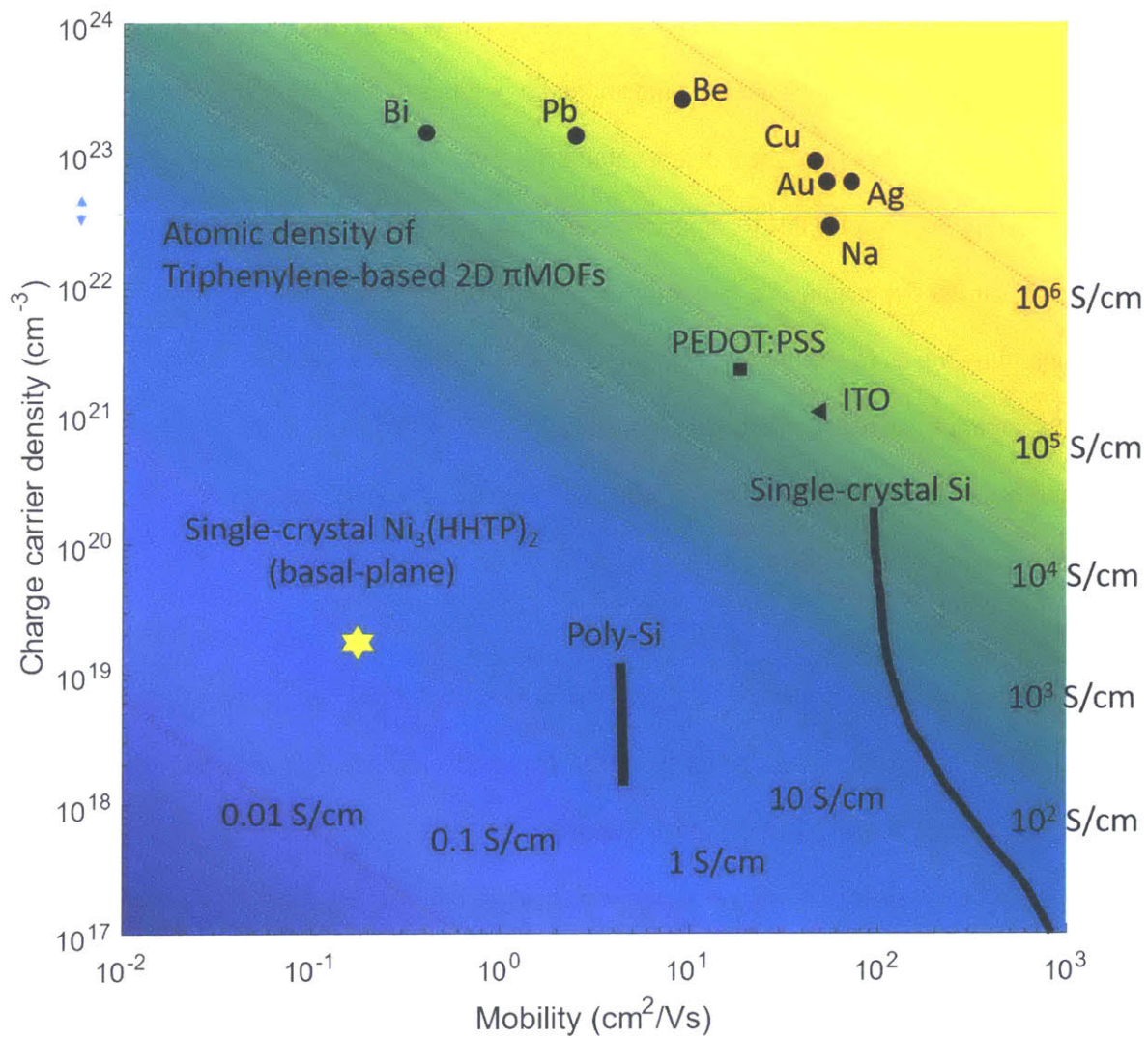


Figure 5-7 Mobility-carrier density-conductivity mapping of various materials. The color indicates the electrical conductivity in log scale. The dotted diagonal lines represent the order of magnitude of the conductivity.

6. Conclusion and outlook

In this thesis, I analyze the growth of 2D π MOFs. Based on that, I could develop a novel growth method generates micrometer-scale single crystal plates. This enables me to explore the in-plane electrical properties of the material for the first time. With the single crystal characterization, we could understand the fundamental properties of $\text{Ni}_2(\text{HHTP})_3$. Whereas the single crystals of Ni-CAT-1 generate a distinct Hall effect, we were unable to measure the Hall effect in pressed pellet samples due to suppression of the charge carrier mobility by grain boundaries. A similar dependence on morphology was observed in the measurements of overall conductivity, allowing us to confirm expectations that the single crystal sample exhibits significantly superior electronic properties overall.

I believe this is the beginning of the field. We only measured the conductivity and mobility of one particular 2D π MOF. Therefore, tremendous amount of works can be done in the near future.

First, we need to grow single crystal plates of other 2D π MOFs, and properly characterize their intrinsic properties. This will help us to understand the 2D π MOFs better and we can develop better 2D π MOFs based on the understanding.

Making a large single-crystal monolayer will also greatly help the field. The monolayer of the materials is expected to have exotic properties. Also, we can tune the Fermi level by applying external gate voltage. Furthermore, it can form heterostructure with other 2D materials. The tunability of the MOFs is great addition to the 2D materials field.

The heterostructure can be made with the current large single crystal as well. If we place the single crystals on top of graphene, interesting properties are expected. Since the graphene is more conductive than $\text{Ni}_3(\text{HHTP})_2$, the MOF crystal does not disturb the measurement of the

tuned graphene. The Kagome structure of the MOF will perturb the graphene, and it may cause interesting physics. Also, the metals can induce the spin-orbit coupling in the graphene. Recently tuning the graphene's properties lead to interesting physics including the magic-angle superconductivity⁸⁰. The tunable nature of the MOFs could potentially generate interesting physics and enrich the 2D materials field.

Increasing the quality of the crystal is also very important. Even though I measured single crystals, it would not perform well if the defects levels are high. From the device fabrications, I experienced the various fracture of the crystals and variations in the crystal quality. Thorough study on the growth parameters are needed to improve the quality and even better performance can be obtained.

Finding a way to form good electrode contact will open up many opportunities. The temperature dependence of Hall measurement was failed due to the high noise level. If we want to study effect of adsorption of various gases, the Hall measurement must be carried out to check how carrier density and mobility are changed upon the adsorption. For $\text{Ni}_3(\text{HHTP})_2$, the adsorption reduces the conductivity which would make the Hall measurement even more challenging. Also, we can explore the interaction with guest molecules and how the electrical doping affects the mobility. Again, the higher carrier concentration would make the Hall measurement more challenging, so the contact problem should be solved.

Lastly, device application is also very important. Thin single crystal plates can have better transistor performance than polycrystalline film. For the sensor application, the single crystal can maximize the response speed and sensitivity. A wide-gap 2D MOF can be used for solar cell device structure or light-emitting diode applications. If the discussed exotic properties are measured, they will open up new applications.

The 2D π MOFs have great potential based on the extreme tunability, and the field is in its infancy. I hope this thesis facilitate the 2D π MOFs research and we can demonstrate the great potential together.

7. Special chapter

The major focus of this thesis is on 2D π MOFs, but I also spent a significant amount of time to explore the properties of organic materials for electrical and optical applications. In this chapter, two topics will be discussed. The first is on the charge transport in organic films composed of a mixture of small molecules. In particular, I found a link between two popular equations that explain percolative transport in a mixture of small molecules. The second is on the degradation of organic light-emitting diodes (OLEDs). OLEDs are dominant display technology in mobile display and increasing their occupancy in TV markets. Eventually, they are targeting general solid-state lighting application. The only major problem is the degradation of organic materials which are known as burn-in phenomena. So far people have mainly focused on the iterative synthesis of variety of materials and tested it. There has been progress, but still, it is the bottleneck for many applications. Therefore, understanding the fundamental science behind the degradation is crucial to solve the problem. In this chapter, the dominance of the exciton lifetime on the photostability will be discussed.

7.1. Link between hopping models and percolation scaling laws

Mixed host compositions that combine charge transport materials with luminescent dyes offer superior control over exciton formation and charge transport in organic light emitting devices (OLEDs).⁸¹⁻⁸⁵ Broadly defined, a mixed host adds a material dedicated to charge transport into the conventional combination of a luminescent dye and a host material. As shown in Figure 7-1, the extra flexibility gained upon the addition of a third material allows tailoring of charge balance within the emissive layer, the generation of a broad exciton recombination zone⁸¹, and control over exciplex formation⁸³. Mixed hosts are especially important for high-efficiency blue OLEDs because it is difficult to synthesize high-conductivity bipolar hosts with blue or UV triplet exciton levels.⁸⁶ It is necessary to understand, however, the electrical properties of dilute charge transport materials within a host. Two prior studies have measured the charge carrier mobility of the electron transport materials Tris-(8-hydroxyquinoline)aluminum (AlQ₃) and bis(2-methyl-8-quinolinato)-4-phenylphenolate aluminum when mixed into N,N'-di(naphthalen-1-yl)-N,N'-diphenyl-benzidine^{87,88} It was observed that increasing the fraction of the conductive material leads to a higher mobility, but no clear relation between concentration and mobility was identified. Subsequently, it was observed that the electrical properties of 4,7-diphenyl-1,10-phenanthroline (BPhen)/ tetracyano-quinodimethane (TCNQ)⁸⁹ and AlQ₃/ 4,4'-bis(carbazol-9-yl)-biphenyl (CBP)⁹⁰ mixed layers could be explained with an empirical scaling law:

$$\sigma \propto (x - x_0)^t \quad (7.1)$$

where σ is conductivity, x is the fraction of the transport material in the host, x_0 is the percolation threshold, and t is the critical exponent.⁹¹ Although the physical meaning of x_0 and t

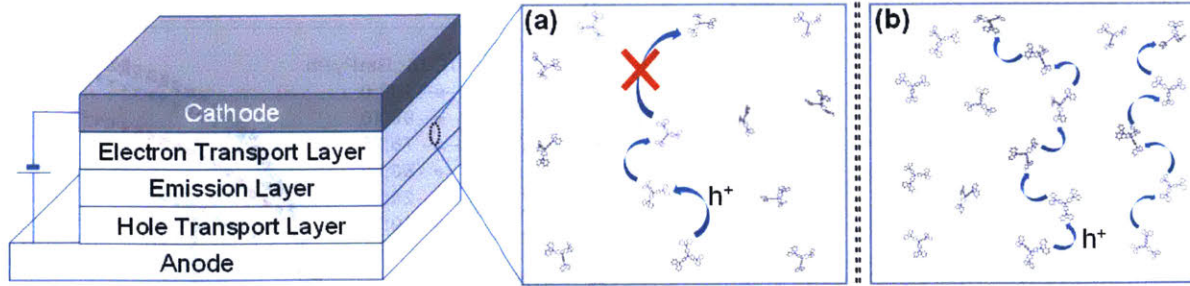


Figure 7-1 Schematic illustration of charge transport in mixtures of small molecules: (a) transport below percolation threshold (b) above percolation threshold. Charge moves along the conductive molecules. At high concentration of the molecules, a percolation path is formed and carriers transport with hopping transport.

is not clear, this model had been widely used to analyze charge transport in many polymer-mixture systems due to its universality and simplicity.⁹²⁻⁹⁷

An alternative model is based on the Miller-Abrahams (MA) model for hopping conductivity in a disordered solid:⁹⁸

$$\mu \propto R^2 \exp\left(-\frac{2R}{\alpha}\right) \quad (7.2)$$

where μ is mobility, R is the hopping distance, and α is the localization length of charge.

This model has been used to determine the localization length in polymers by measuring the concentration dependence of mobility.⁹⁹⁻¹⁰²

We demonstrate analytically that Eq. (7.1) provides a reasonable approximation for the MA model. An expression for the localization length as a function of percolation threshold and critical exponent in the range $x_0 < x \leq 1$ is obtained as follows:

$$t = \frac{\partial \log((x-x_0)^t)}{\partial \log(x)} \frac{x-x_0}{x} \approx \frac{\partial \log(\rho^{-2/3} x^{-2/3} \exp(-2\rho^{-1/3} x^{-1/3}/\alpha))}{\partial \log(x)} \frac{x-x_0}{x} = \left(\frac{2\rho^{-1/3}}{3\alpha} - \frac{2}{3} x^{-1/3} \right) (x^{-1/3} - x_0 x^{-4/3}) \quad (7.3)$$

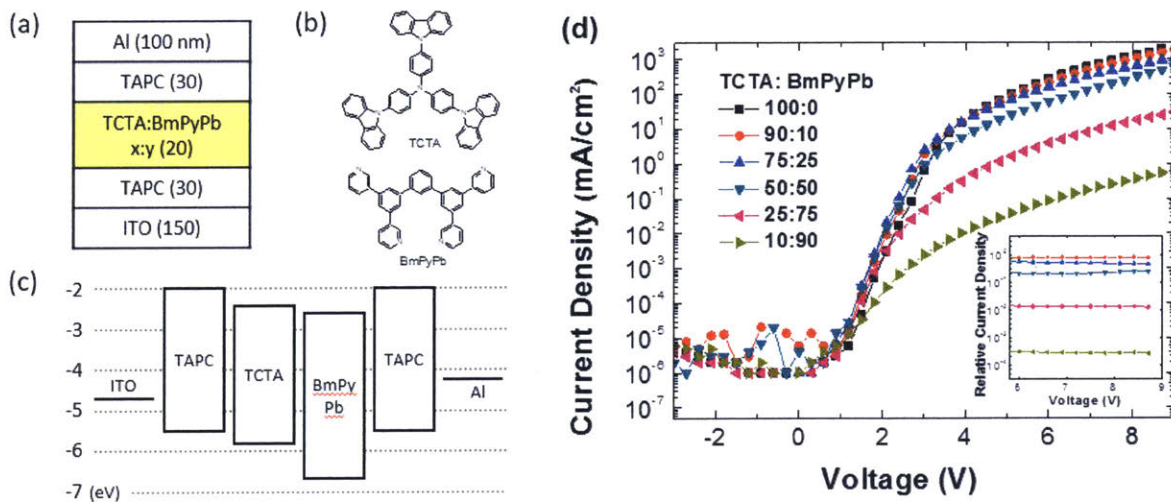


Figure 7-2 (a) Structure of the hole only devices. TAPC has high LUMO level which prevent injection of electrons. (b) Molecular structures of TCTA and BmPyPb. (c) Energy level configuration of the devices. The deep HOMO level of BmPyPb hinder the hole transport. (d) Current density- voltage characteristics of the hole only devices with different mixing ratio. Inset: Relative current density of the devices. It is normalized by the 100% TCTA hole-only device.

where the hopping distance R is $\rho^{-1/3}x^{-1/3}$ and ρ is the molecular density.¹⁰² Evaluating at $x = 1$ yields:

$$\alpha \approx \frac{2(1-x_0)}{3t+2(1-x_0)} \rho^{-\frac{1}{3}} \quad (7.4)$$

This equation connects the empirical parameters, the percolation threshold and the critical exponent, directly to the localization length. Therefore we can simply estimate localization of the systems which are previously reported with the empirical scaling laws.

We fabricated hole-only devices to test the models against typical OLED charge transport characteristics. Figure 7-2(a) shows the device structure. Tris(4-carbazoyl-9-ylphenyl)amine (TCTA) is the hole-transporting material with $\rho^{-1/3} = 10.3 \text{ \AA}$. 1,3-bis(3,5-dipyrid-3-yl-phenyl)benzene (BmPyPb) is an electron transporting material which functions here as an insulating host due to the deep HOMO level. TAPC (1,1-bis[(di-4-tolylamino)phenyl]cyclohexane) is used as a hole-injection and electron-blocking layer. The high

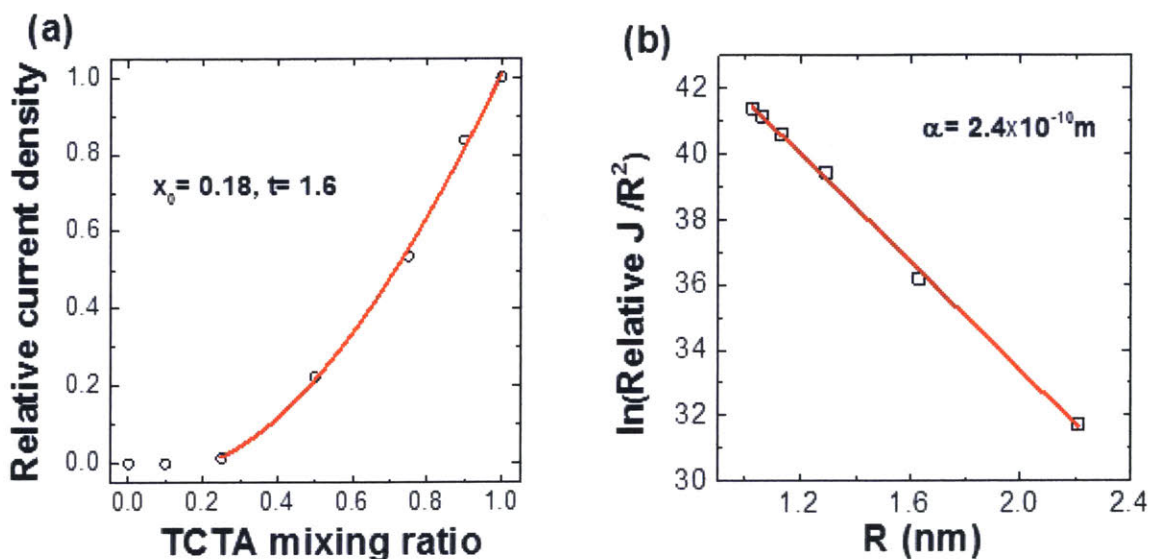


Figure 7-3 (a) Relative current density as a function of TCTA mixing ratio. Fitting of the percolation scaling law, red line, gives the (x_0, t) of (0.18, 1.6). (b) Relative current density as a function of the hopping distance. Fitting with the MA hopping model gives α of 2.4 Å.

LUMO level of TAPC prevents the injection of electrons. The TCTA concentration in the mixed layer is varied from 10 to 100 %. The devices were fabricated with a thermal evaporator without breaking vacuum ($< 2 \times 10^{-7}$ Torr). The thickness of the mixed layer is 20 nm, which is similar to the typical emission layer thickness in OLEDs.

Current density –voltage characteristics of the devices are shown in Figure 7-2(d). As expected, the current density increases with the TCTA concentration. To analyze the data, we calculate the relative current density from the current density of the device divided by that of the device with a neat layer of TCTA. The results are shown inset of Figure 7-2(d). Note that the relative current density is constant over driving voltages from 5.7 V to 8.7 V. The average of the relative current density in the constant region is plotted as a function of TCTA ratio, x , in Figure 7-3(a) and hopping distance, R , in Figure 7-3(b). Both models fit well. For the MA model fitting, we assumed the mobility is proportional to the current density and carrier density is identical for

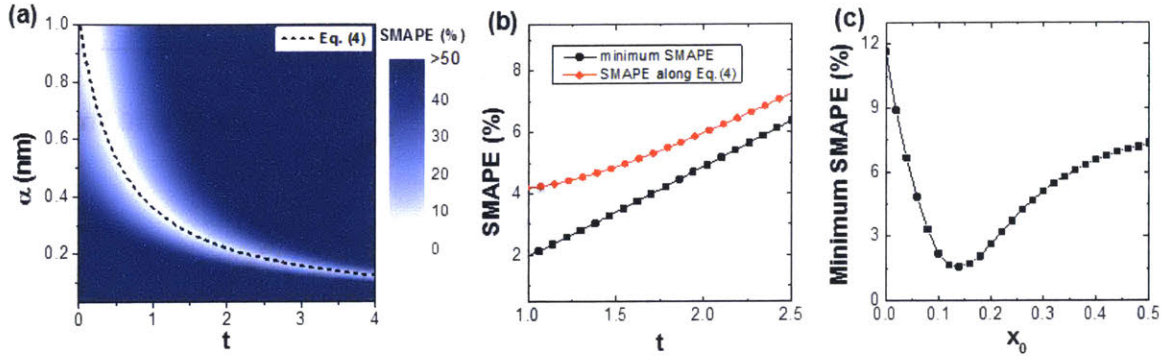


Figure 7-4 (a) Numerical calculation of the SMAPE, which is defined in Eq. (7.5), for the x_0 of 0.18. The dashed black line represents Eq. (7.4). It is well contained within the lowest error region. (b) Extracted minimum SMAPE for $1 < t < 2.5$ from (a) (black square), and the SMAPE along the Eq. (4) in (a) (red circle). (c) The minimum SMAPE for different x_0 values in the range of $1 < t < 2.5$.

the hole-only devices. The empirical percolative model yields $(x_0, t) = (0.18, 1.6)$, and the hopping transport model fits to $\alpha = 2.4 \text{ \AA}$ which is similar to that obtained previously in polymers.¹⁰³

To analyze the robustness of the link between the hopping and empirical percolation models, we calculate the symmetric mean absolute percentage error (SMAPE) between the two models with the boundary conditions of $x_0 + 0.05 < x < 1$ as defined in Eq. (7.5). The lower bound avoids the failure of the empirical percolation model at $x = x_0$.¹⁰⁴

$$SMAPE (\%) = \frac{100}{(1-(x_0+0.05))} \int_{x_0+0.05}^1 \left| \frac{C(x-x_0)^{t-\rho^{-2/3}} x^{-2/3} \exp(-2\rho^{-1/3} x^{-1/3}/\alpha)}{[C(x-x_0)^{t+\rho^{-2/3}} x^{-2/3} \exp(-2\rho^{-1/3} x^{-1/3}/\alpha)]/2} \right| dx \quad (7.5),$$

The prefactor C is a constant used to minimize the error for given (x_0, t, α) . Figure 7-4(a) shows the calculated SMAPE for the various values of t and α with fixed x_0 of 0.18. It is evident that the error is small in the white region, and the dashed line of Eq. (7.4) is contained within that region. A closer examination in Figure 7-4(b) shows the minimum SMAPE for $1 < t < 2.5$ varies from 2 to 6%. The SMAPE along the Eq. (7.4) line is about 1.5 percentage points bigger. These low values for the SMAPE demonstrate the analogy between the two models and also the validity of

the link described by Eq. (7.4). In Figure 7-4(c), the minimum SMAPE between the hopping and empirical percolation model is plotted for different x_0 values. The minimum SMAPE increases as x_0 approaching 0. Such low percolation thresholds are characteristic of mixtures of polymers and small molecules that are subject to phase separation.^{92,105,106} In this case, we cannot simply estimate the hopping distance as $\rho^{-1/3}x^{-1/3}$, thus this leads to a larger error between the two models.

Equation (7.4) could be further improved by consideration of assumptions and limitations. First, there are arguments about the coefficient of 2 in the exponential function of Eq. (7.2). Application of percolation theory to the MA hopping model gives a coefficient of 1.73, *i.e.* $\mu \propto R^2 \exp(-1.73R/\alpha)$.¹⁰⁷ We have also assumed that the transport regime is nearest-neighbor-hopping. For variable-range-hopping, the temperature and the energy levels of local molecules need to be considered. To do that, we should know the density of states (DOS) of molecules.¹⁰⁸ If we assume a Gaussian DOS, the standard deviation (σ) and thermal energy (kT) should be included in the exponential function. Nevertheless, it is valid to approximate the hopping model in the form of Eq. (7.2) for a limited range of R with respect to α and σ with respect to kT .^{102,109}

Consideration of a molecule's geometry could also enhance the accuracy of the modeling. Equation (7.2) is based on s-type wavefunctions. For elongated molecules, Eq. (7.2) could be modified by using p-type wavefunctions as $\mu \propto R^4 \exp(-2R/\alpha)$.¹¹⁰ When we derive Eq. (4), we put $x=1$ for simplicity. Further numerical calculation shows that evaluating at $x=0.75$ gives smaller error. Moreover, it is possible to simulate the system to get (x_0, t) following previous studies that calculated x_0 and t for a given crystal structure.^{91,111}

In conclusion, we have shown the analogy of hopping and percolative transport models for small molecular transport materials in mixed host layers. This verifies that the empirical

percolation scaling law is a reasonable approximation of the MA model for the analysis of charge transport in organic mixtures. The models were linked by a simple analytical expression that is robust across a wide range of parameters. Experimental results and numerical calculations support the result. The equation connects localization length to the percolation threshold and critical exponent, and it will help predict the electrical properties of mixtures of small molecules in practical device geometries.

While this has some associated fundamental interest by effectively deriving the empirical percolation scaling law, it also demonstrates that the conductivity of mixed host OLEDs is controlled by the wavefunction decay length, which is a fundamental parameter that can be readily estimated for any given material. Thus, this work allows the concentration dependence of charge transport in modern OLEDs to be predicted from first principles rather than fit empirically for each material. Consequently, this report should be of interest to organic LED researchers and, more generally, those interested in charge transport in disordered media.

7.2. Degradation of phosphorescent dyes

OLEDs are widely used for mobile devices, with growing applications in televisions and general solid-state lighting. Amidst this success, the greatest remaining challenge is to resolve the poor stability of high-efficiency blue OLEDs. Phosphorescent dyes^{112,113}, which emit from the usually non-radiative triplet state, are the leading commercial high-efficiency technology in red and green, but blue phosphorescent devices degrade to 90% of their initial luminance within 150 hours continuous operation at 1000 nits¹¹⁴.

There are many factors lead to the degradation of OLEDs, and they can be divided into extrinsic or intrinsic parameters¹¹⁵. The extrinsic factors such as temperature, pressure, encapsulation environment and fabrication process are easy to control independently, so the effect of those parameters are well understood^{116,117}. The intrinsic factors are materials properties and their derivatives. Examples of the intrinsic parameters are exciton decay rates, exciton diffusion length, energy levels, mobility, charge density and exciton density. Unfortunately, it is difficult to change one property of a molecule and keep all other properties identical, which makes systematic studies of intrinsic factors challenging. Because the effects of the intrinsic parameters are unknown, degradation models built so far required to hypothesize the effects and fits with many parameters¹¹⁸⁻¹²⁴. The available data, however, are frequently limited to macroscopic phenomena such as the total output luminance.

Diagnostic spectroscopy at the microscopic level must characterize exceedingly rare processes. For example, red phosphorescent OLEDs exhibit a decay time to 95% of initial luminance (*LT95*) of ~20,000 hours at an operating brightness of 1000 nits¹²⁵. Given that the active phosphorescent dye is present at 3% loading in a 30-nm-thick emissive layer, this yields more than 60 *billion* excitons per dye to *LT90*.

Given the challenges that confront the rational design of OLED materials, it is important to determine whether there are any general characteristics of OLED failure processes that can be resolved through device engineering. We focus on long-lived triplet excitons, which are common to all OLEDs, and are hypothesized as an important energy source for degradation processes. The total energy stored in triplet excitons is dependent on the triplet exciton generation rate, G , and the triplet exciton lifetime, τ . Using these two key parameters, we construct a simple model of OLED degradation based on three primary classes of known failure mechanisms.

7.2.1. Degradation model

As shown in Table 7-1, the first class (i) of degradation mechanisms is unimolecular pathways. Examples include spontaneous degradation of a given molecule in its excited state, or an impurity-assisted process such as photo-oxidation¹²⁶. Unimolecular processes are distinguished from the other classes because they scale linearly with the number of triplet excited

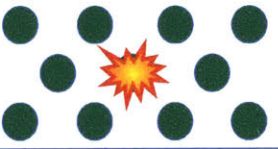
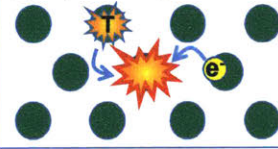
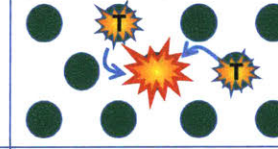
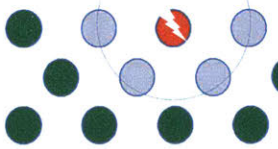
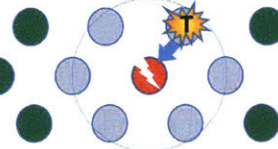
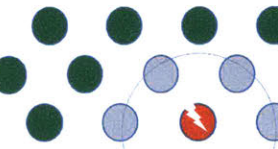
	(i) Unimolecular process	(ii) Triplet-Charge Interaction	(iii) Triplet-Triplet Interaction
Defect generation mechanism			
Defect generation rate	$\propto G\tau$	$\propto G^{1.5}\tau$	$\propto G^2\tau^2$
Excitons quenched by defects			
Quenching loss		$\propto \tau$	
1/LT90	$\propto G\tau^2$	$\propto G^{1.5}\tau^2$	$\propto G^2\tau^3$

Table 7-1 The three classes of degradation mechanisms that generate degraded molecules within an OLED and their defect generation rate as a function of triplet exciton-generation rate (G) and triplet exciton lifetime (τ). The dependence of the OLED lifetime to 90% of initial luminance (LT90) on the triplet exciton lifetime is significant because exciton lifetime not only contributes to the triplet exciton density, but also influences quenching losses at defect sites.

states in the OLED. The second class (*ii*) of degradation mechanism is triplet-charge interactions^{119,127}. Here, triplet excitons collide with a charged molecule, forming a high energy state which initiates permanent damage to one of the molecules. Assuming that the charge density is determined by non-geminate recombination, these processes are expected to scale as the excitation intensity to the power of 1.5¹²⁸. The final class (*iii*) of degradation mechanism is triplet-triplet interactions¹¹⁴. Here, triplet excitons collide, forming a high energy state leading to permanent damage to a molecule. These processes scale quadratically with the number of excited states in the OLED¹²⁹.

Once formed, a damaged molecular site in some instances may quench neighboring molecules, thereby amplifying the impact on an OLED's performance^{130–132}. Including quenching by defects, the expected dependence of each class of degradation mechanism on the overall triplet exciton lifetime τ , and the triplet exciton generation rate G can be derived as follow.

The defect generation rates for the three degradation mechanisms can be summarized as

$$\frac{d[D]}{dt} = k_{D,T}[T] \quad (7.6a)$$

$$\frac{d[D]}{dt} = k_{D,TC}[T][P] \quad (7.6b)$$

$$\frac{d[D]}{dt} = k_{D,TT}[T]^2 \quad (7.6c)$$

where we define the triplet exciton density $[T]$, the defect density $[D]$, the charge density $[P]$, and the degradation rate constants for unimolecular, exciton-exciton, and exciton-charge degradation processes, $k_{D,T}$, $k_{D,TT}$, and $k_{D,TC}$, respectively. Crucially, a damaged molecular site may quench

neighboring molecules, thereby amplifying the impact on an OLED's performance. Including quenching by defects, the expected dynamics of triplet excitons is:

$$\frac{d[T]}{dt} = G - k_R[T] - k_{NR}[T] - k_{ET}[D][T] \quad (7.7)$$

where we further define the exciton pumping rate G , the radiative rate k_R , the nonradiative rate k_{NR} , and the rate of energy transfer to defects $k_{ET}[D]$.

Then, the photoluminescence quantum yield (PLQY, η) and its derivative are,

$$\eta = \frac{k_R}{k_R + k_{NR} + k_{ET}[D]} \quad (7.8)$$

$$\frac{d\eta}{dt} = -\frac{k_R}{(k_R + k_{NR} + k_{ET}[D])^2} \cdot k_{ET} \frac{d[D]}{dt} = -\frac{k_{ET}}{k_R} \eta^2 \frac{d[D]}{dt} \quad (7.9)$$

We define the initial exciton lifetime (τ) of an emitter molecule as,

$$\tau \equiv \frac{1}{k_R + k_{NR}} \quad (7.10)$$

Initially $[D]_0 = 0$, and the degradation rate is much slower than the exciton decay rate. We also define the initial triplet exciton density as:

$$[T]_0 = G\tau \quad (7.11)$$

From Eqn (7.7) and (7.11),

$$\left. \frac{d[D]}{dt} \right|_{t=0} = k_{D,T}G\tau + k_{D,TC}G^{1.5}\tau + k_{D,TT}G^2\tau^2 \quad (7.12)$$

From Eqn (7.5) and (7.12),

$$\left. \frac{d\eta}{dt} \right|_{t=0} = -\frac{k_{ET}}{k_R} \eta_0^2 \left. \frac{d[D]}{dt} \right|_{t=0} = -k_{ET}k_R(k_{D,T}G\tau^3 + k_{D,TC}G^{1.5}\tau^3 + k_{D,TT}G^2\tau^4) \quad (7.13)$$

At time t , PLQY changes due to the increase of $[D]$.

$$\eta = \frac{k_R}{1/\tau + k_{ET}[D]} \quad (7.14)$$

Since we assumed the degradation rate is a lot slower than the exciton decay rate,

$$[T] = \frac{G}{1/\tau + k_{ET}[D]} \quad (7.15)$$

Then, the defect generation rate is,

$$\left. \frac{d[D]}{dt} \right|_t = k_{D,T} \frac{G}{1/\tau + k_{ET}[D]} + k_{D,TC} \frac{G^{1.5}}{1/\tau + k_{ET}[D]} + k_{D,TT} \left(\frac{G}{1/\tau + k_{ET}[D]} \right)^2 \quad (7.16)$$

From Eqn (7.15), (7.14) and (7.16),

$$\begin{aligned} \left. \frac{d\eta}{dt} \right|_t &= -\frac{k_{ET}}{k_R} \eta^2 \left. \frac{d[D]}{dt} \right|_t \\ &= -k_{ET} k_R \left[\frac{k_{D,T} G}{(1/\tau + k_{ET}[D])^3} + \frac{k_{D,TC} G^{1.5}}{(1/\tau + k_{ET}[D])^3} + \frac{k_{D,TT} G^2}{(1/\tau + k_{ET}[D])^4} \right] \\ &= -\frac{k_{ET} k_{D,T} G}{k_R^2} \eta^3 - \frac{k_{ET} k_{D,TC} G^{1.5}}{k_R^2} \eta^3 - \frac{k_{ET} k_{D,TT} G^2}{k_R^3} \eta^4 \end{aligned} \quad (7.17)$$

Eqn (7.17) can be solved numerically. However, it has an analytical solution if one degradation mechanism is dominant as shown below.

$$\eta(t) = \frac{1}{\sqrt{C_T t + 1/\eta_0^2}} \quad \text{where } C_T = \frac{2k_{ET} k_{D,T} G}{k_R^2} \quad (7.18a)$$

$$\eta(t) = \frac{1}{\sqrt{C_{TC} t + 1/\eta_0^2}} \quad \text{where } C_{TC} = \frac{2k_{ET} k_{D,TC} G^{1.5}}{k_R^2} \quad (7.18b)$$

$$\eta(t) = \frac{1}{\sqrt[3]{C_{TT} t + 1/\eta_0^3}} \quad \text{where } C_{TT} = \frac{3k_{ET} k_{D,TT} G^2}{k_R^3} \quad (7.18c)$$

Since we know the initial PLQY, there is only one fitting parameter. On the contrary, previous degradation models have more than 2 fitting parameters, and there is no physical meaning in the parameter. Based on Eqn (7.18), the solutions for T90 are,

$$T_{90,T} = \frac{0.12}{k_{ET} k_{D,T}} * \frac{1}{G\tau^2} \quad (7.19a)$$

$$T_{90,TC} \doteq \frac{0.12}{k_{ET}k_{D,TC}} * \frac{1}{G^{1.5}\tau^2} \quad (7.19a)$$

$$T_{90,TT} \doteq \frac{0.12}{k_{ET}k_{D,TT}} * \frac{1}{G^2\tau^3} \quad (7.19a)$$

The model can be extended further by adding additional degradation mechanisms. If the degradation mechanism is caused by reaction with an impurity such as oxygen,

$$\frac{d[D]}{dt} = k_{D,ox}[O_2][T] \quad (7.20)$$

If there is no continuous oxygen source, the oxygen level will decrease exponentially.

$$[O_2] = [O_2]_0 \exp(-k_{D,ox}[T] t) \approx [O_2]_0 \exp(-t/\tau_{ox}) \quad (7.21)$$

In Eqn (7.21), we approximate that the triplet density remains constant during the oxidation process. This is the case when the oxidation causes a few percent of degradation and occurs fast at the early stage of degradation. Then, the corresponding degradation rate and the luminance change are,

$$\frac{d\eta}{dt} = -\frac{k_{ET} k_{D,ox}[O_2]_0 G}{k_R^2} \eta^3 \exp(-t/\tau_{ox}) \quad (7.22)$$

$$\eta = \frac{1}{\sqrt{-C_{ox} \exp(-t/\tau_{ox}) + C_{ox} + 1/\eta_0^2}} \quad \text{with } C_{ox} = \frac{2\tau_{ox} k_{ET} k_{D,ox}[O_2]_0 G}{k_R^2} \quad (7.23)$$

If the degradation mechanism is a combination of oxidation and triplet-charge interaction,

$$\eta = \frac{1}{\sqrt{-C_{ox} \exp\left(-\frac{t}{\tau_{ox}}\right) + C_{TC}t + C_{ox} + 1/\eta_0^2}} \quad (7.24)$$

If the degradation mechanism is a combination of the oxidation and the triplet-triplet interaction, the degradation curve can be obtained from solving the below differential equation.

$$\frac{d\eta}{dt} = -\frac{k_{ET} k_{D,ox}[O_2]_0 G}{k_R^2} \eta^3 \exp\left(-\frac{t}{\tau_{ox}}\right) - \frac{k_{ET} k_{D,TT} G^2}{k_R^3} \eta^4 \quad (7.25)$$

From the above derivation, we can conclude followings.

$$1/LT90 \propto G\tau^2 \quad (i), \quad 1/LT90 \propto G^{1.5}\tau^2 \quad (ii), \quad 1/LT90 \propto G^2\tau^3 \quad (iii) \quad (7.26)$$

where the solutions for unimolecular, triplet-charge, and triplet-triplet cases are marked (i), (ii), and (iii), respectively. $LT90$ is the time required for the OLED to degrade to 90% of initial luminance. The same dependencies are expected for $LT97$ and $LT95$, and we measure $LT90$ in this study.

Equation 7.26 suggests that, in each case, the dependence of stability on triplet exciton lifetime is dramatic, stronger even than the dependence on generation rate. Therefore, if the triplet exciton lifetime can be reduced via device engineering, the intrinsic degradation rate can be inhibited. For example, in the case of degradation due to triplet-triplet annihilation, the dependence on triplet exciton lifetime is *cubic*. Conceptually, we can understand degradation in terms of the energy density stored in the device; the energy density depends equally on the generation rate and the triplet exciton lifetime. However, Eq.7.26 indicates the exciton lifetime plays a more dominant role than simple reduce of energy density. The additional dependence on triplet exciton lifetime is due to quenching of other triplet excitons at defect sites.

7.2.2. Photodegradation measurement

To test the predictions for triplet-triplet and triplet-charge induced degradation, we engineer a reduction in triplet exciton lifetime to allow exciton decay into the plasmonic modes to outcompete the quenching processes. The result is an increased dependence of stability on τ compared to G . To do this we consider optically pumped films of green and blue Ir-based phosphorescent dyes. The green emitter is the well-studied phosphorescent dye *fac*-tris(2-phenylpyridine) Iridium(III) ($\text{Ir}(\text{ppy})_3$). It is employed as a neat film, where it exhibits strong triplet-triplet annihilation¹³³, sandwiched by the host material 4,4'-bis(N-carbazolyl)-1,1'-biphenyl (CBP). The second material is *fac*-tris[3-(2,6-dimethylphenyl)-7-methylimidazo(1,2-f)phenanthridine] Iridium(III) ($\text{Ir}(\text{dmp})_3$) doped at 10% by volume into 3,3'-bis(N-

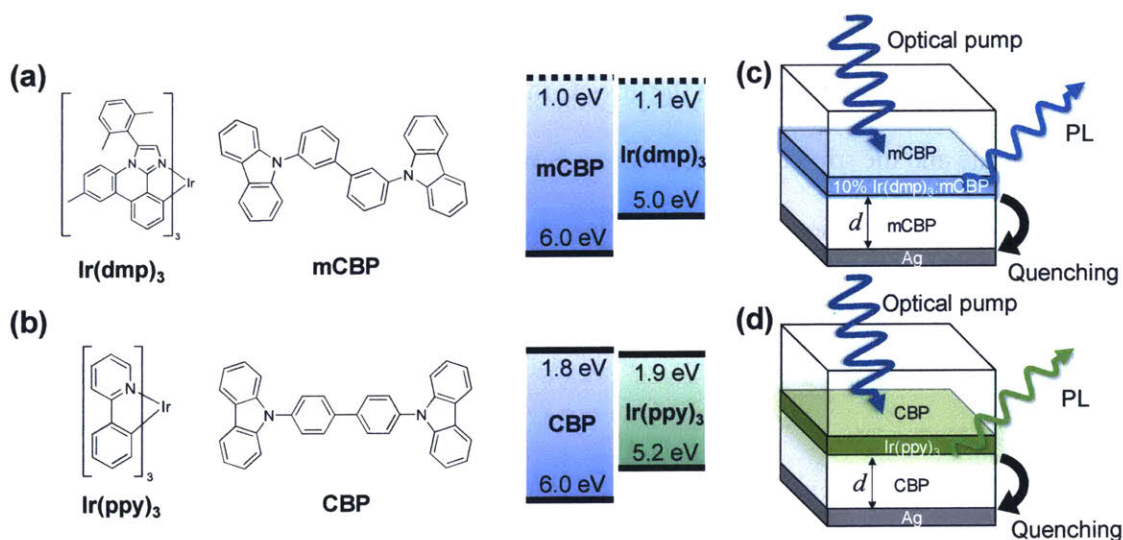


Figure 7-5 The chemical structures and energy levels of (a) blue, and (b) green emission layer. The HOMO levels were measured by ultraviolet photoemission spectroscopy for $\text{Ir}(\text{ppy})_3$, CBP, $\text{Ir}(\text{dmp})_3$, and mCBP^{134,140}. The LUMO levels of $\text{Ir}(\text{ppy})_3$ and CBP were determined by inverse photoemission spectroscopy¹⁴⁰. The LUMO levels of $\text{Ir}(\text{dmp})_3$ and mCBP were determined from the optical gaps¹³⁴ and assuming identical exciton binding energies in $\text{Ir}(\text{ppy})_3$ and CBP, respectively. The sample structure for the blue system (c) is Ag(34 nm)/mCBP(10, 20, 45, 150 nm)/Emission layer(10 nm)/mCBP(10 nm) and the green system (d) is Ag(20 nm)/CBP(0, 5, 10, 20, 45, 100 nm)/Emission layer(10 nm)/CBP(10 nm).

methylcarbazolyl)-1,1'-biphenyl (mCBP) sandwiched by the host material mCBP. The lowest unoccupied molecular orbital (LUMO) of mCBP is near in energy to the LUMO of Ir(dmp)₃ such that free charge is generated under optical excitation of the system. The degradation behavior of this system is dominated by triplet-charge interactions¹³⁴. The chemical structures and energy levels of these materials are shown in Figure 7-5(a) and (b).

To control the exciton lifetime of the phosphorescent dyes, we deposit them on films of Ag with a host material spacer layer of variable thickness, *d*. As shown in Figure 7-5(c) and (d), this approach exploits the well-known phenomenon of non-radiative energy transfer to surface plasmon polaritons in the Ag film^{135–137}. The combination of the guest-host systems of varying concentration at a tunable spacer layer distance from an adjacent silver film allows us to systematically vary the degradation mechanism and triplet exciton lifetime, without the need to chemically modify the materials to do so.

The transient photoluminescence (PL) responses for varying spacer thicknesses are shown in Figure 7-6(a) and (b). To determine the impact of triplet exciton lifetime on stability, we measure the photostability of the samples under continuous excitation by a $\lambda = 405$ nm laser; see Figure 7-6(c) and (d).

As predicted by Equation (7.26), we find that the films with longer triplet exciton lifetimes degrade faster. For each film, we extract the time required for the PL intensity to fall to 90% of its initial value (LT_{90}). Care is taken to ensure that the optical generation rate of triplet excitons is identical for all films. The pump power is corrected based on the transfer-matrix

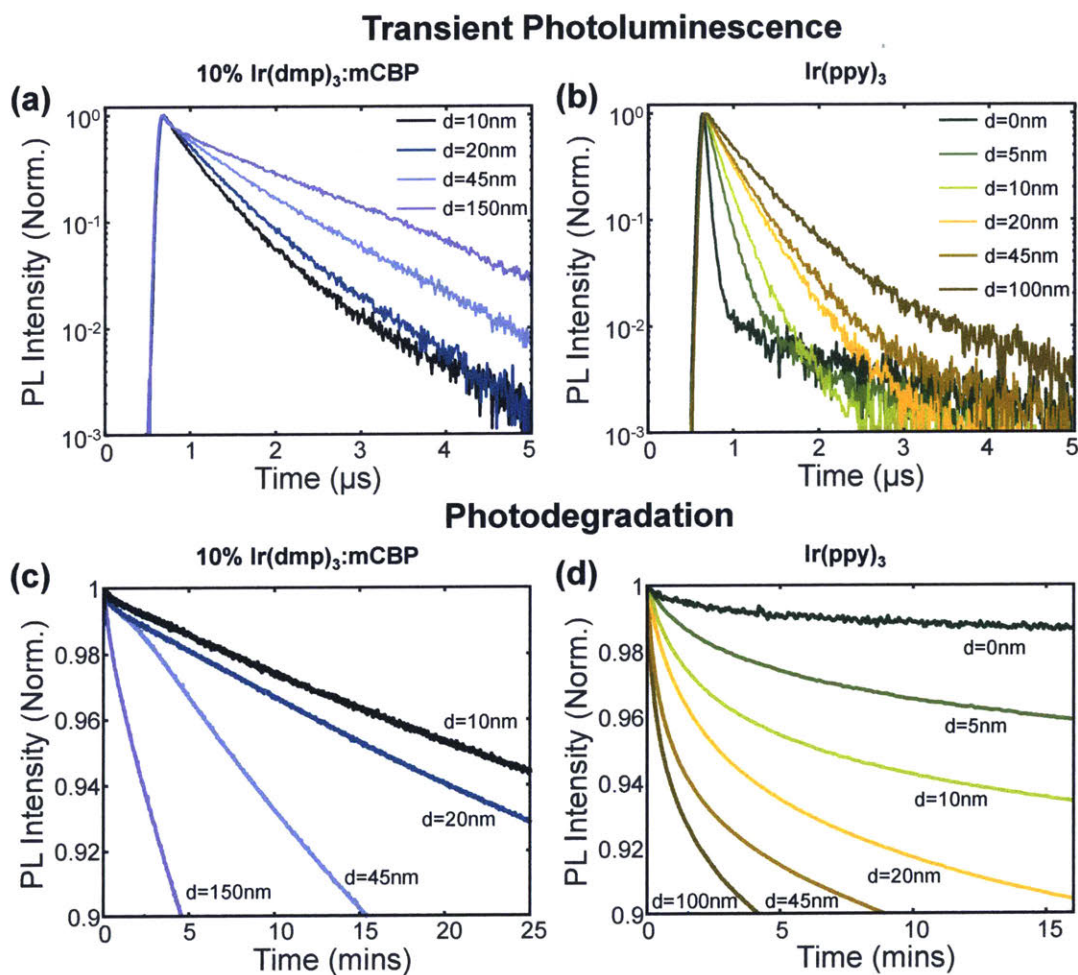


Figure 7-6 Transient photoluminescence of (a) 10% $\text{Ir}(\text{dmp})_3:\text{mCBP}$ and (b) neat $\text{Ir}(\text{ppy})_3$, as a function of varying spacer thickness d . As expected, reducing the distance between the emission layer and the Ag corresponds to increasingly fast exciton decay due to strong coupling to the non-radiative surface plasmonic modes in Ag. The photodegradation curves for the (c) blue and (d) green systems as a function of d . Samples with emission layers closer to Ag experience a stabilizing effect, i.e. slower photodegradation due to the shorter exciton lifetime.

calculation of absorption¹³⁸ and in accordance with experimentally determined pump-power dependencies for each sample.

The primary experimental variable in this study is d , the spacing between an emissive layer of dye molecules and a silver film. Alterations to d change the exciton lifetime in the dye, but also its optical absorption. To compare the photodegradation rates of samples with differing optical absorptions, we first calculated the absorption of each sample using a transfer-matrix method¹³⁸ and verified the calculations experimentally as shown in Figure 7-7. Neat films rather than doped samples were characterized to ensure measurable absorption in 10-nm-thick emissive layers. The sample structure was identical to the degradation samples. Additionally, we prepared reference samples which replaced the Ir(ppy)₃ layer with CBP to measure the silver absorption.

Using the absorption estimates, we ensured that the exciton generation rate was constant across samples with varying d , either by varying the optical pump power directly (doped Ir(ppy)₃

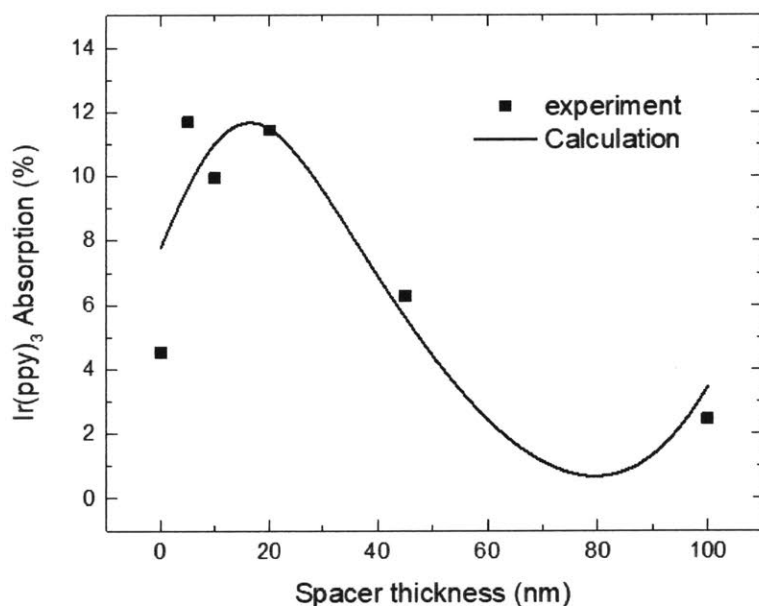


Figure 7-7 Transfer matrix calculation for neat Ir(ppy)₃ samples for different spacer layer and experimental data measured by the integrating sphere. The absorption is corrected based on this calculation.

and doped Ir(dmp)₃) or by adjusting the data after the measurement (neat Ir(ppy)₃). In neat Ir(ppy)₃ samples, the *LT*90s of samples with varying *d* were shifted with respect to each other according to the measured optical pump power dependence for each spacer thickness and then normalized.

7.2.3. Dominance of exciton lifetime in stability

Using the data in Figure 7-6, we extract the measured dependence of phosphorescent dye stability on the triplet exciton lifetime, τ . We summarize these results in Figure 7-8 where we show the degradation behaviors of both 10% Ir(dmp)₃:mCBP and neat Ir(ppy)₃. The dependence of stability for each system on τ is substantial, as predicted by Eq. 7.26. The stability of 10% Ir(dmp)₃:mCBP, which is dominated by triplet-charge interactions, exhibits a power law dependence on τ with an exponent of 2.9. For neat Ir(ppy)₃, dominated by triplet-triplet degradation events, the power law dependence of stability on τ is 3.6. A seven-fold reduction in exciton lifetime thus leads to a *1000-fold* improvement in the photostability of neat Ir(ppy)₃. We note that all of the measured power law dependencies on τ are larger than the predictions in Eq. 7.26. For the doped system, which generates charges, the discrepancy could be partially due to the dissociation of triplet excitons into charges which yields $1/LT90 \propto \tau^{2.5}$. The systematically steeper slopes may also suggest that additional triplet dynamics play a role in the quenching process. For example, triplet exciton diffusion is ignored in the simple model of Eq. 7.26, but is expected to increase the impact of defects as the triplet lifetime and diffusion distance increases¹³⁹. The experimental data nevertheless confirm that the simple model of Eq. 7.26 provides a conservative estimate for the potential stability improvements achievable with changes in triplet lifetime.

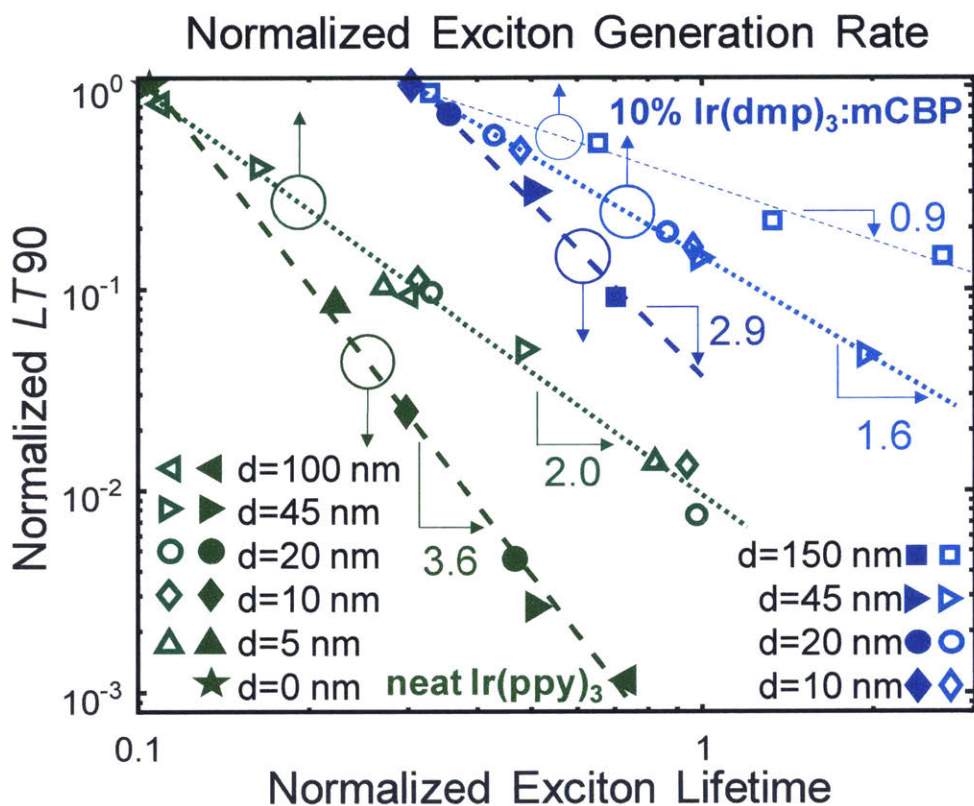


Figure 7-8 The stability in both green (neat Ir(ppy)₃) and blue (10% Ir(dmp)₃:mCBP) systems as a function of the generation rate of triplet excitons, G , and the triplet exciton lifetime, τ . As we predicted from the degradation model, the exciton lifetime has much stronger impact on the degradation rather than exciton generation rate for both systems. The difference in slope between the green and blue system is due to the different degradation mechanism. The slope of the pump-power dependence indicates that neat Ir(ppy)₃ degrades from triplet-triplet annihilation and the doped Ir(dmp)₃ degrades from triplet-charge annihilation. Note that the degradation mechanism changes from triplet-charge annihilation to unimolecular process when d is 150nm. Values for LT90 are extracted from the data presented in Figure 7-6 and plotted on a normalized logarithmic scale against (top) triplet exciton generation rate (G) and (bottom) triplet exciton lifetime (τ).

We also characterized neat Ir(dmp)₃, which exhibited green excimer emission and was not studied further. A doped green system, 10% Ir(ppy)₃:CBP, was found to behave similarly to 10% Ir(dmp)₃:mCBP. The exciton lifetime dependence gives exponent of 2.4 which corresponds to triplet-charge degradation (Figure 7-9). Also the pump power dependence is 1.5 as shown in Table 7-2. Similar to Ir(dmp)₃:mCBP, where electron and hole transport occurs preferentially on

the host and guest, respectively¹³⁴, the Ir(ppy)₃:CBP system can separate charge under photoexcitation. In Figure 7-5 (a), it is notable that the LUMO levels are similar for the guest and host in each material combination studied in this work^{140–142}. One consequence of this is that both Ir(ppy)₃:CBP and Ir(dmp)₃:mCBP systems generate appreciable charge under photoexcitation.

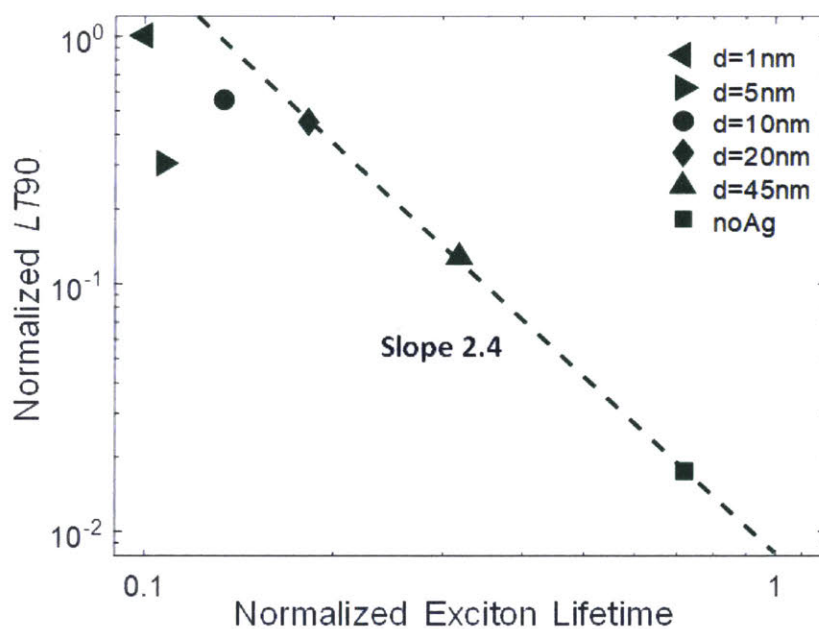


Figure 7-9 Exciton lifetime dependence of 10% Ir(ppy)₃:CBP degradation. The slope is 2.4 which indicates the triplet-charge degradation based on our degradation model. LT90s for emission layers very close to Ag are reduced compared to the trend at larger distances from Ag.

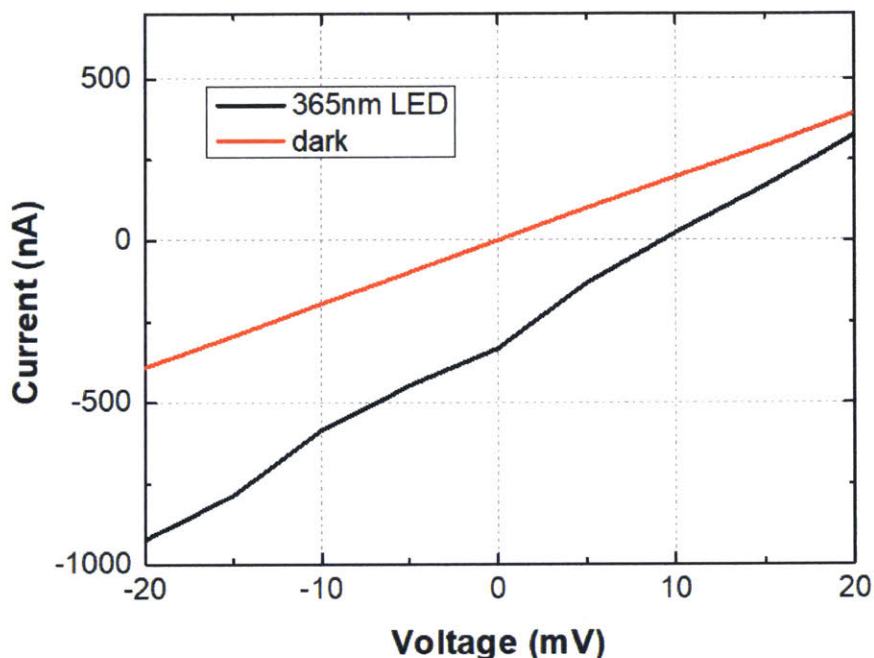


Figure 7-10 Photocurrent of a 10% Ir(ppy)₃:CBP photovoltaic device. The device structure is ITO(100nm)/10% Ir(ppy)₃:CBP (60nm)/Al (80nm), and it is exposed to a $\lambda=365$ nm LED with 5.6 W/cm². The open circuit voltage is 9.3 mV and the short circuit current density is

In order to experimentally confirm charge generation in the doped green emissive layers, we photoexcited a 10% Ir(ppy)₃:CBP film sandwiched between an indium tin oxide (ITO) and an aluminum electrode (ITO (100nm)/Ir(ppy)₃:CBP (10%, 60nm)/Al (80nm)). As shown in Figure 7-10, this resulted in generation of photocurrent in the 10% Ir(ppy)₃:CBP film, confirming the presence of charge carriers in the emissive layer upon photoexcitation.

The charging is exacerbated in the vicinity of the silver film, where it is characterized by the onset of delayed luminescence in the transient PL. The presence of multiple distinct lifetimes and the evidence of additional dynamics close to the silver cause us to neglect samples characterized by strong delayed luminescence.

The dependence of photodegradation on the triplet exciton generation rate offers an additional test of the predictions in Eq. 7.26. The relevant data for neat Ir(ppy)₃ and 10% Ir(dmp)₃:mCBP is shown in Figure 7-8, and the pump-power dependence of 10% Ir(ppy)₃:CBP is shown in Table 7-2.

With Ag - 10% doped films		No Silver	
d	Power Law	Doping ratio	Power Law
1nm	1.72	10%	1.00
5nm	1.40	20%	0.94
10nm	1.64	50%	1.25
20nm	1.40	100%	1.91
45nm	1.32		

Table 7-2 Triplet exciton generation rate dependence of the photodegradation of Ir(ppy)₃:CBP. On the left, we summarize varying CBP spacer thickness for 10% Ir(ppy)₃:CBP films. The structure employed is Ag(20 nm)/CBP(1, 5, 10, 20, 45 nm)/10% Ir(ppy)₃:CBP(10 nm)/CBP(10 nm). On the right, we summarize, the concentration dependence in the absence of a silver film. The structure is CBP (10 nm)/10% Ir(ppy)₃:CBP(10 nm)/ CBP (10 nm). As is the case for 10% doped Ir(dmp)₃:mCBP, samples that include a silver layer exhibit pump power laws with exponents of approximately 1.5, consistent with the presence of triplet-charge interactions. In the absence of the silver film, the power law slopes are around 1, indicates unimolecular degradation. Note that the slope becomes nearly 2 for neat Ir(ppy)₃, due to the strong triplet-triplet annihilation.

The results are consistent with expectations^{128,129} for triplet-charge and triplet-triplet induced degradation in the doped systems and neat Ir(ppy)₃, respectively. We find that the power law governing the dependence of pump intensity has a slope of approximately 1.5 for the 10% doped systems and 2.0 for neat Ir(ppy)₃, as predicted by Eq. 7.26 (ii) and 1(iii), respectively. Interestingly, doped Ir(ppy)₃ in the absence of a silver film and doped Ir(dmp)₃ with large separation of 150 nm between the emission layer and the silver film yield power law slopes of approximately 1. In both cases, the apparent charging in the materials is reduced, yielding

unimolecular power-law dependencies. We note that these systems are unlikely to be relevant to OLEDs, given the substantial densities of charge expected in OLEDs under bias. We also characterize photodegradation as a function of the Ir(ppy)₃ doping ratio in CBP films, observing the expected transition to triplet-triplet interactions at high doping densities

In summary, OLEDs convert injected charge into light by first forming excited states localized on dye molecules. The energy density created by the accumulation of these excited states determines the generation rate of luminance-killing defects. We have shown that reducing the lifetime of triplet excited states is an effective way to alleviate degradation by reducing both overall energy density and energy transfer to defects. The potential stability improvement is significant, more than enough to stabilize phosphorescent blue materials for many applications. Considering the result in the context of modern OLEDs, we note that this approach can be universally applied to phosphorescent dyes, which are unique in that their long-lived states are radiative, opening the possibility of new photonic and plasmonic designs for increasing the stability of phosphorescent OLEDs. Such designs could be incorporated within OLED contacts using the Purcell effect to rapidly extract energy from the phosphorescent emitter via the plasmonic coupling. The associated benefit to stability has been demonstrated here, but the OLED contacts must also radiate the energy back to free space, rather than simply quenching the excitons as in this work. Furthermore, faster energy extraction from OLEDs also promises to reduce efficiency droop at high excitation densities^{129,143}, a key challenge for future OLED applications.

7.2.4. Experimental methods

Photoluminescent samples were grown via vacuum thermal evaporation. Prior to any organic layer deposition or coating, the soda-lime glass substrate was degreased with solvents,

dried, and then treated with oxygen plasma for 1.5 minutes and ultra violet ozone for 5 minutes. The samples were fabricated in high vacuum ($< 10^{-6}$ Torr). The Ag layer was fabricated on a 10 Å thick Aluminum adhesion layer followed by the specified thickness of Ag. All layers were grown at a rate of either 1 or 2 Å/s. All samples were encapsulated with a glass lid and sealed with an ultra violet cured epoxy in a nitrogen glove box (< 1 ppm of H₂O and O₂) immediately after fabrication. For doped layers, doping percentages are in volume percent. All samples were prepared at Universal Display Corporation.

Ellipsometry data was measured with a J.A. Woollam RC2 variable angle ellipsometer. To accurately determine the optical constants and thicknesses of the metal layers, thin layers of the metal were grown on a Si wafer with a ~ 1500 Å thermal oxide.

For the photodegradation measurement, a $\lambda = 405$ nm laser (CPS405, Thorlabs) was used as the excitation source. The excitation power deviation was tracked with a 90:10 beam splitter and a silicon photodetector (818-SL, Newport). A $\lambda = 450$ nm short pass filter was used for the excitation power detection. Another silicon photodetector was used for PL detection with a $\lambda = 450$ nm longpass filter and a $\lambda = 700$ nm shortpass filter. The photodetectors were connected to two lock-in amplifiers (SR830, Stanford Research Systems) to reduce measurement noise. The sample was excited at 45-degree angle and detection optics were placed to normal direction. All measurements were done in an optical enclosure. Transient PL was measured with a streak camera (Hamamatsu C11200 and a $\lambda=371$ nm laser diode).

The absorption of Ir(ppy)₃ neat film was measured by using an integrating sphere (RTC-060-SF, Labsphere). A $\lambda = 405$ nm laser diode (CPS405, Thorlabs) was used as the excitation source and a silicon detector connected to lock-in amplifiers (SR830, Stanford Research Systems) measured the transmitted light collected within the sphere. We measured the light

collected within the sphere for 3 configurations: direct excitation of samples, indirect excitation, and the laser signal in the absence of samples. From this we obtained the absorption of the sample. The absorption of the Ir(ppy)₃ layer is obtained by subtracting the absorption of the samples from the reference samples which contain no Ir(ppy)₃.

List of publications

1. D.-G. Ha, M. Rezaee, Y. Han, S. Siddiqui, L. Xie, R. Day, B. Modtland, J. Finely, D. Muller, J. Kong, P. Kim, M. Dinca and M. A. Baldo, “*Single-crystal plates of a two-dimensional π -conjugated metal-organic framework*” (in preparation)
2. D.-G. Ha, J. Kong, M. Dinca and M. A. Baldo “*Growth mechanisms of two-dimensional π -conjugated metal-organic frameworks*” (in preparation)
3. D.-G. Ha†, J. Tiefert†, M. A. Fusella, M. S. Weaver, J. Brown, M. Einzinger, M. Sherrott, T. V. Voorhis, N. J. Thompson, and M. A. Baldo “*Dominance of Exciton Lifetime in the Stability of Phosphorescent Dyes*” (Submitted)
4. H. Tsujimoto, D.-G. Ha, G. Markopoulos, H. S. Chae, M. A. Baldo, and T. M. Swager “*Thermally Activated Delayed Fluorescence and Aggregation Induced Emission with Through-Space Charge Transfer*” Journal of American Chemical Society, 139, 4894 (2017)
5. R. Gómez-Bombarelli, J. Aguilera-Iparraguirre, T. D. Hirzel, D. Duvenaud, D. Maclaurin, M. A. Blood-Forsythe, H. S. Chae, M. Einzinger, D.-G. Ha, T. Wu, G. Markopoulos, S. Jeon, H. Kang, H. Miyazaki, M. Numata, S. Kim, W. Huang, S. I. Hong, M. Baldo, R. P. Adams and A. Aspuru-Guzik, “*Design of efficient molecular organic light-emitting diodes by a high-throughput virtual screening and experimental approach*” Nature Materials, 15, 1120 (2016)
6. D.-G. Ha, J.-J. Kim, M. A. Baldo, “*Link between hopping models and percolation scaling laws for charge transport in mixtures of small molecules*” AIP Advances, 6, 045221 (2016)

Patent

1. U.S. patent (filed, 15867004) “Emissive compounds and related devices”, T. M. Swager, H. Tsujimoto, G. Markopoulos, D.-G. Ha, M. A. Baldo

Bibliography

1. Yaghi, O. *et al.* Reticular synthesis and the design of new materials. *Nature* **423**, 705 (2003).
2. Ferey, G. Hybrid porous solids : past , present , future. *Chem. Soc. Rev.* **37**, 191–214 (2008).
3. Batten, S. R. *et al.* Terminology of metal – organic frameworks and coordination polymers (IUPAC Recommendations 2013)*. *Pure Appl. Chem.* **85**, 1715–1724 (2013).
4. Polishchuk, P. G., Madzhidov, T. I. & Varnek, A. Estimation of the size of drug-like chemical space based on GDB-17 data. *J. Comput. Aided. Mol. Des.* **27**, 675–679 (2013).
5. Furukawa, H., Cordova, K. E., Keffe, M. O. & Yaghi, O. M. The Chemistry and Applications of Metal-Organic Frameworks. *Science (80-.).* **341**, 974 (2013).
6. Berg, A. W. C. Van Den & Arean, C. O. Materials for hydrogen storage : current research trends and perspectives. *Chem. Commun.* 668–681 (2008). doi:10.1039/b712576n
7. Gándara, F., Furukawa, H., Lee, S. & Yaghi, O. M. High Methane Storage Capacity in Aluminum Metal–Organic Frameworks. *J. Am. Chem. Soc.* **136**, 5271–5274 (2014).
8. <https://www.numat-tech.com/ion-x-oem-data/>.
9. Sumida, K. *et al.* Carbon Dioxide Capture in Metal-Organic Frameworks. *Chem. Rev.* **112**, 724–781 (2012).
10. Li, J. R., Kuppler, R. J. & Zhou, H. C. Selective gas adsorption and separation in metal-organic frameworks. *Chem. Soc. Rev.* **38**, 1477–1504 (2009).
11. Kim, H. *et al.* Water harvesting from air with metal-organic frameworks powered by natural sunlight. *Science (80-.).* **356**, 430 (2017).
12. Khan, N. A., Hasan, Z. & Jhung, S. H. Adsorptive removal of hazardous materials using metal-organic frameworks (MOFs): A review. *J. Hazard. Mater.* **244–245**, 444–456 (2013).
13. Shen, K. *et al.* Ordered macro-microporous metal- organic framework single crystals. *Science (80-.).* **359**, 206–210 (2018).
14. Dincă, M. & Léonard, F. Metal–organic frameworks for electronics and photonics. *MRS Bull.* **41**, 854–857 (2016).
15. Sun, L., Campbell, M. G. & Dincă, M. Electrically Conductive Porous Metal–Organic Frameworks. *Angew. Chemie Int. Ed.* **55**, 3566–3579 (2016).
16. Hmadeh, M. *et al.* New Porous Crystals of Extended Metal-Catecholates. *Chem. Mater.* **24**, 3511–3513 (2012).
17. Smith, M. K. *et al.* Direct Self-Assembly of Conductive Nanorods of Metal-Organic Frameworks into Chemiresistive Devices on Shrinkable Polymer Films Direct Self-

- Assembly of Conductive Nanorods of Metal-Organic Frameworks into Chemiresistive Devices on Shrinkable Polymer Films. *Chem. Mater.* **28**, 5264 (2016).
18. Yao, M. S. *et al.* Layer-by-Layer Assembled Conductive Metal–Organic Framework Nanofilms for Room-Temperature Chemiresistive Sensing. *Angew. Chemie - Int. Ed.* **56**, 16510–16514 (2017).
 19. Rubio-Giménez, V. *et al.* Bottom-Up Fabrication of Semiconductive Metal–Organic Framework Ultrathin Films. *Adv. Mater.* **30**, 1–8 (2018).
 20. Mendecki, L., Ko, M., Zhang, X., Meng, Z. & Mirica, K. A. Porous Scaffolds for Electrochemically Controlled Reversible Capture and Release of Ethylene. *J. Am. Chem. Soc.* **139**, 17229 (2017).
 21. Clough, A. J. *et al.* Metallic Conductivity in a Two-Dimensional Cobalt Dithiolene Metal – Organic Framework. *J. Am. Chem. Soc.* **139**, 10863 (2017).
 22. Cui, J. & Xu, Z. An electroactive porous network from covalent metal–dithiolene links. *Chem. Commun.* **50**, 3986–3988 (2014).
 23. Dong, R. *et al.* High-mobility band-like charge transport in a semiconducting two-dimensional metal–organic framework. *Nat. Mater.* **17**, 1027–1032 (2018).
 24. Sheberla, D. *et al.* High Electrical Conductivity in Ni₃(2,3,6,7,10,11-hexamino-triphenylene)₂, a Semiconducting Metal–Organic Graphene Analogue. *J. Am. Chem. Soc.* **136**, 8859–8862 (2014).
 25. Yuan, K. *et al.* Construction of Large-Area Ultrathin Conductive Metal – Organic Framework Films through Vapor-Induced Conversion. *Small* 1804845 (2019). doi:10.1002/smll.201804845
 26. Campbell, M. G., Liu, S. F., Swager, T. M. & Dincă, M. Chemiresistive Sensor Arrays from Conductive 2D Metal–Organic Frameworks. *J. Am. Chem. Soc.* **137**, 13780–13783 (2015).
 27. Kambe, T. *et al.* π -Conjugated Nickel Bis(dithiolene) Complex Nanosheet. *J. Am. Chem. Soc.* **135**, 2462–2465 (2013).
 28. Kambe, T. *et al.* Redox Control and High Conductivity of Nickel Bis(dithiolene) Complex π -Nanosheet: A Potential Organic Two-Dimensional Topological Insulator. *J. Am. Chem. Soc.* **136**, 14357–14360 (2014).
 29. Dou, J. *et al.* Signature of Metallic Behavior in the Metal – Organic Frameworks. *J. Am. Chem. Soc.* **139**, 13608 (2017).
 30. Feng, D. *et al.* Robust and conductive two-dimensional metal–organic frameworks with exceptionally high volumetric and areal capacitance. *Nat. Energy* **3**, 1–7 (2018).
 31. Park, J. *et al.* Synthetic Routes for a 2D Semiconductive Copper Hexahydroxybenzene Metal–Organic Framework. *J. Am. Chem. Soc.* **140**, 14533 (2018).
 32. Huang, X. *et al.* A two-dimensional p–d conjugated coordination polymer with extremely

- high electrical conductivity and ambipolar transport behaviour. *Nat. Commun.* **6**, 1–8 (2015).
33. Xing Huang, Shuai Zhang, Liyao Liu, Lei Yu, Genfu Chen, Wei Xu, and D. Z. Superconductivity in a Cu(II) based coordination polymer with perfect kagomè structure. *Angew. Chemie Int. Ed.* **57**, 146 (2018).
 34. Pal, T. *et al.* Interfacial Synthesis of Electrically Conducting Palladium Bis(dithiolene) Complex Nanosheet. *Chempluschem* **80**, 1255–1258 (2015).
 35. Jia, H. *et al.* A novel two-dimensional nickel phthalocyanine-based metal–organic framework for highly efficient water oxidation catalysis. *J. Mater. Chem. A* **6**, 1188–1195 (2018).
 36. Lu, J. L. *et al.* Two-Dimensional Node-Line Semimetals in a Honeycomb-Kagome Lattice*. *Chinese Phys. Lett.* **34**, (2017).
 37. Wu, M. *et al.* Conetronics in 2D metal-organic frameworks: double/half Dirac cones and quantum anomalous Hall effect. *2D Mater.* **4**, 015015 (2017).
 38. Zhao, B., Zhang, J., Feng, W., Yao, Y. & Yang, Z. Quantum spin Hall and Z_2 metallic states in an organic material. *Phys. Rev. B* **90**, 201403 (2014).
 39. Wang, Z. F., Su, N. & Liu, F. Prediction of a Two-Dimensional Organic Topological Insulator. *Nano Lett.* **13**, 2842–2845 (2013).
 40. Mortazavi, B., Shahrokhi, M., Makaremi, M., Cuniberti, G. & Rabczuk, T. First-principles investigation of Ag-, Co-, Cr-, Cu-, Fe-, Mn-, Ni-, Pd- and Rh-hexaaminobenzene 2D metal-organic frameworks. *Mater. Today Energy* **10**, 336–342 (2018).
 41. Zhang, X., Zhou, Y., Cui, B., Zhao, M. & Liu, F. Theoretical Discovery of a Superconducting Two-Dimensional Metal – Organic Framework. (2017). doi:10.1021/acs.nanolett.7b02795
 42. Sheberla, D., Bachman, J. C., Elias, J. S., Sun, C. & Shao-horn, Y. Conductive MOF electrodes for stable supercapacitors with high areal capacitance. *Nat. Mater.* **16**, 220 (2017).
 43. Gu, S., Bai, Z., Majumder, S., Huang, B. & Chen, G. Conductive metal–organic framework with redox metal center as cathode for high rate performance lithium ion battery. *J. Power Sources* **429**, 22–29 (2019).
 44. Mendecki, L. & Mirica, K. A. Conductive Metal-Organic Frameworks as Ion-to-Electron Transducers in Potentiometric Sensors. *ACS Appl. Mater. Interfaces* **10**, 19248–19257 (2018).
 45. Smith, M. K. & Mirica, K. A. Self-Organized Frameworks on Textiles (SOFT): Conductive Fabrics for Simultaneous Sensing, Capture, and Filtration of Gases. *J. Am. Chem. Soc.* **139**, 16759–16767 (2017).
 46. Ko, M., Aykanat, A., Smith, M. K. & Mirica, K. A. Drawing sensors with ball-milled

- blends of metal-organic frameworks and graphite. *Sensors (Switzerland)* **17**, (2017).
47. Ko, M., Mendecki, L. & Mirica, K. A. Conductive two-dimensional metal-organic frameworks as multifunctional materials. *Chem. Commun.* **54**, 7873–7891 (2018).
 48. Campbell, M. G., Sheberla, D., Liu, S. F., Swager, T. M. & Dincă, M. Cu₃(hexaiminotriphenylene)₂: An Electrically Conductive 2D Metal–Organic Framework for Chemiresistive Sensing. *Angew. Chemie Int. Ed.* **54**, 4349–4352 (2015).
 49. Wu, G., Huang, J., Zang, Y., He, J. & Xu, G. Porous field-effect transistors based on a semiconductive metal-organic framework. *J. Am. Chem. Soc.* **139**, 1360–1363 (2017).
 50. Choi, H. H., Cho, K., Frisbie, C. D., Siringhaus, H. & Podzorov, V. Critical assessment of charge mobility extraction in FETs. *Nat. Mater.* **17**, 2–7 (2017).
 51. Dong, R. *et al.* A coronene-based semiconducting two-dimensional metal-organic framework with ferromagnetic behavior. *Nat. Commun.* **9**, 1–9 (2018).
 52. Li, W. *et al.* High temperature ferromagnetism in π -conjugated two-dimensional metal-organic frameworks. *Chem. Sci.* **8**, 2859–2867 (2017).
 53. Liu, J. & Sun, Q. Enhanced Ferromagnetism in a Mn₃C₁₂N₁₂H₁₂ Sheet. *ChemPhysChem* **16**, 614–620 (2015).
 54. Balluffi, R. W., Allen, S. M. & Carter, W. C. *Kinetics of Materials*. (Wiley).
 55. J., C. Ein neues Verfahren zur Messung der Kristallisationsgeschwindigkeit der Metalle. *Zeitschrift für Phys. Chemie* **92**, 219 (1918).
 56. Gaillac, R. *et al.* Liquid metal–organic frameworks. *Nat. Mater.* **16**, 1149 (2017).
 57. Van Vleet, M. J., Weng, T., Li, X. & Schmidt, J. R. In Situ, Time-Resolved, and Mechanistic Studies of Metal-Organic Framework Nucleation and Growth. *Chem. Rev.* **118**, 3681–3721 (2018).
 58. Stock, N. & Biswas, S. Synthesis of Metal-Organic Frameworks (MOFs): Routes to Various MOF Topologies, Morphologies, and Composites. *Chem. Rev.* **112**, 933–969 (2012).
 59. Evans, A. M. *et al.* Seeded growth of single-crystal two-dimensional covalent organic frameworks. *Science (80-.)*. **57**, 52–57 (2018).
 60. Cheetham, A. K., Kieslich, G. & Yeung, H. H. M. Thermodynamic and Kinetic Effects in the Crystallization of Metal-Organic Frameworks. *Acc. Chem. Res.* **51**, 659–667 (2018).
 61. Dong, R. *et al.* Large-Area, Free-Standing, Two-Dimensional Supramolecular Polymer Single-Layer Sheet for Highly Efficient Electrocatalytic Hydrogen Evolution. *Angew. Chemie Int. Ed.* **54**, 12058 (2015).
 62. Gao, Z. A. *et al.* Synthesis and characterization of a single-layer conjugated metal–organic structure featuring a non-trivial topological gap. 878–881 (2019). doi:10.1039/c8nr08477g
 63. Walch, H. *et al.* Extended Two-Dimensional Metal–Organic Frameworks Based on

- Thiolate–Copper Coordination Bonds. *J. Am. Chem. Soc.* **133**, 7909–7915 (2011).
64. Yokoyama, D. Molecular orientation in small-molecule organic light-emitting diodes. *J. Mater. Chem.* **21**, 19187 (2011).
 65. Kim, H. J. *et al.* Molecular alignment and nanostructure of 1,4,5,8,9,11-hexaazatriphenylene- hexanitrile (HATCN) thin films on organic surfaces. *J. Mater. Chem. C* **1**, 1260–1264 (2013).
 66. Kubelka, P. & Munk, F. Ein Beitrag zur Optik der Farbanstriche. *Zeits. f. Techn. Phys.* **12**, 593 (1931).
 67. Tauc, J. OPTICAL PROPERTIES AND ELECTRONIC STRUCTURE OF AMORPHOUS Ge AND Si. *Mater. Res. Bull.* **3**, 37 (1968).
 68. Manssor, M. I. & Davis, E. A. Optical and electrical characteristics of a-GaAs and a-AlGaAs prepared by radio-frequency sputtering. *J. Phys. Condens. Matter* **2**, 8063–8074 (1990).
 69. Murri, R., Schiavulli, L., Pinto, N. & Ligonzo, T. Urbach tail in amorphous gallium arsenide films. *J. Non. Cryst. Solids* **139**, 60–66 (1992).
 70. Dias da Silva, J. H., Campomanes, R. R., Leite, D. M. G., Orapunt, F. & O’Leary, S. K. Relationship between the optical gap and the optical-absorption tail breadth in amorphous GaAs. *J. Appl. Phys.* **96**, 7052–7059 (2004).
 71. Zhang, Y., Tan, Y.-W., Stormer, H. L. & Kim, P. Experimental observation of the quantum Hall effect and Berry’s phase in graphene. *Nature* **438**, 201–204 (2005).
 72. Kang, S. J. *et al.* Inking elastomeric stamps with micro-patterned, single layer graphene to create high-performance OFETs. *Adv. Mater.* **23**, 3531–3535 (2011).
 73. Miner, E. M., Wang, L. & Dincă, M. Modular O₂ electroreduction activity in triphenylene-based metal–organic frameworks. *Chem. Sci.* **3**, 6286–6291 (2018).
 74. Kittel, C. *Introduction to solid state physics.* (Wiley, 2004).
 75. McClure, J. W. Analysis of Multicarrier Galvanomagnetic Data for Graphite. *Phys. Rev.* **112**, 715–721 (1958).
 76. Chwang, R., Smith, B. J. & Crowell, C. R. Contact size effects on the van der Pauw method for resistivity and Hall coefficient measurement. *Solid State Electron.* **17**, 1217–1227 (1974).
 77. Jacoboni, C., Canali, C., Ottaviani, G. & Alberigi Quaranta, A. A review of some charge transport properties of silicon. *Solid. State. Electron.* **20**, 77–89 (1977).
 78. Seto, J. Y. W. The electrical properties of polycrystalline silicon films. *J. Appl. Phys.* **46**, 5247–5254 (1975).
 79. Wang, X. *et al.* High electrical conductivity and carrier mobility in oCVD PEDOT thin films by engineered crystallization and acid treatment. *Sci. Adv.* **4**, eaat5780 (2018).

80. Cao, Y. *et al.* Unconventional superconductivity in magic-angle graphene superlattices. *Nature* **556**, 43–50 (2018).
81. Kondakova, M. E. *et al.* High-efficiency, low-voltage phosphorescent organic light-emitting diode devices with mixed host. *J. Appl. Phys.* **104**, 094501 (2008).
82. Chopra, N. *et al.* High efficiency and low roll-off blue phosphorescent organic light-emitting devices using mixed host architecture. *Appl. Phys. Lett.* **97**, 033304 (2010).
83. Park, Y.-S. *et al.* Exciplex-Forming Co-host for Organic Light-Emitting Diodes with Ultimate Efficiency. *Adv. Funct. Mater.* **23**, 4914–4920 (2013).
84. Shin, H. *et al.* Blue Phosphorescent Organic Light-Emitting Diodes Using an Exciplex Forming Co-host with the External Quantum Efficiency of Theoretical Limit. *Adv. Mater.* **26**, 4730–4734 (2014).
85. Lee, J.-H. *et al.* An Exciplex Forming Host for Highly Efficient Blue Organic Light Emitting Diodes with Low Driving Voltage. *Adv. Funct. Mater.* **25**, 361–366 (2015).
86. Padmaperuma, A. B., Sapochak, L. S. & Burrows, P. E. New Charge Transporting Host Material for Short Wavelength Organic Electrophosphorescence: 2,7-Bis(diphenylphosphine oxide)-9,9-dimethylfluorene. *Chem. Mater.* **18**, 2389–2396 (2006).
87. Liu, S.-W., Lee, J.-H., Lee, C.-C., Chen, C.-T. & Wang, J.-K. Charge carrier mobility of mixed-layer organic light-emitting diodes. *Appl. Phys. Lett.* **91**, 142106 (2007).
88. Schwartz, G., Ke, T.-H., Wu, C.-C., Walzer, K. & Leo, K. Balanced ambipolar charge carrier mobility in mixed layers for application in hybrid white organic light-emitting diodes. *Appl. Phys. Lett.* **93**, 073304 (2008).
89. Grover, R., Srivastava, R., Kamalasanan, M. N. & Mehta, D. S. Percolation dominated electron transport in Tetracyanoquinodimethane mixed 4,7-diphenyl-1,10-phenanthroline thin films. *Org. Electron.* **13**, 3074–3078 (2012).
90. Li, C., Duan, L., Li, H. & Qiu, Y. Percolative charge transport in a co-evaporated organic molecular mixture. *Org. Electron.* **14**, 3312–3317 (2013).
91. Sahimi, M. *Applications of percolation theory*. (CRC Press, 1994).
92. M., R. *et al.* Transport in polyaniline networks near the percolation threshold. *Phys. Rev. B* **50**, 13931–13941 (1994).
93. Sixou, B., Travers, J. P., Barthet, C. & Guglielmi, M. Electronic conduction in polyaniline-polyethylene oxide and polyaniline-Nafion blends: Relation to morphology and protonation level. *Phys. Rev. B* **56**, 4604–4613 (1997).
94. Planès, J. *et al.* Transport properties of polyaniline-cellulose-acetate blends. *Phys. Rev. B* **58**, 7774–7785 (1998).
95. Fraysse, J. & Planès, J. Interplay of Hopping and Percolation in Organic Conducting Blends. *Phys. status solidi* **218**, 273–277 (2000).

96. Planès, J. & François, A. Percolation scaling, inhomogeneity, and defects in polyaniline blends: A $1/f$ noise diagnosis. *Phys. Rev. B* **70**, 184203 (2004).
97. Vakhshouri, K., Kozub, D. R., Wang, C., Salleo, A. & Gomez, E. D. Effect of Miscibility and Percolation on Electron Transport in Amorphous Poly(3-Hexylthiophene)/Phenyl- $\{\mathrm{C}\}_{61}$ -Butyric Acid Methyl Ester Blends. *Phys. Rev. Lett.* **108**, 026601 (2012).
98. Miller, A. & Abrahams, E. Impurity Conduction at Low Concentrations. *Phys. Rev.* **120**, 745–755 (1960).
99. Gill, W. D. Drift mobilities in amorphous charge-transfer complexes of trinitrofluorenone and poly-n-vinylcarbazole. *J. Appl. Phys.* **43**, 5033–5040 (1972).
100. Itaya, A., Okamoto, K. & Kusabayashi, S. Hole Transport in Amorphous Films of Poly(N-vinylcarbazole), Copolymers of N-Vinylcarbazole with Styrene, Polystyrene Molecularly-Doped with N-Isopropylcarbazole, and 1,3-Di(N-carbazolyl)propane. *Polym. J.* **17**, 557–565 (1985).
101. Lemus, S. J. S. & Hirsch, J. Hole transport in isopropyl carbazole—polycarbonate mixtures. *Philos. Mag. Part B* **53**, 25–39 (1986).
102. Rubel, O., Baranovskii, S. D., Thomas, P. & Yamasaki, S. Concentration dependence of the hopping mobility in disordered organic solids. *Phys. Rev. B* **69**, 014206 (2004).
103. Baranovskii, S. D. Theoretical description of charge transport in disordered organic semiconductors. *Phys. status solidi* **251**, 487–525 (2014).
104. Bäessler, H. Charge Transport in Disordered Organic Photoconductors a Monte Carlo Simulation Study. *Phys. status solidi* **175**, 15–56 (1993).
105. Yang, J. P., Rannou, P., Planès, J., Proń, A. & Nechtschein, M. Preparation of low density polyethylene-based polyaniline conducting polymer composites with low percolation threshold via extrusion. *Synth. Met.* **93**, 169–173 (1998).
106. Goffri, S. *et al.* Multicomponent semiconducting polymer systems with low crystallization-induced percolation threshold. *Nat. Mater.* **5**, 950–956 (2006).
107. Shklovskii, B.I. & Efros, A.L. *Electronic Properties of Doped Semiconductors*. (Springer-Verlag, 1984).
108. Nenashev, A. V., Oelerich, J. O. & Baranovskii, S. D. Theoretical tools for the description of charge transport in disordered organic semiconductors. *J. Phys. Condens. Matter* **27**, 093201 (2015).
109. Arkhipov, V. I., Emelianova, E. V. & Bäessler, H. Equilibrium carrier mobility in disordered hopping systems. *Philos. Mag. Part B* **81**, 985–996 (2001).
110. Hirsch, J. Hopping transport in disordered aromatic solids: a re-interpretation of mobility measurements on PKV and TNF. *J. Phys. C Solid State Phys.* **12**, 321–335 (1979).
111. Kirkpatrick, S. Percolation and Conduction. *Rev. Mod. Phys.* **45**, 574–588 (1973).

112. Baldo, M. A. *et al.* Highly efficient phosphorescent emission from organic electroluminescent devices. *Nature* **395**, 151–154 (1998).
113. Baldo, M. A., Lamansky, S., Burrows, P. E., Thompson, M. E. & Forrest, S. R. Very high-efficiency green organic light-emitting devices based on electrophosphorescence. *Appl. Phys. Lett.* **75**, 4–6 (1999).
114. Lee, J. *et al.* Hot excited state management for long-lived blue phosphorescent organic light-emitting diodes. *Nat. Commun.* **8**, 15566 (2017).
115. Aziz, H. & Popovic, Z. D. Degradation phenomena in small-molecule organic light-emitting devices. *Chem. Mater.* **16**, 4522–4532 (2004).
116. So, F. & Kondakov, D. Degradation mechanisms in small-molecule and polymer organic light-emitting diodes. *Adv. Mater.* **22**, 3762–3777 (2010).
117. Scholz, S., Kondakov, D., Lüssem, B. & Leo, K. Degradation Mechanisms and Reactions in Organic Light-Emitting Devices. *Chem. Rev.* **115**, 8449–8503 (2015).
118. Fry, C., Racine, B., Vaufrey, D., Doyeux, H. & Ciñ, S. Physical mechanism responsible for the stretched exponential decay behavior of aging organic light-emitting diodes. *Appl. Phys. Lett.* **87**, 213502 (2005).
119. Giebink, N. C. *et al.* Intrinsic luminance loss in phosphorescent small-molecule organic light emitting devices due to bimolecular annihilation reactions. *J. Appl. Phys.* **103**, (2008).
120. Kondakov, D. Y. The Role of Homolytic Reactions in the Intrinsic Degradation of OLEDs. *Org. Electron. Mater. Process. Devices Appl.* 211–242 (2010).
121. Marques dos Anjos, P. N. Analysis of electroluminescence degradation for organic light-emitting diode using a rate equation of chemical kinetics. *J. Inf. Disp.* **14**, 115–120 (2013).
122. López Varo, P., Jiménez Tejada, J. A., López Villanueva, J. A. & Deen, M. J. Space-charge and injection limited current in organic diodes: A unified model. *Org. Electron.* **15**, 2526–2535 (2014).
123. Hershey, K. W. & Holmes, R. J. Unified Analysis of Transient and Steady-State Electroluminescence -Establishing an Analytical Formalism for OLED Charge Balance. *SID Symp. Dig. Tech. Pap.* **48**, 115–118 (2017).
124. Coehoorn, R., Van Eersel, H., Bobbert, P. A. & Janssen, R. A. J. Kinetic Monte Carlo Study of the Sensitivity of OLED Efficiency and Lifetime to Materials Parameters. *Adv. Funct. Mater.* **25**, 2024–2037 (2015).
125. Xu, X. *et al.* Efficient Phosphorescent OLEDs for Warm White And Cool White Lighting Applications. *SID Int. Symp. Dig. Tech. Pap.* 614–616 (2012).
126. Murgia, M. *et al.* In-situ characterisation of the oxygen induced changes in a UHV grown organic light-emitting diode. *Synth. Met.* **102**, 1095–1096 (1999).
127. Giebink, N. C., D'Andrade, B. W., Weaver, M. S., Brown, J. J. & Forrest, S. R. Direct

- evidence for degradation of polaron excited states in organic light emitting diodes. *J. Appl. Phys.* **105**, (2009).
128. Reineke, S., Walzer, K. & Leo, K. Triplet-exciton quenching in organic phosphorescent light-emitting diodes with Ir-based emitters. *Phys. Rev. B* **75**, 125328 (2007).
 129. Baldo, M. A., Adachi, C. & Forrest, S. R. Transient analysis of organic electrophosphorescence. II. Transient analysis of triplet-triplet annihilation. *Phys. Rev. B* **62**, 10967–10977 (2000).
 130. Popovic, Z. D., Aziz, H., Hu, N. X., Ioannidis, A. & Dos Anjos, P. N. M. Simultaneous electroluminescence and photoluminescence aging studies of tris(8-hydroxyquinoline) aluminum-based organic light-emitting devices. *J. Appl. Phys.* **89**, 4673–4675 (2001).
 131. Schmidt, T. D. *et al.* Degradation induced decrease of the radiative quantum efficiency in organic light-emitting diodes. *Appl. Phys. Lett.* **101**, 103301 (2012).
 132. Schmidt, T. D., Jäger, L., Noguchi, Y., Ishii, H. & Brütting, W. Analyzing degradation effects of organic light-emitting diodes via transient optical and electrical measurements. *J. Appl. Phys.* **117**, (2015).
 133. Holzer, W., Penzkofer, A. & Tsuboi, T. Absorption and emission spectroscopic characterization of Ir(ppy)₃. *Chem. Phys.* **308**, 93–102 (2005).
 134. Zhang, Y., Lee, J. & Forrest, S. R. Tenfold increase in the lifetime of blue phosphorescent organic light-emitting diodes. *Nat. Commun.* **5**, 5008 (2014).
 135. Celebi, K., Heidel, T. D. & Baldo, M. A. Simplified calculation of dipole energy transport in a multilayer stack using dyadic Green's functions. *Opt. Express* **15**, 1762–1772 (2007).
 136. Paquette, S. Enhanced Photostability In Organic Thin Films Deposited On Plasmonic Substrates. (University of Rochester, 2012).
 137. Catrice Carter; Zeqing Shen; Kun Zhu; Kelsey Gwynne; Deirdre M. O'Carroll. Photoluminescence stability of blue organic phosphorescent materials on plasmonic silver nanostructure architectures. in *Proc. SPIE 10529, Organic Photonic Materials and Devices XX* 1052907 (2018).
 138. Pettersson, L. A. A., Roman, L. S. & Inganäs, O. Modeling photocurrent action spectra of photovoltaic devices based on organic thin films. *J. Appl. Phys.* **86**, 487–496 (1999).
 139. Thomas, D. D., Carlsen, W. F. & Stryer, L. Fluorescence energy transfer in the rapid-diffusion limit. *Proc. Natl. Acad. Sci.* **75**, 5746–5750 (1978).
 140. Yoshida, H. & Yoshizaki, K. Electron affinities of organic materials used for organic light-emitting diodes: A low-energy inverse photoemission study. *Org. Electron.* **20**, 24–30 (2015).
 141. Mäkinen, A. J., Hill, I. G. & Kafafi, Z. H. Vacuum level alignment in organic guest-host systems. *J. Appl. Phys.* **92**, 1598–1603 (2002).
 142. Peng, C. *et al.* Probing the Emission Zone Length in Organic Light Emitting Diodes via

Photoluminescence and Electroluminescence Degradation Analysis. *ACS Appl. Mater. Interfaces* **9**, 41421–41427 (2017).

143. Einzinger, M. *et al.* Shorter Exciton Lifetimes via an External Heavy-Atom Effect: Alleviating the Effects of Bimolecular Processes in Organic Light-Emitting Diodes. *Adv. Mater.* **29**, 1–7 (2017).